

Review

Recent Advances in MOF-Based Materials for Remediation of Heavy Metals and Organic Pollutants: Insights into Performance, Mechanisms, and Future Opportunities

Cuilian Yang^{1,2,†}, Zhuangzhuang Xue^{1,2,†} and Jia Wen^{1,2,*} ¹ Research Institute of Hunan University in Chongqing, Hunan University, Chongqing 401120, China² College of Environmental Science and Engineering, Hunan University, Changsha 410082, China

* Correspondence: jwen@hnu.edu.cn

† These authors contributed equally to this work.

Abstract: In recent years, heavy metals and organic pollutants have become two major obstacles to maintaining the ecological environment. Thus, choosing efficient and environmentally friendly methods and materials to remediate heavy metals and organic pollution has become a hot research topic. Porous metal–organic frameworks (MOFs) and their composites or derivatives can be used as ideal adsorbents and catalytic materials because of their unique structures and functions. This work reviews the research progress on MOF-based materials in the remediation of the water environment in the past decade. The MOF-based materials discussed here mainly include MOF composites obtained by fabrication and MOF derivatives obtained by pyrolysis. Both MOF composites and MOF derivatives are optimized materials that exhibit adsorption or catalytic performance superior to the pristine MOFs. Additionally, the interactions and mechanisms between the MOF-based materials and different heavy metals or organic pollutants are discussed in detail. Finally, some problems or defects of the MOF-based materials are also proposed considering the materials' economic efficiency, stability and safety. There is still a long way forward for the real application of MOF-based materials. Further efforts are also needed to explore and expand the environmental remediation scope of MOF-based materials.

Keywords: MOF composites; MOF derivatives; heavy metals; organic pollutants; remediation



Citation: Yang, C.; Xue, Z.; Wen, J. Recent Advances in MOF-Based Materials for Remediation of Heavy Metals and Organic Pollutants: Insights into Performance, Mechanisms, and Future Opportunities. *Sustainability* **2023**, *15*, 6686. <https://doi.org/10.3390/su15086686>

Academic Editor: Guannan Liu

Received: 21 March 2023

Revised: 10 April 2023

Accepted: 13 April 2023

Published: 14 April 2023



Copyright: © 2023 by the authors. Licensee MDPI, Basel, Switzerland. This article is an open access article distributed under the terms and conditions of the Creative Commons Attribution (CC BY) license (<https://creativecommons.org/licenses/by/4.0/>).

1. Introduction

With the continuous development of the economy and growth of the world population, more and more pollutants are produced because of human activities. They can be detected in various environmental media, seriously threatening the ecological environment and human health. In particular, heavy metals (HMs) and organic pollutants (OPs) are common pollutants in the water environment (including groundwater and surface water). Heavy metals are mainly from mining, smelting, electroplating, and tanning industries, and the pollution as a result of HMs is particularly severe in developing countries [1]. Lead (Pb), chromium (Cr), cadmium (Cd), arsenic (As), and mercury (Hg) are common HMs in the environment. Their characteristics of high toxicity, potential accumulation and non-biodegradability in the environment will potentially cause harm to animals, plants and humans [1,2]. Organic pollutants have the characteristics of inertness and persistence in the environment. Since the 20th century, millions of organic chemicals have been discovered and manufactured with the rapid development of industry and the chemical industry [3]. Typical aqueous OPs in water can be classified as conventional industrial organics, organic dyes, pesticides, pharmaceuticals and personal care products (PPCPs), etc. Some typical HMs and OPs can be found in drinking water, and the US EPA has set strict limitation for them (Table 1).

Table 1. USA drinking water quality criteria standards for HMs and OPs [4].

HMs	MCLG ¹ (mg/L)	MCL ² (mg/L)
Mercury (inorganic)	0.002	0.002
Lead	zero	0.015
Cadmium	0.005	0.005
Copper	1.3	1.3
Arsenic	zero	0.05
Antimony	0.006	0.006
Chromium (total)	0.1	0.1
OPs	MCLG (mg/L)	MCL (mg/L)
Chlorobenzene	0.1	0.1
Dichloromethane	zero	0.005
Ethylbenzene	0.7	0.7
Four Vinyl Chloride	zero	0.005
Atrazine	0.003	0.003
Diquat	0.02	0.02
Lindane	0.0002	0.0002
Gebutox	0.007	0.007
Glyphosate	0.7	0.7
Polychlorinated biphenyls	zero	0.0005
Xylenes	10	10

¹ MCLG: maximum contaminant level goal. A non-enforceable health goal that is set at a level at which no known or anticipated adverse effect on the health of persons occurs and that allows an adequate margin of safety.

² MCL: maximum contaminant level. The highest level of a contaminant that is allowed in drinking water. MCLs are set as close to the MCLG as feasible using the best available analytical and treatment technologies and taking cost into consideration. MCLs are enforceable standards.

Over the past decades, researchers have been committed to researching porous materials with adsorption and catalytic properties. As a new type of porous material, metal-organic frameworks (MOFs) have attracted more and more attention because of their high porosity, large surface areas, and structural diversity [5–7]. Metal-organic frameworks are composed of metal ions or clusters and organic ligands, and they are organic-inorganic hybrid materials with intramolecular pores connected by medium-strength coordination bonds [8]. The organic ligand is usually a multidentate organic ligand containing oxygen and nitrogen, including polycarboxylic acid aromatic ligands (e.g., terephthalic acid (BDC) and trimesic acid (BTC)) and nitrogen-containing heterocyclic ligands (e.g., imidazoles, tetrazoles, pyrimidines, pyridines, purines, etc.) [9,10]. The inorganic metal cluster is generally composed of transition metal ions, including common 3d type divalent metal ions (Ni^{2+} , Zn^{2+} , etc.), trivalent metal ions (Fe^{3+} , Co^{3+} , Cr^{3+} , Sc^{3+} , V^{3+} , etc.), p-type trivalent metal ions (Al^{3+} , In^{3+} , etc.), and some rare-earth metal ions. MOFs, first synthesized and named by Yaghi et al. in 1995 [11], have been developed to possess a greater family including MIL (Materials of Institut Lavoisier) [12], UIO (University of Oslo) [13], and ZIF (Zeolitic imidazolate framework) [2], etc. At present, MOFs have high application prospects in gas storage [13,14], separation [15,16], metal ion detection [17], drug delivery [18], catalysis [19], chemical sensing [20], adsorption [21], etc. MOFs are particularly common in the remediation of HMs and OPs in water [10,21–24].

As adsorbents, MOFs generally have better adsorption capacity than many traditional adsorbents such as zeolite, bio-charcoal, and activated carbon [22,24]. Moreover, MOFs can act as catalysts for the degradation of OPs in the environment due to the catalytic effect of their central metal ions. Although MOFs have achieved good results in remediating HMs and OPs, the pristine MOFs (unmodified or untreated) still have certain defects. A few can be listed as follows: (1) the pristine MOFs in the nano-size form are difficult to separate in water treatment and easily cause secondary pollution; (2) the pristine MOFs are generally small in size and easy to agglomerate; and (3) some MOFs have poor stability and recyclability in water. The above-mentioned defects would thus hinder the exposure of active sites and limit the efficiency of HM and OP treatment. Consequently, numerous

efforts have been applied to improve the performance of MOFs, for example, adjusting the structure or surface properties of the materials and synthesizing MOF-based composites or derivatives.

To date, a large number of articles with regard to MOF-based materials have been published, indicating that they are worthy of attention. This review focuses on the types of MOF-based materials, their removal efficiency, and associated mechanisms for the remediation of HMs and OPs in aqueous environments.

2. What Are MOF-Based Materials?

MOFs have been widely studied and applied in water treatment since they were invented [25,26]. However, as mentioned above, the defects of some pristine MOFs limited their application in the water environment. In recent years, many efforts have been made to improve the stability and performance of MOFs. In particular, many research results have suggested that MOF-based materials are ideal adsorbents or catalysts for removing aqueous pollutants because of their high adsorption capacity, water stability, and reusability [27–30]. Here, MOF-based materials are divided into MOF composites and MOF derivatives. Specifically, the MOF composites mainly include MOF-based core–shell composites and macro-MOF hybrids (further divided into hydro(aero)gel and macro-MOF-coated composites), and the MOF derivatives are further divided into MOF-derived nanoporous carbon (NPC), metal@carbon (metal@C), and metal oxide@carbon (metal oxide@C) (Figure 1).

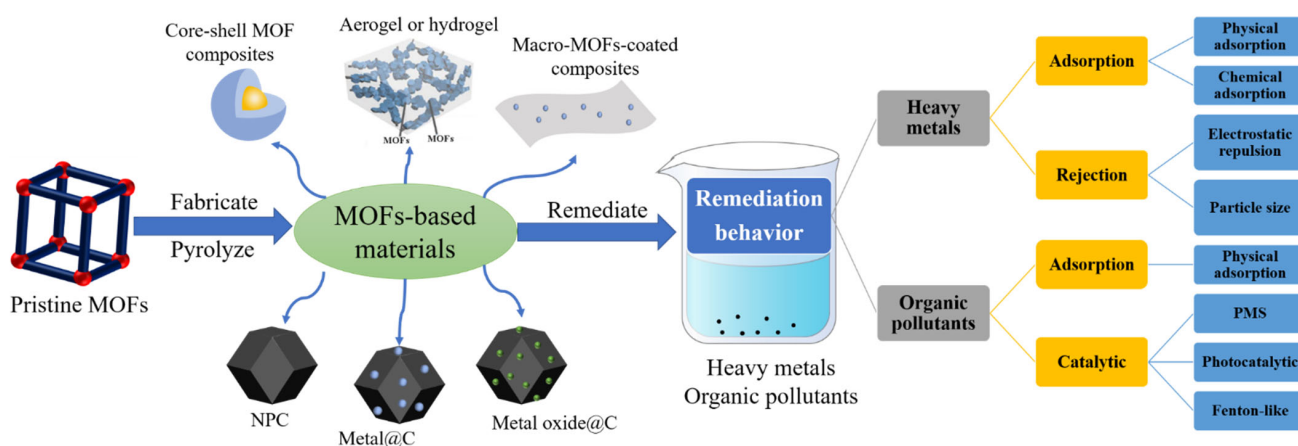


Figure 1. Schematic illustration summarizing the main contents of the present work.

2.1. MOF Composites

MOF composites are a class of materials that combine MOFs with one or more substances with high stability, high surface area, or multifunctional groups (such as hydroxyl groups, amine groups, etc.). Various kinds of MOF composites have been prepared by combining MOFs with inorganic metal nanoparticles (NPs) [29,31,32], graphene oxide (GO) [33,34], reduced graphene oxide (rGO) [30,35], nanofibers [36,37], carbon nanotubes (CNTs) [38], organic polymers [39–41], etc. According to the differences between these functional materials and synthetic methods, MOF composites can be divided into core–shell MOF composites and macro-MOFs [8].

Core–shell MOF composites are the most representative type of multifunctional MOF composite materials. The MOFs can be assembled with other materials (such as a second MOF [42,43], inorganic compounds [32,44], organic polymers [45–47], etc.) to form the core–shell structure. Composite components are usually embedded inside or coated on the surface of the MOFs, so the MOFs can be used as both core and shell. The primary synthetic strategy of the core–shell composites is to make MOFs or another composite component grow in situ by layer-by-layer self-assembly [31,48]. Under reasonable controlling conditions, MOFs, as the shell, can be coated outside of the non-porous materials (such as metal oxide NPs) to form ordered and uniform porous core–shell composites [31,49,50].

Macro-MOFs are a group of emerging MOF composites. They are a type of material combining MOFs with special components with good mechanical properties (such as aerogel and hydrogel [30,51–53]) or depositing MOFs onto supporting materials (such as nanofiber materials [37,54–56], carbon materials [33–35], and composite membranes [33,57,58]). The former are called MOF composite aerogels or hydrogels, and the latter are called macro-MOF-coated composites. The supporting materials can be directly bound to the MOFs or surface-modified to obtain appropriate functional groups, which promote strong adhesion of the MOF particles through electrostatic interaction or covalent bonding [53,57,59]. Generally, the methods of synthesizing macro-MOFs are direct mixing or in situ growth. Macro-MOFs can tackle many problems encountered in water treatment processes, such as secondary pollution and low separation efficiency [35,52].

2.2. MOF Derivatives

Inorganic NPs and porous carbon are both MOF derivatives that show unique advantages in environmental applications. They can be prepared by direct pyrolysis of the virgin MOFs and MOF composites under appropriate conditions. The process does not require any additional carbon source due to the high carbon content of the organic ligands in MOFs [60,61]. For example, the pyrolysis of MOFs at high temperature and inert atmosphere (nitrogen or argon) will generate porous and uniform metal@C materials. If the MOFs are directly heated in an oxygen atmosphere or at low temperature, porous metal oxide@C with high specific surface area and regular morphology can be obtained [62]. For MOFs containing metals with high boiling points, a pickling treatment is needed to etch away the remaining metal substances to obtain a porous carbon material with large pore volume and high specific surface area [63]. Compared with the porous inorganic NPs prepared by traditional methods, the MOF-derived nanostructures have a uniform structure and excellent performance, and they are widely used in catalysis [64], gas storage [65], and removal of pollutants in water [66].

3. Remediation of HMs Using MOF-Based Materials

3.1. Typical Cationic HMs

Hg(II), Pb(II), Cd(II), Ni(II), and Cu(II) are common cationic HMs in the environment [31,67]. Exposure to even a small amount of these HMs can be hazardous to human health due to their non-biodegradability and bioaccumulation [68]. The US Environmental Protection Agency (EPA) hence imposed strict regulations on the limit concentrations of the HMs in water environments, which underlines the importance of removing them from water. Various MOF-based materials that have been widely proven effective and feasible for removal of typical cationic HMs are summarized in Table 2, and some of them show better adsorption properties than many traditional adsorbents.

Table 2. Summary of MOF-based materials as adsorbents for typical cationic HMs.

MOF-Based Materials	HMs	Q_e (mg/g) or Removal Rate (%)	Selectivity	Reusability	Mechanism	Ref.	
Core-shell composites	Fe-BTC/PDA	Hg(II) Pb(II)	1643 394	Ca ²⁺ , Mg ²⁺ , Na ⁺ , K ⁺ , Sr ²⁺ , Pb ²⁺	Reusable	Electrostatic interaction Coordination, Diffusion	[47]
	Fe ₃ O ₄ @Cu ₃ (btc) ₂ -SH	Hg(II) Pb(II)	348.43 215.05	Ni ²⁺ , Na ⁺ , Mg ²⁺ , Ca ²⁺ , Zn ²⁺ , Cd ²⁺	Reusable	Electrostatic interaction Coordination	[69]
	Fe ₃ O ₄ @TMU-32	Hg(II) Pb(II)	909 1607	Cr ³⁺ , Cu ²⁺	Reusable	Electrostatic interaction Coordination	[31]

Table 2. Cont.

MOF-Based Materials	HMs	Q _e (mg/g) or Removal Rate (%)	Selectivity	Reusability	Mechanism	Ref.	
PFe ₃ O ₄ @NH ₂ -MIL-125 (Ti)	Pb(II)	561.7	Ag ⁺ , Be ²⁺ , Cd ²⁺ , Zn ²⁺ , Ni ²⁺ , Mn ²⁺ , Mg ²⁺ , As ³⁺ , Cr ³⁺	Reusable	Chemical bonding (C-N-Pb(II)-O-Fe) Coordination	[70]	
ZIF-8@CA	Pb(II)	1321.21	NO ₃ ⁻ , SO ₄ ²⁻ , Cl ⁻ , Cd ²⁺ , Cu ²⁺ , Zn ²⁺	Reusable	Electrostatic interaction Ion exchange	[39]	
melamine-MOFs	Pb(II)	205	Not mentioned	Reusable	Coordination	[41]	
MCNC@Zn-BTC	Pb(II)	558.66	Cu ²⁺ , Cd ²⁺ , Zn ²⁺	Reusable	Coordination	[48]	
Fe ₃ O ₄ @SiO ₂ @UiO-66	Pb(II)	102	Not mentioned	Reusable	Electrostatic interaction Coordination	[71]	
Fe ₃ O ₄ @SiO ₂ @UiO-66-NH ₂	MB	128					
Fe ₃ O ₄ @SiO ₂ @UiO-66-Urea	MO	219					
NH ₂ -MIL-101(AI)@ZIF-8	Cu(II)	526.74	Li ⁺ , Na ⁺ , K ⁺ , Ca ²⁺ , Mg ²⁺ , Mn ²⁺ , Co ²⁺ , Ni ²⁺ , Hg ²⁺ , Pb ²⁺ , Cd ²⁺	Not mentioned	Coordination Diffusion	[42]	
Macro-MOF composites	PA 300 nanofibers	Hg(II)	Not mentioned	Reusable	Electrostatic interaction Ion exchange	[55]	
	PA 808 nanofibers	Pb(II)					265.45
		Hg(II)					150.95
		Pb(II)					254.4
	Pb(II)	119.9					
PVA/Sb-TBC nanofibers	Pb(II)	91	Ca ²⁺ , Mg ²⁺	Not mentioned	Electrostatic interaction Ion exchange	[54]	
PVA/Sr-TBC nanofibers		124					
PVA/La-TBC nanofibers		194					
UiO-66-NH ₂ @CA aerogels	Pb(II)	89.40	Not mentioned	Reusable	Electrostatic interaction Coordination	[52]	
UiO-66@CA aerogels	Cu(II)	39.33					
	Pb(II)	81.30					
	Cu(II)	31.23					
ZIF-8/rGA aerogels	Pb(II)	281.5	Not mentioned	Reusable	Ion exchange Electrostatic interaction	[30]	
	Cd(II)	101.1					
BC@ZIF-8 aerogels	Pb(II)	390	Pb ²⁺ , Co ²⁺	Reusable	Coordination Diffusion	[51]	
	Cd(II)	220					
ZIF-67/BC/CH aerogels	Cu(II)	200.6	Not mentioned	Not mentioned	Coordination Ion exchange Electrostatic interaction	[53]	
	Cr(VI)	152.1					
PDA/MOF-TFN membrane	Pb(II)	94–99.2%	Not mentioned	Not mentioned	Electrostatic interaction Ion exchange Coordination Size exclusion	[57]	
	Cd(II)						
	Ni(II)						
IRMOF-3/GO-1 PSF@PDA@IRMOF-3/GO-1 membrane	Cu(II)	254.14 89.3%	Na ⁺ , K ⁺ , Ca ²⁺ , Mg ²⁺ , Pb ²⁺ , Ni ²⁺ , Co ²⁺ , Fe ³⁺	Not mentioned	Coordination Electrostatic interaction Size exclusion	[33]	

Table 2. Cont.

MOF-Based Materials	HMs	Q _e (mg/g) or Removal Rate (%)	Selectivity	Reusability	Mechanism	Ref.	
f-ZIF-8@GO membrane	Cu(II)	1872.24	Pb ²⁺ , Co ²⁺	Reusable	Electrostatic interaction Coordination	[34]	
PAN/MOF-808 membrane	Cd(II) Zn(II)	225.05 287.06	Not mentioned	Reusable	Electrostatic interaction Ion exchange Size exclusion	[36]	
UiO-66-(COOH) ₂ /prGO membrane	Cu(II) Cd(II)	96.5–83.1% 92.6–80.4%	Not mentioned	Not mentioned	Electrostatic interaction Size exclusion	[35]	
PAA/ZIF-8/PVDF membrane	Ni(II)	219.09	Na ⁺	Reusable	Hydrogen bonding Ion exchange Coordination	[58]	
MOF derivatives	ZnO/ZnFe ₂ O ₄ /C	Pb(II)	344.83	Not mentioned	Reusable	Ion exchange	[66]
	Ni@C	Pb(II) Cu(II) Cd(II)	92.5 63.4 41.4	Not mentioned	Reusable	van der Waals forces Diffusion	[72]

3.1.1. Adsorption Behavior of MOF Composites

Recent studies suggested that the core–shell structure and functional design of MOF composites can significantly improve the efficiency of HM adsorption and the material's water stability [31,32,48,69–71]. In particular, magnetic NPs and multifunctional group-rich substances (e.g., amino, thiol, and carboxyl) were combined with MOFs and showed excellent results. For example, Ke et al. [69] reported the successful removal of Pb(II) and Hg(II) ions from aqueous samples by using a post-synthetic-modification (PSM) thiol core–shell Fe₃O₄@Cu₃(btc)₂ (Figure 2a). According to the study, the MOF composites exhibited excellent regeneration capability and adsorption performance toward Pb(II) and Hg(II) in a wide pH range (2–10) (Figure 2b). Notably, their selective adsorption affinity for Pb(II) ($K_d = 1.23 \times 10^4$ mL/g) and Hg(II) ($K_d = 5.98 \times 10^4$ mL/g) was remarkable, while they had weak binding affinity for other metals such as Ca²⁺, Na⁺, Ni²⁺, Zn²⁺, Mg²⁺, and Cd²⁺ ($K_d = 19.03$ – 77.06 mL/g) (Figure 2c). Another study also reported a thiol-functionalized CeO₂@UiO-66-(SH)₂ and a magnetically functionalized CeO₂/Fe₃O₄@UiO-66-(SH)₂. The former could simultaneously capture Pb(II) (99%), Hg(II) (98%), Cr (III and VI) (93%), Cd(II) (87%), and As (III and V) (56%) at an aqueous concentration of 100 µg/L. Notably, the latter showed adsorption capacity comparable to that of the former, and they could be easily separated from water by a magnet in less than 5 min [32]. Additionally, a magnetic MOF composite Fe₃O₄@TMU-32 showed a high adsorption capacity for Pb(II) (1600 mg/g) and Hg(II) (905 mg/g), respectively [31]. The TMU-32 precursor itself had carbonyl, amine, and urea functional groups that could interact with the metal ions, and Fe₃O₄ magnetic NPs could modulate the material's surface charge (Figure 2d,e). In a word, different types of core–shell MOF composites can be formed via layer-by-layer self-assembly to improve their removal efficiency, stability, and recovery of materials. Furthermore, highly effective adsorption sites (thiol, amino, carboxyl functional groups, etc.) can be purposefully introduced into the MOFs or composites through PSM or pre-designing methods to improve the densities of chelating functional groups [73].

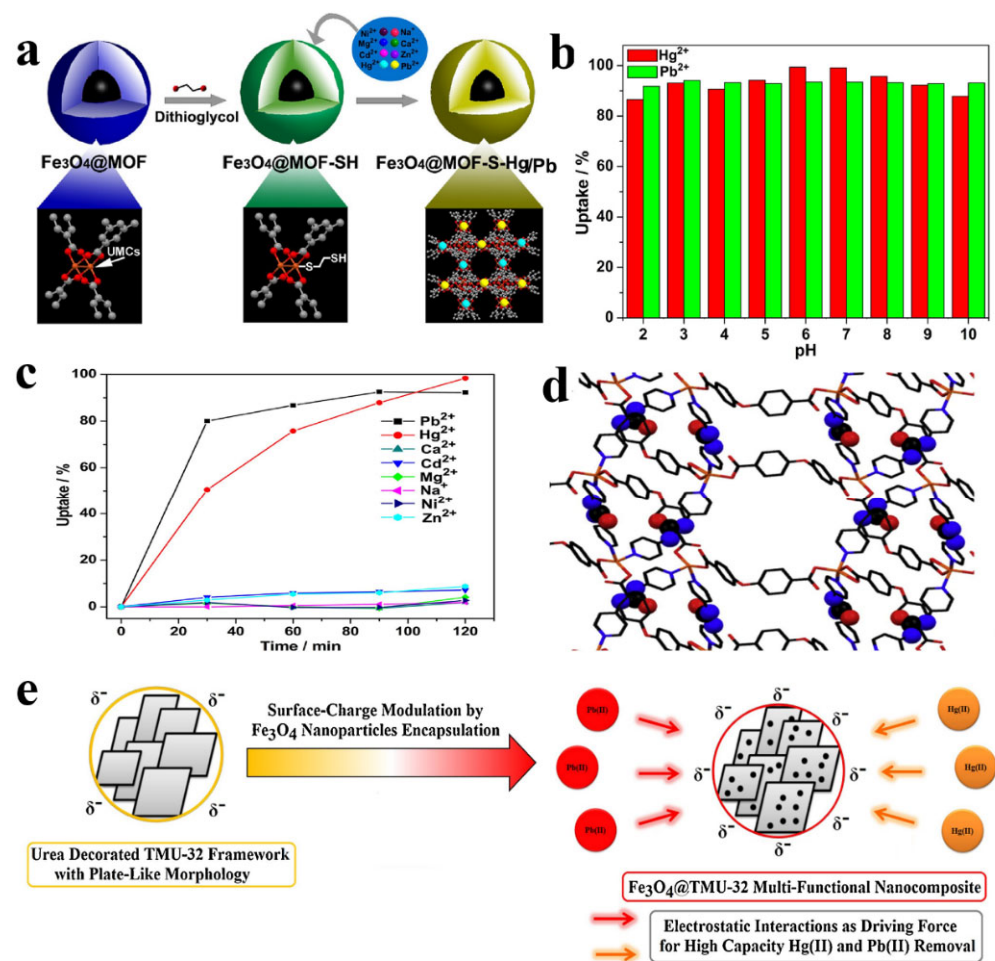


Figure 2. (a) Schematic representation of the preparation of thiol-functionalized Fe₃O₄@Cu₃(btc)₂ core-shell magnetic microspheres and their use for selective heavy metal ion removal. (b) Effects of pH on the Pb(II) and Hg(II) removal efficiency of sample B (Fe₃O₄@Cu₃(btc)₂-DTG-1.13) in the mixture solution (0.5 mM). (c) Adsorption kinetics of sample B (Fe₃O₄@Cu₃(btc)₂-DTG-1.13) for heavy metal ions in the mixture solution (0.5 mM). Reprinted with permission from Ref. [69]. Copyright 2017, Elsevier. (d) Structural representation of TMU-32. (e) Proposed mechanism for Pb(II) and Hg(II) removal by Fe₃O₄@TMU-32. Reprinted with permission from Ref. [31]. Copyright 2018, Elsevier.

The practical application of nano MOFs encounters difficulties because of their poor recycling and secondary water pollution. In 2016, Shooto et al. [54] first proposed an effective strategy to tackle these issues by electrospinning MOFs with nanofibers. They prepared PVA/Sr-TBC, PVA/La-TBC, and PVA/Sb-TBC composite nanofibers, aiming to improve the HM removal efficiency and adjust the mechanical properties of the materials, but the results were not satisfactory. Recently, Ma et al. [51] and Li et al. [53] developed a way to attach ZIF-8 or ZIF-67 to bacterial cellulose (BC) aerogels that can be easily separated from water (Figure 3a). The as-formed macro-MOFs inherited the structural characteristics of ZIF-8 or ZIF-67 and BC (e.g., high porosity, mechanical flexibility, and large surface area). The BC@ZIF-8 composite aerogel exhibited superior adsorption performance for Pb(II) (390 mg/g) and Cd(II) (220 mg/g), while the ZIF-67/BC/CH aerogels removed sufficient amounts of Cu(II) and Cr(VI) (200.6 mg/g and 152.1 mg/g, respectively). The MOF was uniformly distributed in the composite aerogel and did not release during the processing of pollutants. Moreover, the composite aerogel could also return to its original shape immediately after being artificially compressed and dehydrated (Figure 3b). More recently, a novel polydopamine (PDA) decorated MOF thin-film nanocomposite (PDA/MOF-TFN) was synthesized by Wang's group in 2020 [57]. The macro-MOF synthesized using the

in situ deposition method was capable of rejecting Pb(II), Cd(II), Ni(II) and salts from water. According to the study, the PDA/MOF-TFN membrane showed high rejection rates (>94%) for HMs, in the order of Pb(II) > Ni(II) > Cd(II), as a result of its size exclusion and adsorption properties. These new macro MOFs effectively overcome the problems of aggregation and secondary pollution, while improving the mechanical properties and selectivity of the materials toward HMs.

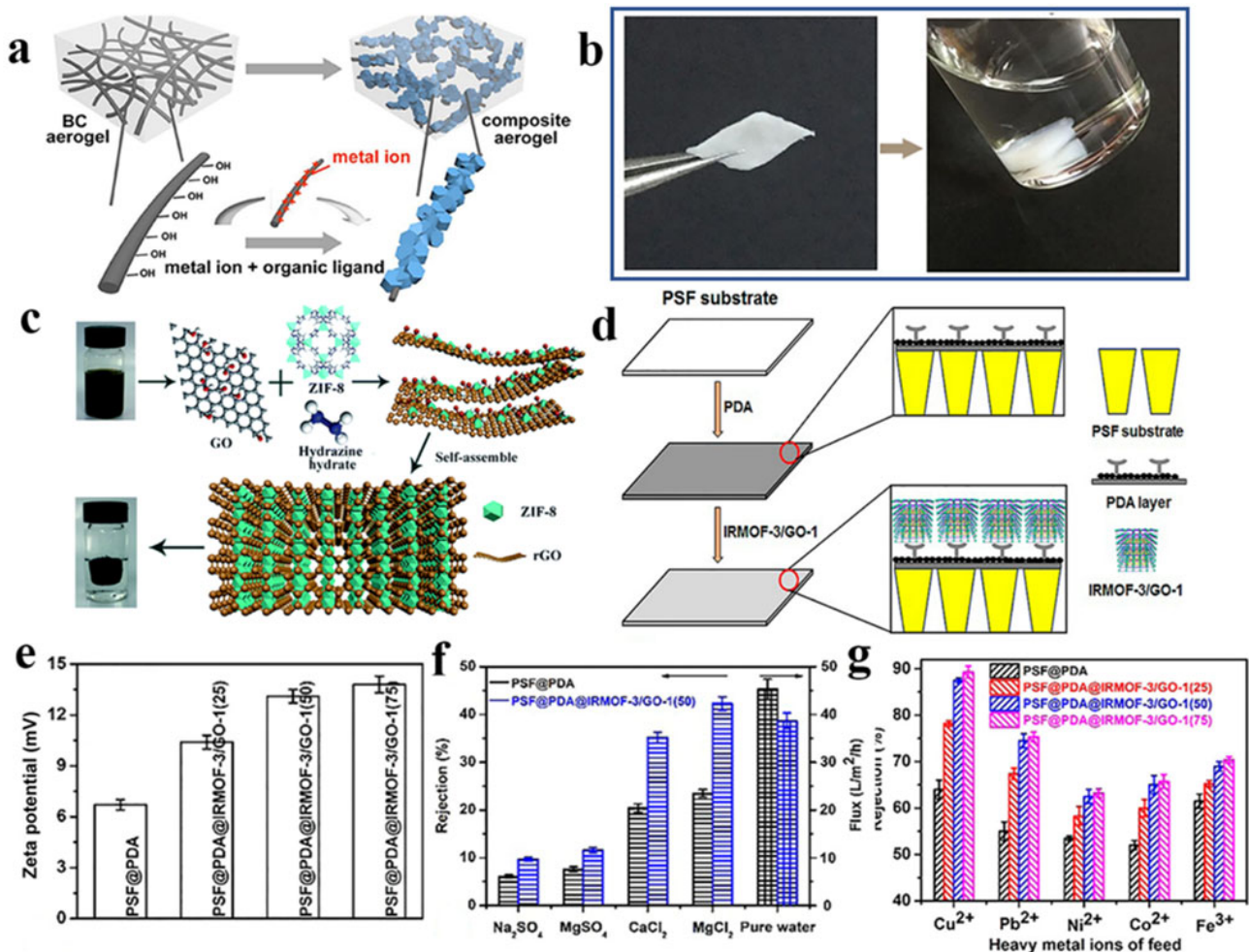


Figure 3. (a) The fabrication process for BC@MOFs composite aerogels. (b) A wet composite aerogel (55 wt% BC@ZIF-8) can be compressed fully (left), and the compressed aerogel recovers its original shape completely when placed in solution again (right). Reprinted with permission from Ref. [51]. Copyright 2018, Elsevier. (c) Schematic of the self-assembly mechanism of the rGO and ZIF-8 nanoparticles for the formation of ZIF-8/rGO composite hydrogels. Reprinted with permission from Ref. [30]. Copyright 2017, The Royal Society of Chemistry. (d) Schematic illustration of the fabrication process for PSF@PDA@IRMOF-3/GO-1. (e) Zeta potentials of PSF@PDA, PSF@PDA@IRMOF-3/GO-1(25), PSF@PDA@IRMOF-3/GO-1(50) and PSF@PDA@IRMOF-3/GO-1(75) membrane surfaces. (f) Salt rejections and pure water fluxes of PSF@PDA and PSF@PDA@IRMOF-3/GO-1(50). (g) Rejections of PSF@PDA and PSF@PDA@IRMOF-3/GO-1 (25, 50 and 75) examined with the feeds containing different heavy metal ions. Reprinted with permission from Ref. [33]. Copyright 2016, American Chemical Society.

Furthermore, the macro-MOFs prepared from GO and MOF also showed excellent performance in metal removal. Due to their different component mass ratios and synergistic effects among components, composites tend to have more-advanced properties than single materials. In 2017, Mao et al. [30] reported a ZIF-8/rGO aerogel, which was synthesized

by a one-pot method via self-assembling rGO aerogel and NPs under the synergy of the chemical reduction process and metal ion crosslinking (Figure 3c). The ZIF-8/rGO aerogel, rapidly transforming into a hydrogel in wastewater, reached equilibrium for Pb(II) and Cd(II) within 4 min, and the maximum adsorption capacity was 101.1 and 281.5 mg/g, respectively. There are two reasons for the easy removal of HMs by the ZIF-8/rGO aerogel: firstly, the uniformly decorated ZIF-8 provided additional active sites for HM ions due to its high specific surface area, and secondly, the rGO aerogel was negatively charged due to the residual hydroxyl groups (-OH). Rao et al. [33] prepared a new adsorbent called IRMOF-3/GO with high adsorption capacity for Cu(II) (254.14 mg/g), and the adsorption was attributed to the coordination between the amine group (-NH₂) on IRMOF-3/GO and Cu(II). Then, they further fabricated a nanofiltration (NF) membrane (PSF@PDA@IRMOF-3/GO) via surface decorating the IRMOF-3/GO onto a PDA-coated polysulfone (PSF) substrate (Figure 3d). Surprisingly, the incorporation of IRMOF-3/GO onto PSF@PDA membrane could increase the zeta potentials and active sites of the pristine membrane surface, which enhanced the rejections between the composite membrane surface and salt solutions or HMs (e.g., Cu²⁺, Pb²⁺, Ni²⁺, Co²⁺ and Fe³⁺) (Figure 3e–g). Additionally, the composite displayed higher rejections against HMs than common salt ions due to electrostatic repulsion and adsorption, while the metal salt ions were only rejected by electrostatic effects. A similar study has been reported for the rejection of Cu(II) by an amine-modified MOF@GO composite called f-ZIF-8@GO, which removed an exceptionally high amount of Cu(II) (1872.24 mg/g) [34]. Meanwhile, Zhang et al. [35] successfully combined UiO-66-(COOH)₂ and a partially reduced graphene oxide (prGO) to form a composite named UiO-66-(COOH)₂/prGO NF. The material also showed excellent rejection of Cu(II) (96.5–83.1%) and Cd(II) (92.6–80.4%).

3.1.2. Adsorption Behavior of MOF Derivatives

Limited studies have used MOF derivatives to remove cations from aqueous solutions. Song et al. [72] discovered a novel magnetically separable 3D hierarchical carbon-coated nickel nanocomposite (Ni@C), which was fabricated by calcinating the Ni-based MOF (Ni₃(OH)₂(C₈H₄O₄)₂(H₂O)₄). Results showed that the nanocomposite had excellent adsorption capacity for Pb(II) (92.5 mg/g), Cu(II) (63.4 mg/g), and Cd(II) (41.4 mg/g), respectively. The adsorbent can be easily separated from the solution by using an ordinary common magnet without external energy. Additionally, Chen et al. [66] synthesized a nanoporous adsorbent ZnO/ZnFe₂O₄/C by using Fe(III)-modified MOF-5 as both the precursor and the self-sacrificing template. The ZnO/ZnFe₂O₄/C presented better Pb(II) adsorption capacity (344.83 mg/g) than the ZnO@SiO₂@Fe₃O₄/C NPs (54.6 mg/g). They proposed that a part of Zn(II) on the adsorbent surface was dissolved out of the ZnO crystal, and thus the residual oxygen group on the surface of ZnO could be combined with Pb(II) through the ion exchange process.

3.2. Typical Anionic HMs

Although there are fewer types of anionic HMs in aqueous solutions, they show similarities to cationic metals in that they are also present in low concentrations in the environment and are accumulative. The common anionic HMs in the environment are arsenic (As) and chromium (Cr), whose speciation is heavily dependent on the environmental pH. Arsenic (mainly As(V) and As(III)) exists in the form of oxygen-containing anions (e.g., H₂AsO₃⁻, HAsO₃²⁻, H₂AsO₄⁻, and HAsO₄²⁻). Generally, the toxicity of As(III) is higher than that of As(V), and the removal of As(III) requires a complex oxidation process to transfer it to As(V) [74]. Chromium in aqueous solution mainly exists as the higher oxidation state Cr(VI) (including CrO₄²⁻, Cr₂O₇⁻ and HCrO₄⁻). Only under the reductive condition can the Cr(VI) be converted to Cr(III). In contrast to As, Cr(VI) toxicity is higher than that of Cr(III). Past work on MOF-based materials employed to remove anionic HMs is summarized in Table 3.

Table 3. Summary of adsorptive capability of MOF-based materials for Cr (Cr(III) or Cr(VI)) and As (As(III) or As(V)) in water.

MOF-Based Materials	Target HMs	Q _e (mg/g) or Removal Rate (%)	Reusability	Mechanism	Ref.	
Core-shell composites	Fe ₃ O ₄ @ZIF-8	As(III)	100	Reusable	Ligand exchange Chemical bonding (Zn-O-As)	[74]
	β-MnO ₂ @ZIF-8	As(III)	140.27	Reusable	Electrostatic attraction Oxidation-adsorption Chemical bonding (As-O)	[44]
	MOF-NZVI	As(III)	360.6	Reusable	Oxidation-adsorption Chemical bonding (As-O)	[29]
	Fe ₃ O ₄ @UiO-66	As(V)	73.2	Reusable	Ion exchange Chemical bonding (As-O)	[75]
	Fe ₃ O ₄ @MIL-101	As(III) As(V)	121.5 80.0	Reusable	Oxidation/reduction-adsorption Chemical bonding (As-O)	[76]
	CoFe ₂ O ₄ @MIL-100(Fe)	As(III) As(V)	143.6 114.8	Not mentioned	Ion exchange Chemical bonding (As-O) Hydrogen bonding	[77]
	MIL-100(Fe) based filters	As(III) As(V)	90% 100%	Reusable	Oxidation-adsorption Fenton-like reaction	[78]
MOF derivatives	NiOx/Ni@C 300 400 500 600 Ni-MOF	As(V)	210.40 454.94 290.89 342.77 133.93	Reusable	Electrostatic interaction Chemical bonding (As-O)	[79]
Core-shell composites	MOR-1-HA	Cr(VI)	259	Reusable	Electrostatic interaction Ion exchange Coordination	[45]
	MP@ZIF-8	Cr(VI)	136.56	Reusable	Electrostatic interaction Adsorption-reduction Coordination	[46]
	CeO ₂ @UiO-66-(SH) ₂ CeO ₂ /Fe ₃ O ₄ @UiO-66-(SH) ₂	As Cd(II) Cr Cu(II) Pb(II) Hg(II)	56% 87% 93% 99% 99% 98%	Reusable	Electrostatic interaction Coordination Chemical bonding (Zr-O-As)	[32]
	BUC-21/TNTs	Cr(VI)	100% (20 min)	Reusable	Ion exchange Electrostatic interaction Photocatalysis-reduction Adsorption-reduction	[80]
	ZnO@ZIF-8	Cr(VI) MB	88% (240 min)	Not mentioned	Electrostatic interaction Photocatalysis-reduction Diffusion Adsorption-reduction	[50]
	MWCNT/NH ₂ -MIL-68	Cr(VI)	100% (120 min)	Reusable	Photocatalysis-reduction Diffusion Adsorption-reduction	[38]
	M@MIL-100(Fe)	Cr(VI)	100% (8 min)	Reusable	Photocatalysis-reduction Adsorption-reduction	[81]
	Fe ₃ O ₄ @UiO-66@UiO-67/CTAB	Cr(VI)	932.1	Reusable	Electrostatic interaction Hydrogen bonding van der Waals forces	[43]
MOF derivatives	PANI@NC	Cr(VI)	198.04	Reusable	Adsorption Coordination-reduction	[63]

Table 3. Cont.

MOF-Based Materials	Target HMs	Q _e (mg/g) or Removal Rate (%)	Reusability	Mechanism	Ref.
Ni@N-CNTs/NG	Cr(VI)	72.325	Reusable	Electrostatic interaction Diffusion Adsorption-reduction (HCOOH)	[82]
P-Fe ₂ O ₃	Cr(VI) Pb(II) Cu(II) Co(II)	175.5 97.8 66.2 60.4	Not mentioned	Electrostatic interaction Ion exchange Coordination	[62]
Fe _{0.72} ⁽⁰⁾ Fe _{2.28} ^(II) C	Cr(VI)	354.6	Reusable	Adsorption-reduction	[83]
NZVI@ZD	Cr(VI)	226.5	Not mentioned	Electrostatic interaction Diffusion Adsorption-reduction	[84]

3.2.1. Capture of As(III) and As(V)

In the past few years, MOF-based materials have shown excellent performance in removing aqueous As. Pristine MOFs such as MIL-100(Fe) [77,85], ZIF-8 [44,56,74], and UiO-66 [29,75] are commonly used as adsorbents; however, they have almost no oxidation performance for the removal of As(III). Before MOF composites were studied, the removal of As only depended on the interaction between the central metal ions of the MOFs and As(III or V) as well as the high surface area of MOFs.

Due to the more toxic nature of As(III), more efforts were devoted to fabricating MOF-based materials with exceptional adsorption and oxidation ability. The oxidative adsorption of As(III) and the simultaneous removal of As(III) and As(V) by MOF composites gradually have become more important [76,77]. An example of MOF composites for simultaneous rapid oxidation and adsorption of As(III) was reported by Jian and Wang [44]. They deposited ZIF-8 nanocrystals on β -MnO₂ nanowires and synthesized a one-dimensional β -MnO₂@ZIF-8 composite material. Compared with the pristine ZIF-8, the adsorption capacity of β -MnO₂@ZIF-8 for As(III) was significantly increased by 1.6 times (to 140 mg/g), which could be attributed to the high surface area (883 m²/g) of ZIF-8 and high oxidizing capacity of β -MnO₂ (Figure 4a,b). Importantly, the composite could be easily separated from the water after 30 min of settling, whereas the ZIF-8 was still suspended in the water (Figure 4c). Another material, named Fe₃O₄-ZIF-8, exhibited superior removal efficiency for As(III) (up to 100 mg/g at pH = 8) within a broad pH range (5–11) [74]. The authors elucidated that the adsorption between Fe₃O₄@ZIF-8 and As(III) resulted from the hydrolysis of ZIF-8, which produced a large number of external active sites (Zn-OH), and As(III) formed mononuclear or binuclear complexes with the Zn-OH through ligand exchange. Moreover, an iron (Fe) mesh-based MOF filter for removing As(III) and As(V) in groundwater was demonstrated by Wang's group [78]. In their study, 90% of As(III) and all As(V) were removed by the Fe-based MIL-100(Fe) filter after 6 h of filtration. In comparison, only 17% of As(V) and 10% of As(III) were removed by the original Fe mesh. Notably, the Fenton-like reactions were initiated by Fe²⁺/Fe³⁺ sites within the MIL-100(Fe) framework to oxidize As(III) to As(V). Recently, the highest adsorption capacity for As(III) was reported by Liu's group [29] using a MOF-nanoscale zero-valent iron (NZVI) composite (360.6 mg/g at pH = 7). Their study also showed a consistently high removal capacity for As(III) (>98.2%) between pH 3.0 and 12.0. In the presence of coexisting ions (e.g., Ca²⁺, Mg²⁺, Cu²⁺, PO₄³⁻, and SO₄²⁻), this material still showed good selectivity for As(III) in this pH range.

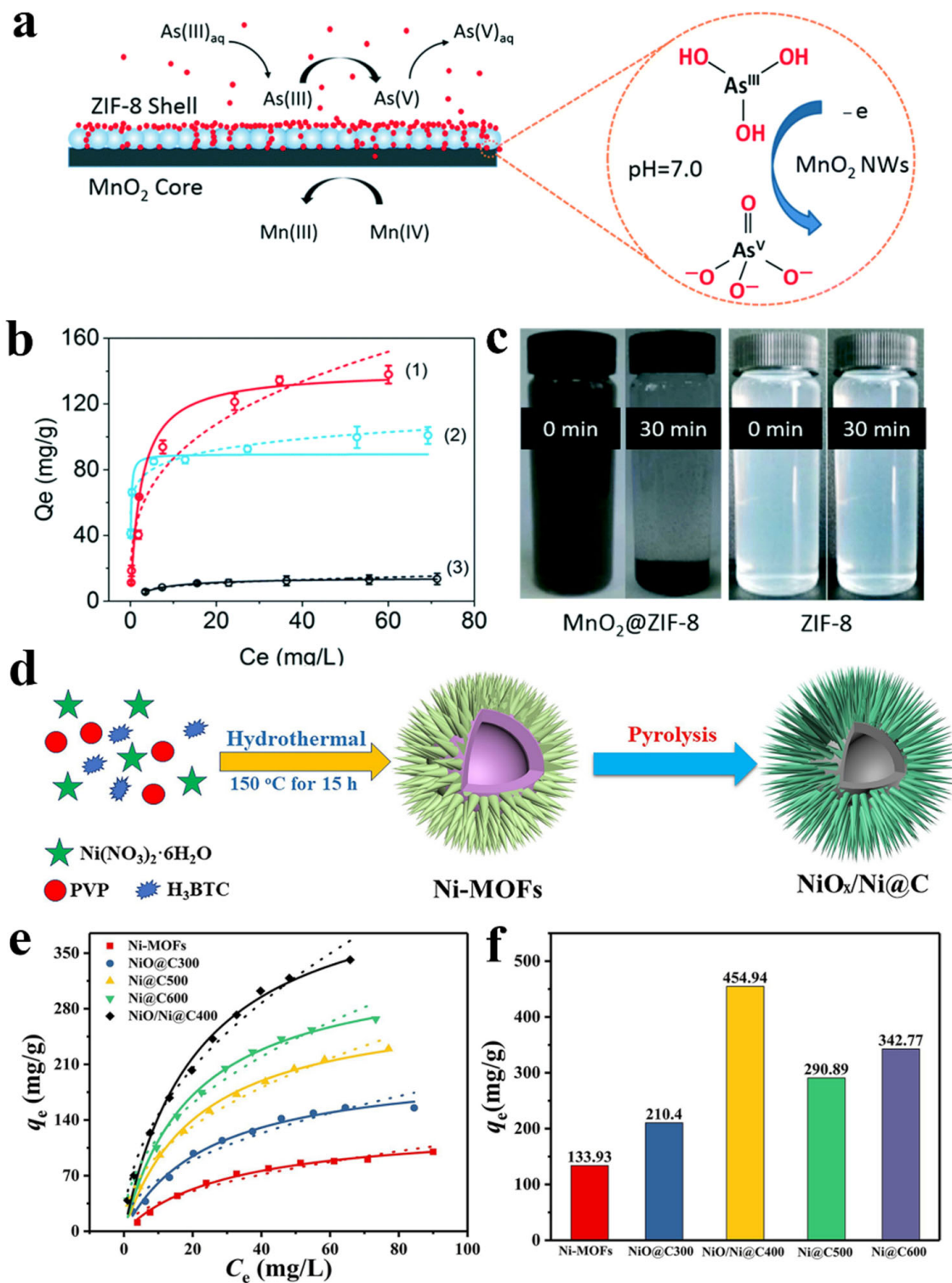


Figure 4. (a) Schematic illustration of the As(III) removal process on MnO_2 @ZIF-8 NWs. (b) Fitted adsorption isotherms of As(III) on (1) MnO_2 @ZIF-8 NWs, (2) ZIF-8, and (3) β - MnO_2 NWs. (c) Photographs of two vials containing MnO_2 @ZIF-8 NWs and ZIF-8 nanoparticles after gravity settling for 0.5 h in aqueous solution, respectively. Reprinted with permission from Ref. [44]. Copyright 2016, The Royal Society of Chemistry. (d) Schematic illustration of the synthesis of Ni-MOFs and $\text{NiO}_x/\text{Ni}@C$. (e,f) Adsorption isotherms and comparison of adsorption capacities of Ni-MOFs, $\text{NiO}@C300$, $\text{NiO}/\text{Ni}@C400$, $\text{Ni}@C500$, and $\text{Ni}@C600$ for As(V) removal. Reprinted with permission from Ref. [79]. Copyright 2019, Elsevier.

MOFs are also used as a self-sacrificed template to prepare various metal nanoparticles@carbon (MNP@C) for removal of As(V). The adsorption capacity of these MOF-derived nanomaterials seems to be superior to that of their pristine counterparts. For instance, Ni-MOF was pyrolyzed to form a series of magnetic chestnut shell-shaped hollow sphere structured composites (NiO_x/Ni@C) at different temperatures for As(V) removal [79] (Figure 4d). Results showed that the number of oxygen-containing functional groups on the surface of the material gradually decreased with increasing temperature, and the NiO_x gradually converted into Ni. Furthermore, NiO_x/Ni@C400 had the highest As(V) removal performance (454.94 mg/g) in the pH range of 1–10, compared to Ni@C600 (342.77 mg/g), Ni@C500 (290.89 mg/g), NiO@C300 (210.40 mg/g), and Ni-MOF (133.93 mg/g) (Figure 5e,f). However, there was also an exception of improved As removal by the MOF-derived material shown in the study of Liu et al. [85], where the α-Fe₂O₃ derived by calcining MIL-100(Fe) at different temperatures only removed 70–95 mg/g As(V), lower than that removed by the pristine MIL-100(Fe) (110 mg/g).

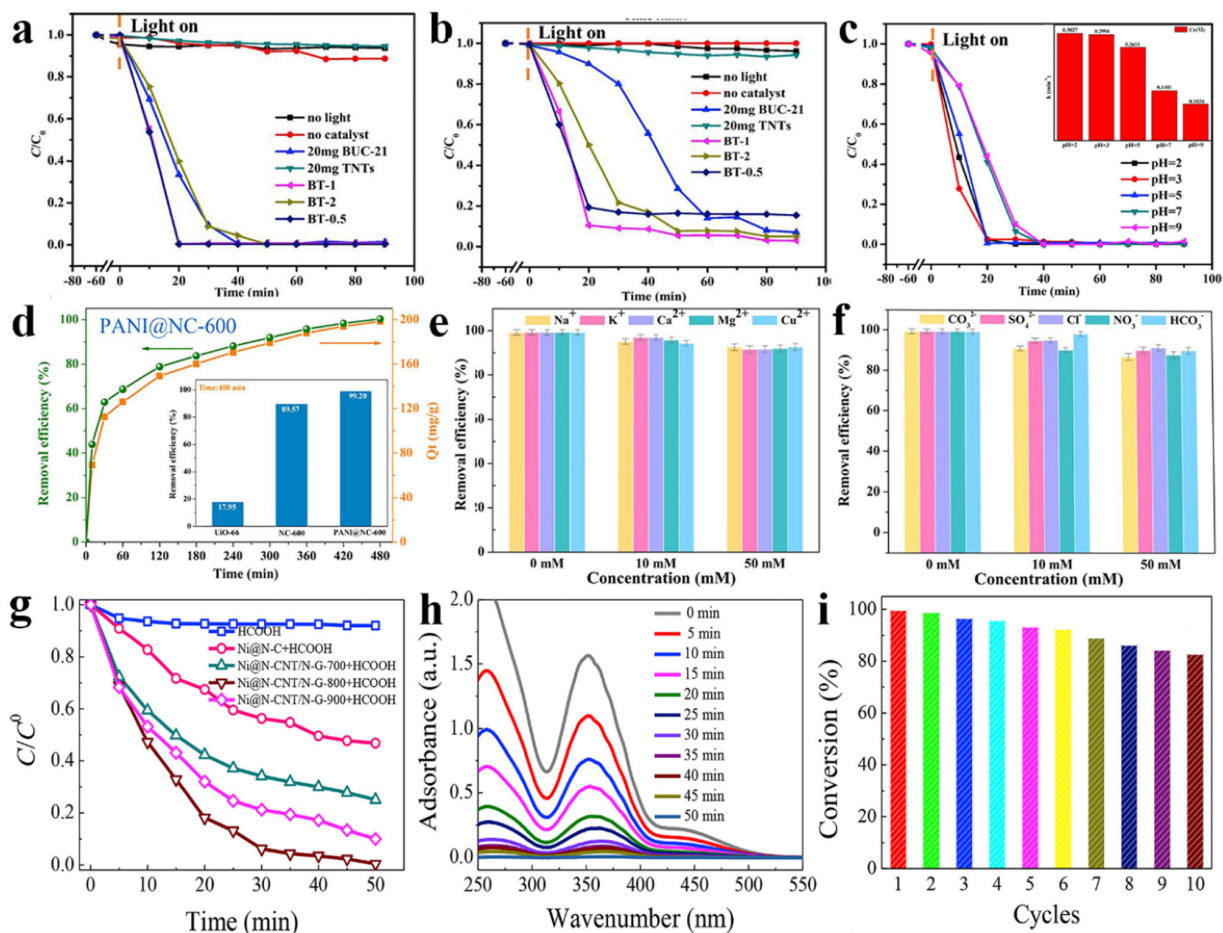


Figure 5. (a) Photocatalytic Cr(VI) reduction efficiencies and (b) total Cr removal efficiencies in control experiments and in the presence of different photocatalysts by BT-X. (c) Reduction of Cr(VI) under UV light irradiation at different pH by BT-X. Reprinted with permission from Ref. [80]. Copyright 2019, Elsevier. (d) Performance comparison of different adsorbents on Cr(VI) removal; inset shows the removal rate of Cr(VI) by UiO-66, NC-600, and PANI@NC-600 at 480 min. (e,f) Effects of different cations and anions on the removal efficiency of PANI@NC-600. Reprinted with permission from Ref. [63]. Copyright 2019, Elsevier. (g) The reduction of Cr(VI) in different systems. (h) Typical time-dependent UV-vis absorption spectra of Cr(VI) solution in Ni@N-CNTs/N-G-800/HCOOH system. (i) The catalytic stability of 3D Ni@N-CNTs/N-G-800. Reprinted with permission from Ref. [82]. Copyright 2019, Elsevier.

3.2.2. Capture of Cr (Cr(III) and Cr(VI))

In recent years, many studies pertaining to the removal of Cr(VI) have focused not only on non-catalytic adsorption but also on photocatalytic reduction-adsorption. It has been proved that the MOF-based materials can efficiently remove Cr substances from aqueous solution with a maximum adsorption capacity ranging from 72.35 mg/g to 932.1 mg/g [5,43,46,62,63,82,84].

The photocatalytic performance of MOFs for removal of Cr(VI) could be effectively improved by adding multi-wall carbon nanotubes (MWCNT) [38], graphene oxide (GO) [86], ZnO [50], noble metal [81], and titanate nanotubes (TNTs) [80], etc. The photocatalytic reactivity of MOFs is attributed to their large surface area and rich metal nodes as catalytic active sites [87]. For instance, Wang et al. [80] used two-dimensional BUC-21 and TNTs to prepare a series of MOF (BUC-21)/TNT composites (BT-X, X representing the mass ratio of BUC-21 and TNTs) with good photocatalytic performance. Experimental results revealed that the Cr(VI) concentration could be significantly affected by light, catalyst types (e.g., BUC-21 and BT-X), and pH value. In particular, BT-X displayed 100% photocatalytic Cr(VI) reduction performance within 20–100 min and excellent stability over a wide pH range (2–9) (Figure 5a–c). This was due to the synergistic effect of BUC-21 and TNTs, which promoted the removal of Cr(VI) through photocatalytic reduction and adsorption reactions. Moreover, Pi et al. [38] synthesized an MWCNT/NH₂-MIL-68-(In) composite (named PL-1). They found that the addition of MWCNT increased the mesoporous diffusion and visible light absorption of Cr(VI) by MOFs without changing the conduction band position. Thus, the photocatalytic kinetic constant of PL-1 was nearly three times that of the NH₂-MIL-68-(In). It was reported that M@MIL-100(Fe) (M = Au, Pd, or Pt) also had achieved similarly high photocatalytic reduction of methyl orange (MO) and Cr(VI) [81]. Especially, the Pt@MIL-100(Fe) could completely reduce the Cr(VI) within 8 min and degrade MO within 40 min, whereas only 69% of Cr(VI) and approximately 5% of MO (without H₂O₂) were reduced by MIL-100(Fe). The photocatalytic performance of MOFs has been widely discovered and applied to the photocatalytic reduction of Cr(VI), which provides a new field of vision for the reduction and adsorption of Cr(VI) polluted wastewater.

A large number of MOF derivatives were also used to remove Cr from water, such as NPC [63], metal@C [82,83], and metal oxide@C [62,84]. These materials inherit the high specific surface area and functionality of the MOFs, and they also have multiple advantages (e.g., high porosity and multiple active sites) of the carbon-based materials and metal NPs after high-temperature pyrolysis. Lai et al. [63] synthesized N-doped carbon (NC) materials (PANI@NC) by etching and in situ polymerization of polyaniline (PANI) on the carbonized UiO-66 (Figure 5d). They found that the removal rate of Cr(VI) exceeded 99% with the PANI@NC-600, and the maximum adsorption capacity reached 198.04 mg/g at pH = 1. They also reported that the competition effect of various cations (such as Na⁺, K⁺, Ca²⁺, Cu²⁺, and Mg²⁺) and anions (such as Cl⁻, CO₃²⁻, SO₄²⁻, and NO₃⁻) on Cr(VI) was small at high concentrations (Figure 5e,f). In the study of Fang et al. [84], NZVI@ZD was synthesized by the carbonization of a core-shell structured NZVI@ZIF-67. Owing to its high specific surface area and large pore size, favorable for Cr(VI) adsorption and diffusion, the maximum adsorption capacity of NZVI@ZD for Cr(VI) was surprisingly as high as 226.5 mg/g, surpassing that of the pristine ZIF-67 (29.35 mg/g) and NZVI@ZIF-67 (36.53 mg/g). Additionally, the Ni-MOF-derived N-doped graphene-CNT framework (Ni@N-CNTs/N-G) could catalyze the reduction of Cr(VI) to Cr(III) in the presence of formic acid (HCOOH) and removed both within 50 min [82] (Figure 5g,h). It could also maintain a removal efficiency of about 82.7% after 10 cycles (Figure 5i). The authors proposed that in the presence of the electron-donating acid (HCOOH), the dehydrogenation of HCOOH into atomic hydrogen and the reducing nitrogen/oxygen groups on the surface of the derivative played an important role in the reduction of Cr(VI). In general, porous carbon materials derived from MOFs possess high specific surface area and high activity, which facilitate Cr(VI) adsorption and transformation.

3.3. Possible Mechanisms of HM Removal

The synergistic effect between the composite elements and MOFs provides multiple mechanisms for the removal of HMs. For core–shell MOF composites and MOF derivatives, high adsorption efficiency is derived from the functional groups, central metal ions, and high specific surface area of the materials. These reactions are based on physical adsorption (including diffusion, electrostatic interaction, van der Waals forces, etc.) and chemical adsorption (including coordination interaction, Lewis acid–base interaction, ion exchange, and combined adsorption-oxidation/reduction, etc.) [84]. For the macro-MOFs, HMs are either adsorbed on the material or rejected directly during filtration because of the hydrogel or membrane technology. Like the previous two materials, the macro-MOFs also rely on the high specific surface area and active groups to trap HM ions. Additionally, the size repulsion effect of the macro-MOFs (especially MOF composite membrane) based on the material's pore diameter and the radius of the HM ions also endows the materials with high metal selectivity.

4. Remediation of OPs using MOF-Based Materials

4.1. Conventional Industrial Organics

Since the emergence of various manufacturing industries, conventional industrial OPs have troubled us as ubiquitous and persistent environmental pollutants. There are many types of conventional industrial organic chemicals, which are roughly divided into phenols, polychlorinated biphenyls (PCBs), polycyclic aromatic hydrocarbons (PAHs), aromatic compounds, etc. Conventional industrial organic chemicals are mostly highly toxic and persistent in the environment. They exist in water bodies at lower concentrations, but they are difficult to biodegrade and can be continuously enriched through the food chain. Long-term exposure can damage the body's immune system and cause various chronic diseases. Thus, researchers have developed various MOF-based materials to remediate industrial wastewater through adsorption and catalysis reactions.

In recent years, a large number of studies have shown that magnetic materials coupled with MOFs to form core–shell structured composites have been widely used in the removal of industrial organic pollutants. For nitroresorcinol (NRC) adsorption, Yang et al. [88] synthesized a new durian-shaped magnetic porous $\text{Fe}_3\text{O}_4@\text{SiO}_2@\text{UiO}-66$ composite (MSU(Zr)), which assembled UiO-66 onto Fe_3O_4 particles by the solvothermal method (Figure 6a). The results showed that the MSU(Zr) had excellent adsorption capacity (more than 200 mg/g) for NRC as a result of the high porosity of UiO-66 and the Lewis base nature of the $\text{Zr}_6\text{O}_4(\text{OH})_4$ clusters. Notably, better adsorption performance was found in acidic conditions. Niu et al. [89] successfully synthesized a core–shell $\text{Pd}@\text{Fe}_3\text{O}_4@\text{MOF}$ for degradation of chlorophenol and phenol. As shown in Figure 6b, the Fe_3O_4 NPs were first immobilized on the Pd NPs, forming a core–shell $\text{Pd}@\text{Fe}_3\text{O}_4$ hybrid material. Then, a hollow Fe-MOF was used to wrap the $\text{Pd}@\text{Fe}_3\text{O}_4$, obtaining a yolk/shell structure of $\text{Pd}@\text{Fe}_3\text{O}_4@\text{MOF}$. The Fe_3O_4 NPs and $\text{Pd}@\text{Fe}_3\text{O}_4$ hybrid particles in the shell were the active centers for catalyzing H_2O_2 Fenton reactions. The degradation rates of 2-chlorophenol and 2,4,6-trichlorophenol in the $\text{Pd}@\text{Fe}_3\text{O}_4@\text{MOF}$ catalyst were 100% and 75%, respectively. Additionally, the 4-chlorophenol, 2,4-dichlorophenol, and phenol were completely removed within 10 min (Figure 6c). After repeated use five times, the $\text{Pd}@\text{Fe}_3\text{O}_4@\text{MOF}$ catalyst could still completely degrade the 2,4,6-trichlorophenol within 3 h. Possible mechanisms of the TCP catalytic degradation by the $\text{Pd}@\text{Fe}_3\text{O}_4@\text{MOF}$ are shown in Figure 6d. The catalyst's core–shell cavity ensured rapid diffusion of the reactants, and the electron transfer of Pd to Fe_3O_4 accelerated the generation of $\cdot\text{OH}$ radicals inside the $\text{Pd}@\text{Fe}_3\text{O}_4$ hybrid material. In addition, the catalyst was easy to recycle due to its magnetic properties and reusability. The strategy of combining MOFs and magnetic particles provides a new direction for the remediation of industrial OPs in the future.

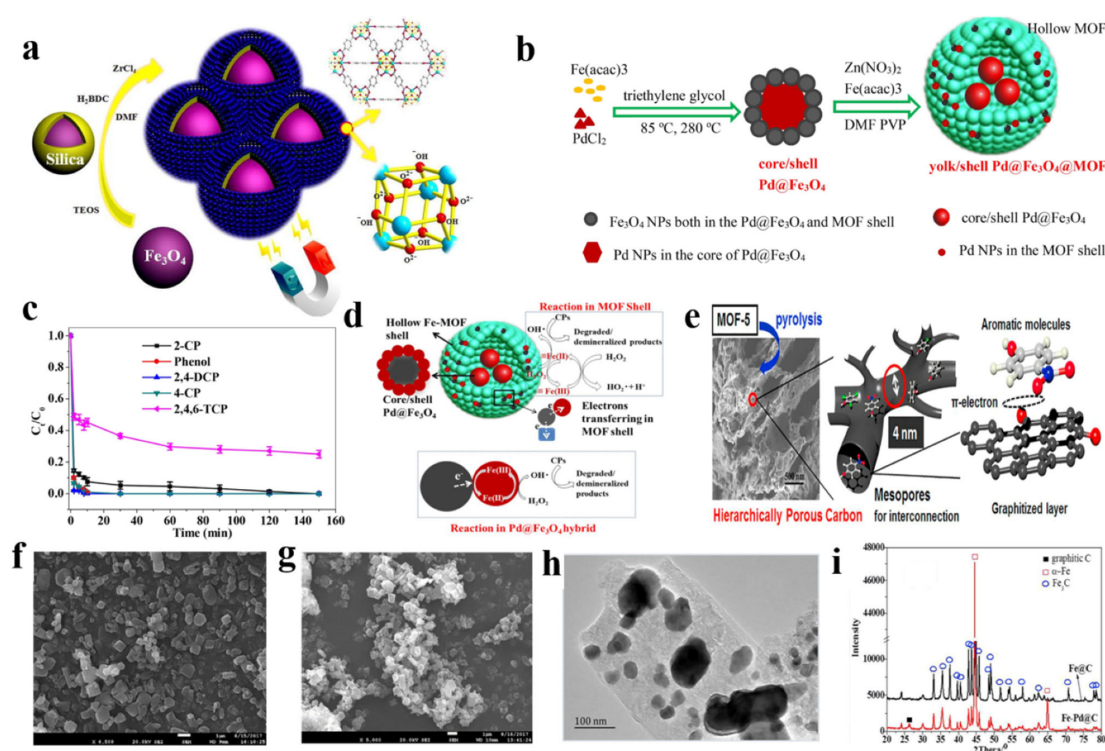


Figure 6. (a) Schematic of synthesis procedure for MSU(Zr). Reprinted with permission from Ref. [88]. Copyright 2017, Elsevier. (b) Preparation strategy for the yolk/shell Pd@Fe₃O₄@MOF nanocomposites. (c) Removal efficiency for different chlorophenols. (d) Possible mechanism of TCP degradation catalyzed by Pd@Fe₃O₄@MOF (condition: 1 mM H₂O₂, pH = 4). Reprinted with permission from Ref. [89]. Copyright 2018, Elsevier. (e) Schematic diagram of mechanism for adsorption of aromatic pollutants by LPC. Reprinted with permission from Ref. [90]. Copyright 2018, Elsevier. SEM images of Fe-MOFs prepared with (f) solvothermal method and (g) mechanochemical technique. (h) TEM images of Fe-Pd@C, (i) XRD patterns of Fe@C and Fe-Pd@C. Reprinted with permission from Ref. [91]. Copyright 2019, Elsevier.

Many MOF derivatives are being studied to remediate organic-polluted industrial wastewater. The porous carbon materials derived from MOFs can be used as excellent adsorbents in wastewater because of their large specific surface area, good stability, and low cost. Teng et al. [90] used MOF-5 as a template to synthesize layered porous carbon (LPC) by pyrolysis (950 °C) for the adsorption of aromatic pollutants. After high-temperature pyrolysis (950 °C), the MOF-5 became a layered porous carbon material (LPC) with higher porosity and better graphite structure (Figure 6e). The graphitized layer had a high affinity for the π electrons on the aromatic ring, exhibiting a large adsorption capacity for aromatic compounds (even double that of the activated carbon). The adsorption of aromatic compounds by LPC was a spontaneous, endothermic physical adsorption reaction.

MOF derivatives can also be used as catalysts to generate corresponding free radicals to degrade industrial OPs in wastewater. For instance, He et al. [91] successfully prepared a core/shell Fe-Pd@C nanocomposite to strengthen the Fenton degradation of phenol by Fe-MOF using a mechanochemical method. Scanning electron microscope (SEM) results showed that the resultant Fe-MOF had a morphology similar to that produced by the traditional solvothermal methods (Figure 6f,g). Transmission electron microscopy (TEM) results clearly showed that the hollow Fe-Pd@C particles were embedded in the large carbon shell (Figure 6h), which not only improved the stability of the metal NPs but also retained the catalytic ability. Graphitized carbon, Fe⁰, and Fe₃C were effectively detected through the X-ray powder diffraction (XRD) analysis of the Fe@C and Fe-Pd@C (Figure 6i). The Fe-Pd@C nanocomposite could continuously and permanently act as an Fe source for oxidizing phenol by Fenton reaction, in which H₂O₂ was decomposed into

hydroxyl radicals ($\cdot\text{OH}$) due to the internal micro-electrolysis between the Fe^0 and carbon components. More importantly, the core/shell structure of Fe-Pd@C ensured the effective transfer of electrons from Fe to the carbon electrode and avoided the termination of micro-electrolysis inside the Fe-C, which improved the catalytic performance and service life compared to the traditional Fe/C materials. Similarly, Ahsan et al. [92] also found a highly active, recyclable and magnetic C@Co nano-catalyst to degrade MO and 4-Nitrophenol. This synthesis strategy successfully fixed magnetic Co NPs uniformly on the porous carbon matrix, retaining the catalytic activity of the Co NPs to a large extent.

In all, MOF composites and MOF derivatives have good application prospects for remediating conventional industrial OPs. How to design stable, highly active, and reusable MOF-based materials is a key point for future research.

4.2. Organic Dyes

Organic dyes are a serious pollutant in water bodies, mainly from the textile, paper, leather, plastics, rubber, medicine, printing, and dye manufacturing industries [93]. Organic dyes are synthetic aromatic compounds that can be simply divided into cationic and anionic dyes [94]. Organic dyes remaining in water can cause severe damage to the human brain, central nervous system, liver, kidneys, and reproductive system. Some toxic and even carcinogenic organic dyes can exist in the environment for a long time due to their chemical stability, adversely affecting the survival and reproduction of microorganisms and animals living in water [94,95]. Thus, various MOF composites and MOF derivatives have been studied and applied to the remediation of organic dyes in water.

4.2.1. Adsorption Behavior of MOF-Based Materials

In the actual application process, the nano-sized adsorption materials are difficult to separate and reuse. The combination of MOFs and magnetic metal NPs can render the MOFs magnetized for facile collection [96]. For example, Liu et al. [97] combined magnetic Fe_3O_4 NPs and $\text{NH}_2\text{-MIL-101(Al)}$ to adsorb different kinds of anionic and cationic dyes. The results showed that the large adsorption capacities of the magnetic $\text{NH}_2\text{-MIL-101(Al)}$ for malachite green (MG) and indigo carmine (IC) were 274.4 and 135 mg/g, respectively. Huang et al. [71] successfully synthesized an amino-modified Zr-based magnetic MOF composite (Zr-MFC) by the in situ growth method. According to the study, the Zr-MFC had high adsorption capacity for methylene blue (MB) (128 mg/g) and MO (219 mg/g) in an aqueous solution. The material was easy to recycle, and the adsorption capacity remained unchanged after six cycles, indicating great application potential. Yang et al. [98] proposed to grow ZIF-67 shells on the surface of Fe_3O_4 NPs by introducing polystyrenesulfonate (PSS), and the as-formed novel type of $\text{Fe}_3\text{O}_4\text{@MOF}$ (MZIF-67) was used for removing MO from an MO/MB mixture solution (Figure 7a). It could be seen that the ZIF-67 crystals were covered on the surface of Fe_3O_4 NPs (Figure 7b,c), and the petal-like MZIF-67 had a size between 50 and 100 nm. The characteristic peaks of MZIF-67 were highly consistent with those in Fe_3O_4 and ZIF-67 crystals, further verifying the integrity of the composite structure (Figure 7d). Study results also showed that the MZIF-67 had a stronger adsorption capacity for MO (up to 738 mg/g) than many other MOF adsorbents. Since the solution pH may change the form of MO and the surface charge density of MZIF-67, too high or too low pH was not conducive to MO adsorption (Figure 7e). Combining the zeta potential of MZIF-67 and the influence of pH on adsorption (Figure 7e–g), the possible mechanism of selective adsorption was proposed. The selective adsorption of MO was mainly attributed to the electrostatic interaction between the positively charged MZIF-67 and anionic MO. Meanwhile, the cationic MB stayed away from the MZIF-67 because of electrostatic repulsion. Shi et al. [99] also reported the adsorption of MG on an Fe_3O_4 NP-doped magnetic MOF composite named $\text{Cu-MOF/Fe}_3\text{O}_4$ (113.67 mg/g). In short, the magnetic MOF composites formed by the combination of magnetic NPs and MOFs are convenient for recycling and have good application prospects for the adsorption of organic dyes in wastewater.

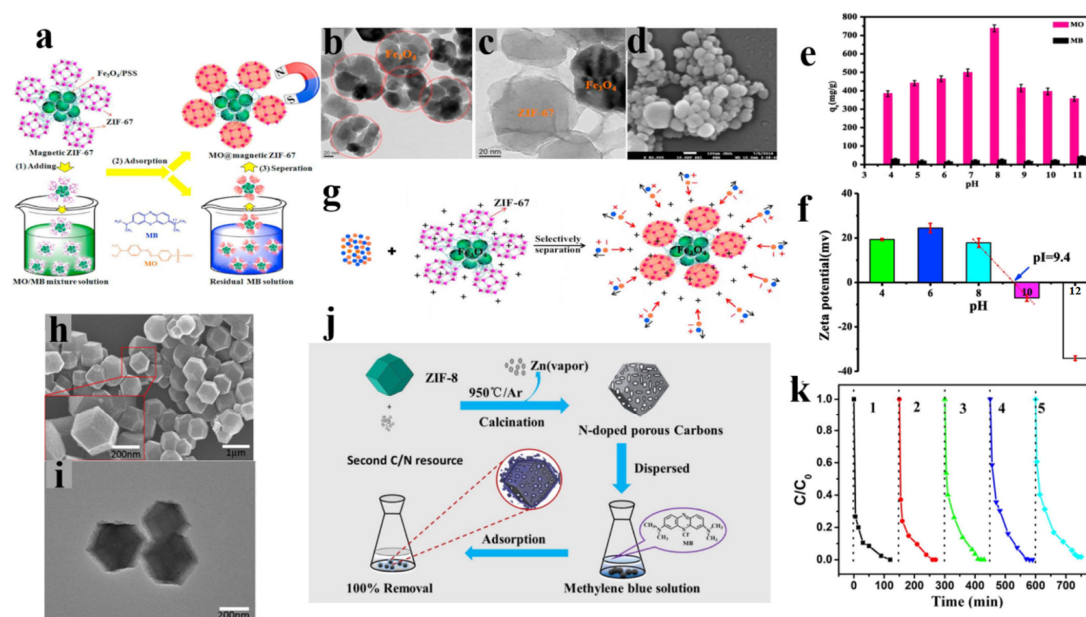


Figure 7. (a) Schematic illustration of selective removal of MO from MO/MB mixed solution by MZIF-67. TEM images of (b) Fe_3O_4 and (c) MZIF-67; (d) FESEM images of MZIF-67. (e) pH effects on MO and MB adsorption of MZIF-67. (f) Zeta potential of MZIF-67. (g) Selective adsorption mechanism illustration of MB/MO mixture dyes by MZIF-67. Reprinted with permission from Ref. [98]. Copyright 2017, Elsevier. (h) SEM image and (i) TEM image of Carbon-ZD. (j) Schematic illustration of the fabrication process of N-doped porous Carbons and adsorption of MB. (k) Regeneration and reuse of Carbon-ZD. Reprinted with permission from Ref. [100]. Copyright 2017, Elsevier.

To expand the specific surface area and porosity for fast and efficient adsorption, MOFs can also be converted into corresponding derivatives through calcination and pyrolysis. Generally speaking, the pyrolysis of MOFs in inert gas can produce metal/carbon hybrid materials and carbon materials, and direct calcination of MOFs in air can produce nano-metal oxide. For example, Xu et al. [100] used ZIF-8 as a template to synthesize three N-doped porous carbon adsorbents (i.e., Carbon-Z, Carbon-ZS, and Carbon-ZD) for the treatment of MB in wastewater. The preparation of N-doped porous carbon was divided into two steps (Figure 7j): firstly, the ZIF-8 was added to a methanol solution containing sucrose and dicyandiamide to obtain the ZIF/sucrose and ZIF/dicyandiamide composites; Secondly, the ZIF-8, ZIF/sucrose and ZIF/dicyandiamide composites were pyrolyzed under 950°C argon atmospheres to form Carbon-Z, Carbon-ZS, and Carbon-ZD, respectively. Compared with the original ZIF-8 (Figure 7h,i), the Carbon-ZD sample after high-temperature pyrolysis retained its original diamond-shaped dodecahedron structure, but the carbonization significantly increased the material's specific surface area (Carbon-ZD $1796.5\text{ m}^2/\text{g}$ vs. ZIF-8 $1451.8\text{ m}^2/\text{g}$). Results also showed that the Carbon-ZD was a promising MB adsorbent with a saturated adsorption capacity of up to 1148.2 mg/g and good reusability (Figure 7k). More importantly, the removal rate of MB was still close to 100% when MO and MB coexisted in the wastewater, indicating the strong anti-interference ability of the Carbon-ZD. Song et al. [72] studied an effective adsorbent Ni@C nanocomposite, which was obtained by pyrolyzing the sheet-like porous MOF precursor $\text{Ni}_3(\text{OH})_2(\text{C}_8\text{H}_4\text{O}_4)_2(\text{H}_2\text{O})_4$. The synthesized Ni@C had a large specific surface area of $120.38\text{ m}^2/\text{g}$ and evenly dispersed Ni on its 3D-layered lamellar porous structure. The Ni@C was not easy to agglomerate and had good adsorption of rhodamine B (RhB) within 10 min (99%). In all, MOF composites and MOF derivatives usually have stronger adsorption capacity and higher stability than the original MOF (Table 4). Using a MOF as a template to prepare various MOF derivatives by calcination and pyrolysis can produce excellent adsorbents for the removal of organic dyes in wastewater.

Table 4. Brief summary of MOF-based materials for organic dye removal.

MOF-Based Materials	MOF Precursors	Removal Type	Organic Dyes	Performance	Reusability	Mechanism	Ref.
MOF composites							
GO/MOFs	Ni-MOF	Adsorption	MB	274 mg/g for MB	It could be used at least five times after washing with ethanol.	Electrostatic interaction and acid–base interaction	[101]
Ni-MOF/GO	Ni-MOF	Adsorption	CR	2489 mg/g for CR	Not mentioned	Electrostatic interaction, acid–base interaction	[102]
MFC-N	UiO-66	Adsorption	MB	128 mg/g for MB	There was no obvious loss of MFC adsorption capacity after 6 cycles.	Electrostatic attraction interaction	[71]
MFC-O			MO	219 mg/g for MO			
Magnetic NH ₂ -MIL-101(Al)	MIL-101(Al)	Adsorption	MG IC	274.4 mg/g for MG 135 mg/g for IC	The removal rate of MG and IC decreased slightly after 5 cycles.	Electrostatic interaction, π - π stacking interaction and hydrogen bonding	[97]
POM@MOF	Cu ₃ (BTC) ₂	Adsorption	MB	77.22 mg/g for MB	Not mentioned	Electrostatic attraction	[103]
Cu-MOFs/Fe ₃ O ₄	Cu-MOFs	Adsorption	MG	113.67 mg/g for MG	MG removal rate could still reach 90% after 5 cycles.	Physical adsorption	[99]
MZIF-67	ZIF-67	Adsorption	MO	738 mg/g for MO	Not mentioned	Electrostatic interaction	[98]
Fe ₃ O ₄ @MIL-100(Fe)	MIL-100(Fe)	Adsorption	MB	73.8 mg/g for MO	Adsorption did not decrease significantly after 5 cycles.	Not mentioned	[104]
Fe ₃ O ₄ @MIL-100(Fe)	MIL-100(Fe)	Photocatalytic degradation	MB	99.77% photodegradation for MB within 200 min	The photocatalytic activity had no obvious loss after repeated use.	Photogenerated holes (h ⁺), photoelectron transfer, ·OH	[105]
Fe ₃ O ₄ @MIL-101(Fe)	MIL-101(Fe)	PMS degradation	AO7	Degraded completely within 60 min	The removal rate of AO7 ranged from 98.1% to 95.0% in 3 cycles.	SO ₄ ^{•−} , ·OH, ·O ₂ [−]	[106]

Table 4. Cont.

MOF-Based Materials	MOF Precursors	Removal Type	Organic Dyes	Performance	Reusability	Mechanism	Ref.
UiO-66/g-C ₃ N ₄	UiO-66	Photocatalytic degradation	MB	100% photodegradation for MB within 240 min	Not mentioned	·O ₂ ⁻	[107]
ZIF-67/PAN	ZIF-67	PMS degradation	AY	95.1% degradation rate within 10 min	The catalytic effect remained stable (above 98%) after 5 cycles.	SO ₄ ^{•-}	[108]
ZIF@R	ZIF-67	PMS degradation	RhB	Removed completely within 20 min	No loss of catalytic activity of ZIF@R after 5 cycles.	SO ₄ ^{•-} and ·OH	[109]
ZIF-9@GEL	ZIF-9	PMS degradation	RhB	99% degradation rate within 10 min	The degradation performance did not decrease significantly (about 90%) after 3 cycles.	SO ₄ ^{•-} and ·OH	[110]
ZIF-12@GEL	ZIF-12						
MOF derivatives							
Ni@C	Ni-MOF	Adsorption	RhB	Almost 99% adsorption for RhB within 10 min	Not mentioned	van der Waals forces, hydrogen bonding	[72]
Ni/PC-CNT	Ni/Zn-MOF	Adsorption	MG CR	898 mg/g for MG 818 mg/g for CR	The adsorption rate of Ni/PC-CNT for MG and CR remained above 85%.	π-π interaction and electrostatic interaction	[111]
MWCNTs	Co-MOF	Adsorption	CR	1639 mg/g for CR	Not mentioned	Hydrogen-bonding interactions, π-π stacking interactions and the effect of mesopores	[112]
Carbon-ZD	ZIF-8	Adsorption	MB	1148.2 mg/g for MB	The adsorption efficiency of the Carbon-ZD for MB was still very high after 5 cycles.	Nitrogen doping and electrostatic interaction	[100]
Carbon-ZS				791.3 mg/g for MB			
Carbon-Z				505.3 mg/g for MB			

Table 4. Cont.

MOF-Based Materials	MOF Precursors	Removal Type	Organic Dyes	Performance	Reusability	Mechanism	Ref.
Co-BiFeO ₃	PABs	Photocatalytic degradation	MO	Nearly 89.8% degradation rate in 120 min	The degradation rates in 4 cycles were 89.8%, 86.3%, 83.5% and 81.4%, respectively.	A larger range of light response and more oxygen vacancies	[80]
NPCs	ZIF-8 NH ₂ -MIL-53 IRMOF-3	PMS degradation	MO RhB	100% MO and 90% RhB were removed by NPC/PMS within 60 min.	Not mentioned	Excellent electron transfer ability of graphite nitrogen	[113]
NPC-800	ZIF-8	PMS degradation	RhB	The degradation rate of RhB was 85.0%.	The removal rate of RhB decreased slightly from 85.0% to 68.8% after 3 cycles.	SO ₄ ^{•-} and ·OH	[114]
PNC-800	Zn-Co PBA ₅	PMS degradation	MB RhB OII	The degradation rate was 100%, 92.8 and 93.2%, respectively.	PNC-800 has good catalytic stability after 3 cycles.	Non-radical process	[115]
MCCI	Co/Fe-MOF	PMS degradation	RhB	80% degradation rate within 30 min	The catalytic effect remained good after 6 cycles.	SO ₄ ^{•-}	[116]
Fe ₃ O ₄ @C/Cu	HKUST-1	Photocatalytic degradation	MB	Completely removed within 150 min	The photocatalytic activity had no obvious loss after 5 cycles	Photoelectron transfer and ·OH	[117]
MCG	ZIF-67	PMS degradation	AY	Completely decolorized within 30 min	The removal rate remained 97.6% after 50 cycles.	SO ₄ ^{•-} and ·OH	[118]

4.2.2. Catalytic Behavior of MOF-Based Materials

Due to their central catalytic metal ions and unique porous structure, MOFs can be used as excellent templates/precursors to prepare various catalysts (e.g., NPC, metal@C materials, and metal oxide@C materials).

MOFs exhibit semiconductor properties under visible light and can be used as a new type of environmental purification cationic photocatalyst [119]. In recent years, MOF composites have made significant progress as a kind of photocatalyst for the degradation of organic dyes. For example, Qiu et al. [105] developed a novel multifunctional magnetic Fe_3O_4 @MIL-100(Fe) core-shell composite to decolorize MB. They successfully packaged Fe_3O_4 NPs into the MIL-100(Fe) in a controlled manner through a layer-by-layer strategy. In the yolk-shell structure of Fe_3O_4 @MIL-100(Fe) (Figure 8a,b), the Fe_3O_4 acted as the core, and the MIL-100(Fe) was the shell. The photodegradation rate of Fe_3O_4 @MIL-100(Fe) for MB could reach 99.77% within 200 min under visible light (Figure 8c). Under the same conditions, the activity was equivalent to that of the traditional photocatalyst TiO_2 but far better than C_3N_4 (10.45%). Cycle experiments (Figure 8d) and XRD analysis (Figure 8e) proved that the photocatalytic reactivity and structure of Fe_3O_4 @MIL-100(Fe) had almost no change after five cycles of use, indicating good long-term stability. The possible mechanism of Fe_3O_4 @MIL-100(Fe) photocatalytic degradation is given in Figure 8f. Under visible light irradiation, electrons in the valence band (VB) of MIL-100(Fe) were excited and transferred to the conduction band (CB), consequently generating holes (h^+) that could directly oxidize the adsorbed MB. The photogenerated electrons then activated the $\text{H}_2\text{O}_2/\text{H}_2\text{O}$ system to generate a large number of $\cdot\text{OH}$ radicals, which could also be used to oxidize MB. Nevertheless, they hindered the effective recombination of electrons and holes. The magnetic properties of Fe_3O_4 @MIL-100(Fe) core-shell microspheres were also studied by vibrating sample magnetometry (VSM) (Figure 8g). The Fe_3O_4 @MIL100(Fe) showed a magnetic hysteresis loop with a magnetic susceptibility of 34.70 emu/g. In addition, the sample dispersed in the water could be quickly attracted to the magnet in 5 sec, which successfully solved the problem of separation.

MOFs can also be used as ideal precursors for the production of nano-metals and metal oxides through calcination and pyrolysis. Another study by Qiu's group successfully reported Fe_3O_4 @C/Cu and Fe_3O_4 @CuO composite materials [117], produced by pyrolyzing the magnetic Fe_3O_4 @HKUST-1 in N_2 atmosphere and air, respectively. Interestingly, the Fe_3O_4 @C/Cu pyrolyzed in the N_2 atmosphere had a remarkably larger specific surface area ($31.06 \text{ m}^2/\text{g}$) than the Fe_3O_4 @CuO ($0.0233 \text{ m}^2/\text{g}$). It is well-known that traditional Fe_3O_4 and TiO_2 semiconductors have low photocatalytic utilization efficiency due to the high charge-carrier recombination rate [120]. In contrast, metal NPs can absorb visible light and have a lower Fermi level, thereby acting as suitable electron acceptors. In this study, carbon, as a sensitizer, could quickly transfer photoexcited electrons from Fe_3O_4 to Cu NPs, while photo-generated holes were still located on the Fe_3O_4 microspheres, which greatly reduced the probability of electron-hole recombination. Therefore, the Fe_3O_4 @C/Cu exhibited excellent photocatalytic activity for MB degradation compared with Fe_3O_4 @CuO, g- C_3N_4 , Fe_3O_4 , and TiO_2 powders in the study.

Zeolitic imidazolate framework (ZIF), as a typical MOF of abundant and ordered N species, represented by ZIF-8 and ZIF-67, has been considered as an ideal precursor for porous NC due to its thermally stable carbon skeleton and N-containing ligand 2-methylimidazole [121]. Ma et al. [114] successfully synthesized N-doped porous carbon (NC-800) by pyrolyzing ZIF-8 under an N_2 atmosphere (Figure 8h). As shown in Figure 8i,j, the NC-800 still retained the rhombic dodecahedron morphology of the ZIF-8 crystal during pyrolysis, but its N-doping weight (15.20%) was much higher than that produced by one-pot synthesis using melamine or urea as the N source [122]. A free radical quenching experiment (Figure 8k) revealed that the main mechanism during the process of peroxy-monosulfate (PMS) activation by NC was the large amount of sulfate and $\cdot\text{OH}$ produced rather than electron transfer. Nevertheless, the NC-800 catalyst had medium reusability, as shown by the slightly decreased RhB removal rate (about 68.8%) in the second and third

runs compared to the first run (Figure 8l). The reduced catalytic performance was due to the decrease in the relative content of N and the large increase in oxygen content in the NC-800. Interestingly, the catalytic activity of NC-800 could be completely restored after being heat-treated in the air at 350 °C for 1 h. Wang et al. [113] prepared various NC materials with different N content using three N-rich MOFs (i.e., ZIF-8, NH₂-MIL-53, and IRMOF-3), and the as-formed materials were used to activate PMS for degradation of phenol, bisphenol A (BPA), MO, and RhB. Due to the presence of N, the NC materials showed better catalytic performance for PMS than the N-free porous carbon. This was mainly because the graphite N in the NC could activate adjacent carbon atoms more effectively, thereby promoting the adsorption and dissociation of PMS. In short, the use of pyrolysis to produce MOFs as carbon precursors to activate PMS provides a new idea for future advanced oxidation processes.

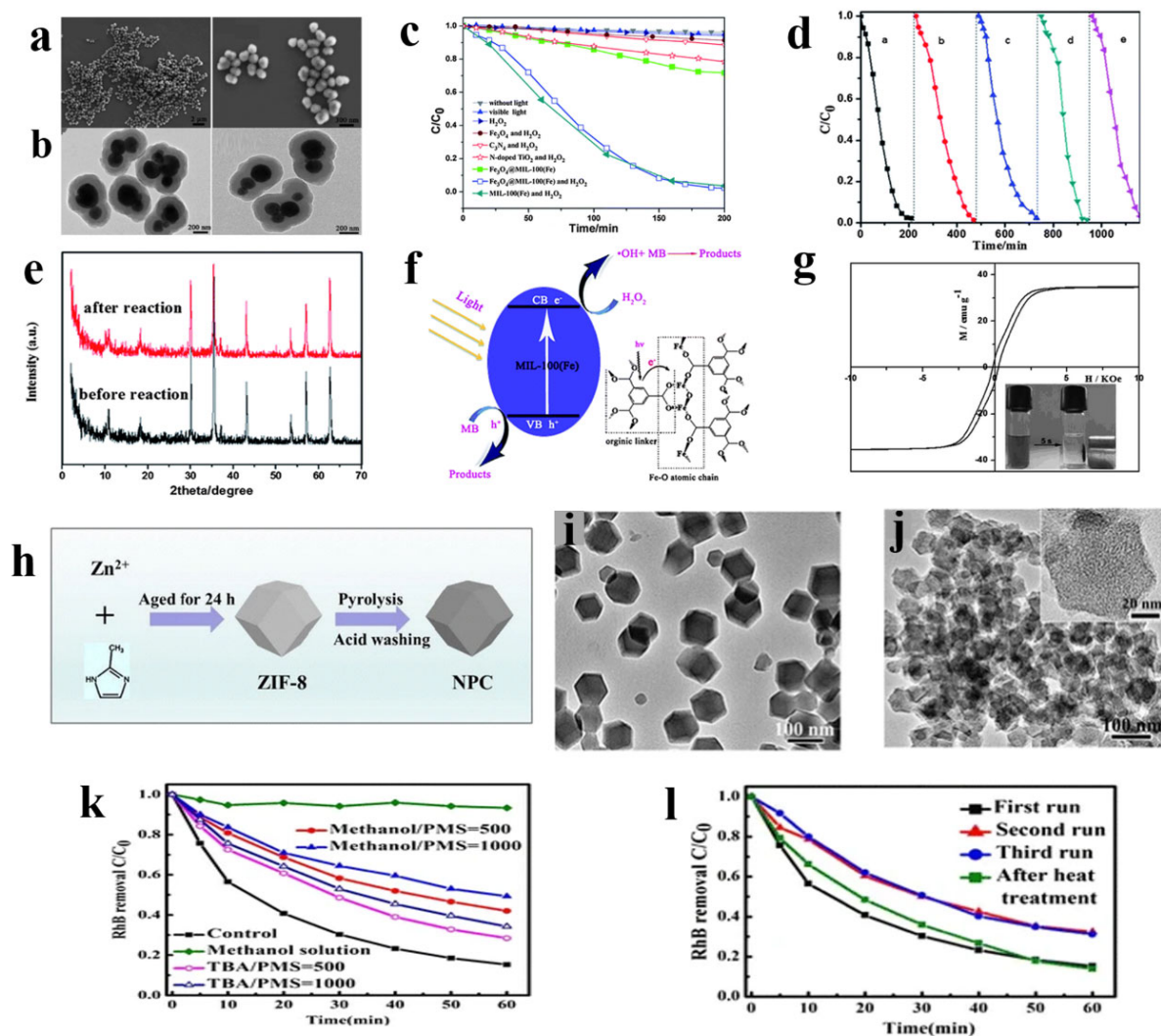


Figure 8. (a) SEM and (b) TEM images of Fe₃O₄@MIL-100(Fe). (c) Photodegradation with different catalytic conditions under visible light irradiation. (d) Five degradation cycles of MB. (e) PXRD patterns for Fe₃O₄@MIL-100(Fe) before and after reaction. (f) Schematic illustration of the principle of MB photodegradation under light irradiation. (g) Room temperature magnetization curves of the Fe₃O₄@MIL-100(Fe) microspheres at 300 K. Reprinted with permission from Ref. [105]. Copyright 2013, The Royal Society of Chemistry. (h) Schematic illustration of synthesis (NC). TEM images of (i) ZIF-8 and (j) NC-800. (k) Radical quenching tests using methanol and TBA as the quenching. (l) Stability tests of NC-800 for RhB removal. Reprinted with permission from Ref. [114]. Copyright 2017, Springer-Verlag Berlin Heidelberg.

4.3. Pesticides

As pest and weed control chemicals, pesticides play a vital role in plant growth and agricultural production [123]. Broadly speaking, pesticides refer to chemical agents used to prevent, eliminate, or control diseases, insects, grasses, and other organisms that harm agriculture and forestry and purposefully regulate plant growth [124–126]. According to their treatment targets, pesticides can be divided into herbicides, insecticides, fungicides, and growth regulators [124].

With their extensive use in the environment, pesticides have brought severe environmental pollution and ecological risks. Most pesticides (e.g., aldrin, DDT, and chlorobenzenes) contain persistent organic pollutants (POPs) that accumulate in the environment and are difficult to degrade [127]. Residual pesticides mainly exist in soil, sediments, surface water, and groundwater. They can be continuously enriched in animals through the food chain and eventually enter the human body. According to Kim's investigation [126], many diseases, including cancer, leukemia, and asthma, are closely related to pesticide exposure. Notably, people with low immunity (such as children, pregnant women, or the elderly) are more susceptible to pesticide-induced harm. Hence, it is important to choose a suitable remediation method to remove pesticide residues in the environment.

4.3.1. Adsorption Behavior of MOF-Based Materials

MOF-based materials can be extensively used in the adsorption of pesticides in aqueous environments. However, the high production cost of MOFs inhibits their wide application. In comparison, natural materials are often inexpensive and available from a wide range of sources. Hence, the combination of natural materials and MOFs to produce low-cost and efficient adsorption materials is worthy of research. According to Abdelhameed's study [128], they first prepared a Cu-BTC@cotton composite by assembling a cotton fabric with Cu-BTC MOF and used it for ethion insecticide adsorption. Characterization analysis proved that Cu-BTC was successfully combined with the cotton fabric through the interaction between Cu and cellulose functional groups. The adsorption of ethion insecticide by the Cu-BTC@cotton conformed to the Langmuir model, and the saturated adsorption capacity was as high as 182 mg/g. The adsorption of ethyl ions was carried out by both physical and chemical adsorption, including the coordination of sulfur (on the ethyl group) with Cu (on the Cu-BTC), and the hydrogen bond formation between oxygen (on the ethyl group) and cellulose. The Cu-BTC@cotton is an excellent absorbent material for organochlorine pesticides in water, which will afford new research directions in the use of MOFs and textiles to mitigate pesticide pollution in water.

MOF composites prepared by combining MOFs with functional carbon materials and/or metal NPs can also have improved adsorption capacity. Wang et al. [129] successfully synthesized a new type of magnetic NP (i.e., $\text{Fe}_3\text{O}_4@\text{SiO}_2\text{GO-MOFs}$) based on a simple green solvothermal method. In the study, Cu-MOFs and SiO_2 coated Fe_3O_4 NPs were loaded on a platform of GO nanosheets through chemical bonding. The as-formed material possessed the large specific surface area of GO, the magnetism of Fe_3O_4 , and the high porosity and adjustability of a MOF. The study results also showed that the magnetic $\text{Fe}_3\text{O}_4@\text{SiO}_2\text{GO-MOFs}$ could effectively enrich six typical insecticides (i.e., imidacloprid, carbendazim, metalaxyl, myclobutanil, tebuconazole, and cyfluthrin), suggesting potential application value for alleviating pesticide pollution in the environment. Similar research was also reported by Xu's group [130]. They prepared a new type of magnetic Cu-based MOF using $\text{Fe}_3\text{O}_4\text{-GO-}\beta\text{-CD}$ nanocomposite as a magnetic core and carrier. The composite showed excellent removal performance for neonicotinoid pesticides in water bodies (almost completely removed within 1 h).

4.3.2. Catalytic Behavior of MOF-Based Materials

Though MOFs exhibit semiconductor behavior, the relatively large bandgap of MOFs and the high electron-hole recombination severely limit their photocatalytic performance [131]. Based on this, narrow bandgap semiconductors such as Ag/AgCl, Ag/AgIO₃, or Ag/AgPO₄

can be fixed on MOFs to improve their light absorption performance and catalytic activity. For example, Oladipo and co-workers [132] successfully developed a sunlight-driven $\text{AgIO}_3/\text{MIL-53}(\text{Fe})$ nano-hybrid photocatalyst by combining AgIO_3 and MOFs through an ultrasonic method. The nano-hybrid photocatalyst had high photocatalytic activity for methyl malathion and chlorpyrifos with degradation rates of 93–97% within 120 min, which were much higher than that of AgIO_3 (45–75%) and $\text{MIL-53}(\text{Fe})$ (50–68%). To improve the light absorption capacity of ZIF-8, a visible light active photocatalyst named $\text{Fe}_3\text{O}_4\text{-COOH@ZIF-8/Ag/Ag}_3\text{PO}_4$ was successfully synthesized by either a hydrothermal, solvothermal, or in situ precipitation method for photocatalytic degradation of diazinon [133]. In the study, ZIF-8 was introduced to grow in situ on the surface of carboxylate-modified Fe_3O_4 NPs for the first time. Then, the as-synthesized $\text{Fe}_3\text{O}_4\text{-COOH@ZIF-8}$ core-shell was combined with Ag_3PO_4 and Ag NP composite. As a result, the $\text{Fe}_3\text{O}_4\text{-COOH@ZIF-8/Ag/Ag}_3\text{PO}_4$ could remove 99.7% of diazinon and maintain high photocatalytic activity and stability after five cycles. Using three masking agents for quenching (i.e., ethylenediaminetetraacetate ($\text{Na}_2\text{-EDTA}$), p-benzoquinone (BZQ), and isopropanol (IPA)) showed that holes (h^+) and superoxide radicals ($\cdot\text{O}_2^-$) were the main active species in the photocatalytic degradation process. The electron-hole pairs were effectively separated by the synergistic effect between the surface plasmon resonance of Ag NPs and the ordered energy transfer through the Z-scheme mechanism.

Bimetal MOFs use two metals as the center to help adjust the electronic state of the catalyst [134,135]; thereby, their catalytic activity and stability are improved compared with single-metal MOFs. Ye et al. [136] selected the transition metals cobalt (Co) and Ni to synthesize three MOFs (i.e., Co-MOF, Ni-MOF, and Co/Ni-MOF) by a simple hydrothermal method. The catalytic degradation of atrazine by Co/Ni-MOF (93.3% removal) was far better than that of the Co-MOF and Ni-MOF in the catalytic ozone oxidation reaction. This was because the Co/Ni-MOF catalyst had a multi-metal center, higher coordination unsaturation, higher electron density, and higher electron transfer efficiency than the Co-MOF and Ni-MOF. Surprisingly, there was a redistribution of the electron density, migrating from Co to Ni because the electronegativity of Ni was higher than that of Co. The high electron density in the metal center contributed to the formation of oxygen-containing groups (hydroxyl groups) on the surface [136]. The authors speculated that both the surface hydroxyl groups and unsaturated coordination sites on the MOF contributed to the catalytic activity of the Co/Ni-MOF.

4.4. Pharmaceuticals and Personal Care Products

Pharmaceuticals and personal care products (PPCPs), as typical emerging contaminants, have caused widespread concern, because they are frequently detected in surface water and groundwater, and sometimes even in drinking water [137,138]. The presence of PPCPs in the environment was first detected in the 1980s [138,139]. So far, there are about 12,000 PPCPs for human use in the world [140], which can be roughly divided into anti-inflammatory medicines, analgesics, antibiotics, beta-blockers, anti-depressants, blood lipid regulators, disinfectants, and fragrances. Currently, the existing PPCPs in the environment are mainly broad-spectrum antibacterial agents (such as antibiotics, sulfonamides, quinolones, etc.), anti-inflammatory drugs and analgesics (carbamazepine, diclofenac, ibuprofen, etc.), and endocrine disrupting chemicals (steroid estrogen, bisphenols, etc.). According to a current survey in Australia, many antibiotic drugs, such as tetracycline (TC), erythromycin and sulfa drugs, were found in wastewater [141]. Méndez-Arriaga et al. [142] also reported that non-steroidal anti-inflammatory drugs were frequently detected in collected water samples. Although these PPCPs in the environment are mostly at trace concentrations (ng/L to $\mu\text{g/L}$), long-term exposure to such chemicals will cause potential harm to the ecosystem and public health. Most notably, the widespread use and abuse of broad-spectrum antibacterials have made antibiotic resistance a major issue of public health concern [140,143]. However, the traditional sewage treatment process (i.e., coagulation, flocculation, and sedimentation) may be unable to effectively remove various

PPCPs in wastewater. Therefore, highly selective and significant removal of PPCPs from the environment remains a major challenge.

4.4.1. Adsorption Behavior of MOF-Based Materials

Due to the simple operation and no secondary pollution, adsorption to directly remove PPCPs in sewage is considered one of the most feasible and effective methods. As porous materials with high adsorption capacity and stable performance, MOFs are a good choice for the adsorption of PPCPs. Recently, the approach using MOFs as templates to prepare MOF composites and derivatives in various ways has been widely applied to remove PPCPs in wastewater (Table 5).

Table 5. Summary of MOF-based materials as adsorbents for removal of PPCPs.

MOF-Based Materials	MOF Precursors	Q_e (mg/g)	Adsorption Thermodynamics	Adsorption Kinetics	Reusability	Mechanism	Ref.
MOF composites							
Fe ₃ O ₄ @MIL-100(Fe)	MIL-100(Fe)	CIP 278.39	Langmuir model	Elovich model and pseudo-second-order model	Not mentioned	Chemisorption and physical adsorption	[144]
Fe ₃ O ₄ @MOF-235(Fe)	MOF-235(Fe)	CIP 187.48	Langmuir model	Elovich model	Not mentioned	Physical adsorption	[144]
MIL-101/Fe ₃ O ₄	MIL-101(Cr)	CIP 63.28	Langmuir and Freundlich models	Pseudo-second-order model	Not mentioned	Film diffusion and intraparticle diffusion	[145]
MWCNT/MIL-53(Fe)	MIL-53(Fe)	TCN 363.37 OTC 325.59 CTC 180.68	Langmuir model	Pseudo-second-order model	The adsorption of TCs did not change obviously after 4 cycles.	π - π interaction, pore/size-selective adsorption and influence of metal ions	[146]
UIO-66-(OH) ₂ /GO	UIO-66	TC 37.96	Freundlich model	Pseudo-second-order model	Not mentioned	Electrostatic interaction, π - π interaction, hydrogen bonding and acid-base interaction	[147]
UIO-66/CA	UIO-66	LOFX 86.43	Langmuir model	Pseudo-second-order model	The adsorption efficiency of LOFX was still above 70% even after 5 cycles.	Not mentioned	[148]
Al-MOF/SACS	Al-MOF	BPA 136.9	Freundlich model	Pseudo-second-order model	The adsorption efficiency of BPA remained above 96% after 5 cycles.	π - π stacking, hydrogen bonding and cation- π interaction	[149]
NFe ₃ O ₄ @Zn(GA)/Starch-Hydrogel	Zn-MOF	FLV 782.05	Langmuir model	Pseudo-second-order model	The adsorption capacity decreased to 700.09 mg/g after 5 cycles.	Not mentioned	[150]

Table 5. Cont.

MOF-Based Materials	MOF Precursors	Q _e (mg/g)	Adsorption Thermodynamics	Adsorption Kinetics	Reusability	Mechanism	Ref.
Ni/Co-MOF@CMC aerogel	Ni/Co-MOF	TC 624.87	Langmuir model	Pseudo-second-order model	Not mentioned	Surface hydroxyl interaction, complexation of metal ions and oxygen	[151]
MOF derivatives							
PCN-222	Zr-MOFs	CAP 379	Not mentioned	pseudo-second-order model	Not mentioned	H-bond interaction, electrostatic interaction and the special pore structure of PCN-222	[152]
PCN-134	Zr-MOFs	DF 604.1	Langmuir model	Pseudo-second-order model.	The removal rate was above 95% after 7 cycles.	Not mentioned	[153]
CDMs	MAF-6	IBP 408 DCF 503	Langmuir model	Pseudo-second-order model.	The adsorption decreased slightly after 1 cycle, but basically unchanged from 2 to 5 cycles.	van der Waals and hydrophobic interactions	[78]
BMDCs	bio-MOF-1	ATLN 522 CLFA 540	Langmuir model	Pseudo-second-order model	The adsorption of ATLN did not decrease appreciably after 4 cycles.	ATLN: Electrostatic interactions CLFA: H-bonding and electrostatic interactions	[154]
CDIL@AIPCP	Al-MOF	PCMX 338 TCS 326	Langmuir model	Pseudo-second-order model	The adsorption efficiency did not decrease seriously with the increase in the number of cycles.	H-bonding	[155]
Co ₃ S ₄	ZIF-67	CIP 471.7	Langmuir model	Pseudo-second-order model and liquid-film diffusion model	There was no obvious loss in CIP removal after recycling five times.	Electrostatic interaction	[156]
NC-800	Zn-ZIF-L	TC 347.06	Langmuir model	Pseudo-second-order model	The adsorption of TC could maintain a high level after 4 cycles.	Electrostatic interaction and hydrogen bond interaction	[157]
MDC-1000	ZIF-8	SMX 435	Langmuir model	Pseudo-second-order model	The adsorption capacity decreased slightly after 1 cycle, but was unchanged from 2 to 4 cycles.	H-bonding	[158]
NPC	ZIF-8	CIP 416.7	Freundlich model	Pseudo-second-order model	The adsorption of CIP had no obvious loss after 7 cycles.	Electrostatic interactions, hydrophobic interactions	[159]

It is well known that most MOFs are in nano to micron scale, making them difficult to separate and recover from aqueous media. Therefore, nano-scale MOFs have certain limitations for large-scale commercialization and industrial applications. Some strategies have been studied to overcome these shortcomings [144,148–150]. For example, Moradi et al. [144] reported $\text{Fe}_3\text{O}_4@\text{MIL-100}(\text{Fe})$ and $\text{Fe}_3\text{O}_4@\text{MOF-235}(\text{Fe})$ for ciprofloxacin (CIP) removal. The synthesis strategy of loading magnetic oxidized metal NPs onto MOFs not only preserves the adsorption active sites but also endows the materials with magnetism for separation. A study by Mohamed's group [150] successfully manufactured an $\text{NFe}_3\text{O}_4@\text{Zn}(\text{GA})/\text{starch-hydrogel}$ by wrapping the starch hydrogel matrix on the MOF and doping it with nano-magnetite. Results showed that the $\text{NFe}_3\text{O}_4@\text{Zn}(\text{GA})/\text{starch-hydrogel}$ had a maximum adsorption capacity of 782.05 mg/g for FLV statin drug. In addition to hydrogels, aerogels with porous structures can also combine with MOFs to facilitate the rapid removal of PPCPs. For example, Li et al. [151] successfully prepared a Ni/Co-MOF@CMC aerogel for TC removal. Based on the synthesis strategy, a high-porosity 3D sodium carboxymethylcellulose (CMC) aerogel was selected as the carrier for the in situ growth of Ni/Co-MOF (Figure 9a). The Ni/Co-MOF@CMC aerogel kept the same 3D porous structure as the original CMC aerogel (Figure 9b), but the color of the hybrid material changed from the original white to light green. It verified that the Ni/Co-MOF had successfully grown in situ on the CMC aerogel without destroying the original 3D porous structure. The as-formed Ni/Co-MOF@CMC aerogel had a good adsorption capacity for TC (up to 624.87 mg/g).

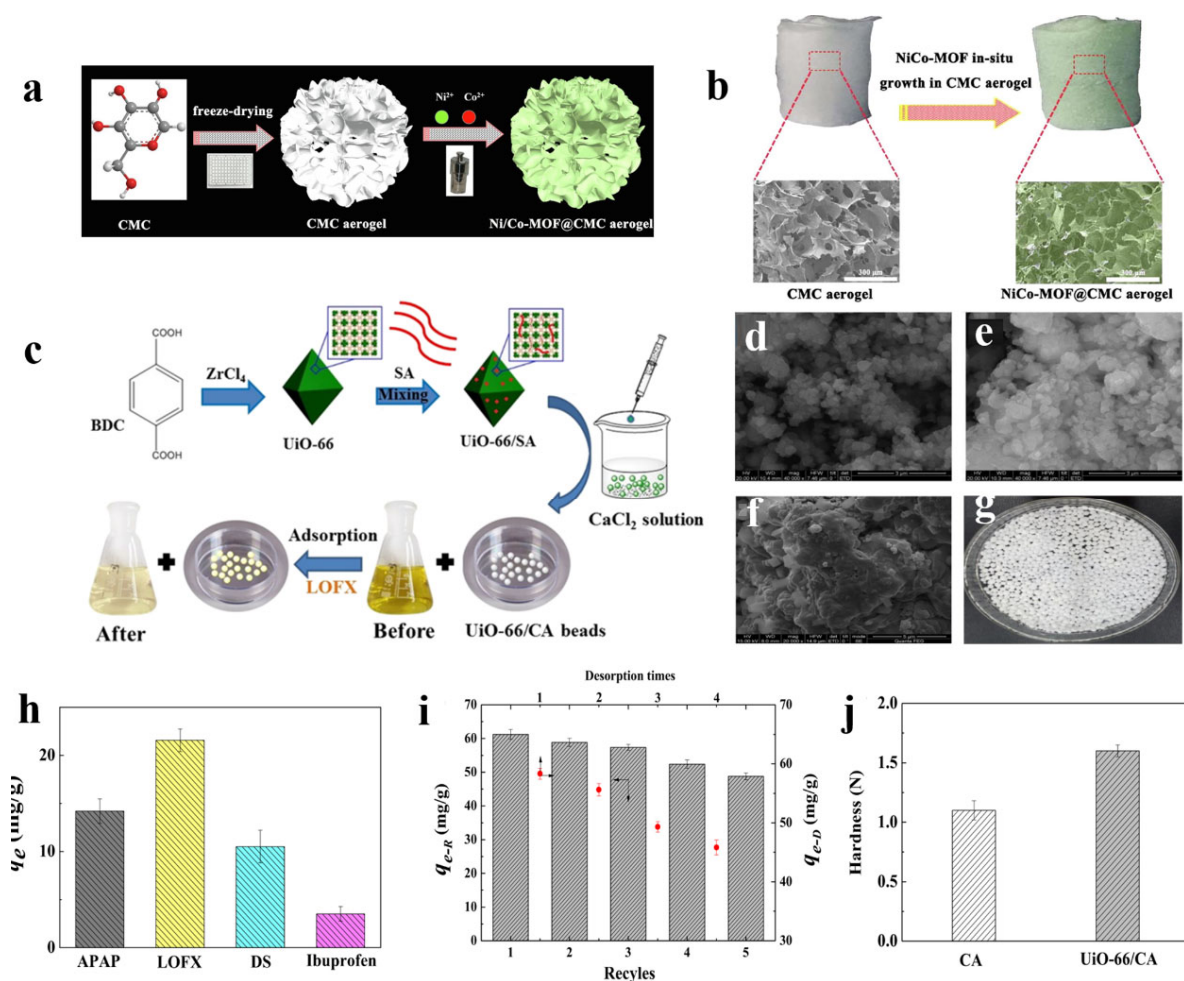


Figure 9. (a) Schematic diagram of the preparation of Ni/Co-MOF@CMC aerogel. (b) Photographs and SEM images of the CMC aerogel and Ni/Co-MOF@CMC aerogel. Reprinted with permission from Ref. [151]. Copyright 2019, Elsevier. (c) Schematic of the fabrication of UiO-66/CA. SEM images

of (d) UiO-66, (e) UiO-66/CA powder and (f) UiO-66/CA beads. (g) Photographs of UiO-66/CA. (h) Adsorption selectivity of UiO-66/CA microbeads. (i) The reusability of UiO-66/CA for LOFX adsorption. (j) The hardness of dry CA and UiO-66/CA microbeads. Reprinted with permission from Ref. [148]. Copyright 2019 Springer.

More interestingly, Sun et al. [148] successfully prepared UiO-66/calcium alginate (CA) beads by using a CaCl_2 solution solidification method to combine sodium alginate and UiO-66 for the first time. The entire preparation process and adsorption experiment are illustrated in Figure 9c. The SEM images in Figure 9d–f showed the difference in the morphology of UiO-66, UiO-66/CA powder, and UiO-66/CA beads. The original spherical particles of the UiO-66 formed an agglomerated structure after modification, and the inter-particle gaps were filled with the alginate. The size of the UiO-66/CA beads was about 3 mm (Figure 9g). Experimental results (Figure 9h) showed that the UiO-66/CA could selectively remove the target drug levofloxacin (LOFX). It also had higher adsorption capacity for LOFX (21.57 ± 1.18 mg/g) than for the other three drugs (i.e., acetaminophen (APAP) (14.20 ± 1.28 mg/g), diclofenac sodium (DCF) (10.52 ± 1.70 mg/g), and ibuprofen (IBP) (6.51 ± 0.76 mg/g)). A recycling experiment (Figure 9i) showed that the adsorption capacity slightly decreased with the increased number of cycles, but the activity and effectiveness were always maintained above 79%. The mechanical strength of UiO-66/CA beads was far better than that of the original CA beads (Figure 9j). Therefore, the UiO-66/CA bead was an efficient and reusable LOFX adsorbent. To further enhance the adsorption performance and make full use of sodium alginate and chitosan, Luo et al. [149] introduced chitosan during the preparation of MOF beads and successfully prepared Al-MOF/SA-CS composite beads for BPA adsorption. The introduction of chitosan increased the beads' porosity and further increased the adsorption capacity from 100.8 mg/g to 136.9 mg/g. Noteworthy, it was found that methanol could effectively recover and regenerate the adsorbed composite beads, which had high value for commercial applications.

Using MOFs as a template, NPC materials are also excellent adsorbents for removing PPCPs. Li et al. [159] used ZIF-8 as a template to produce NPC through a one-step carbonization method to adsorb CIP in water. The results indicated that the NPC-700 had the best adsorption performance (416.7 mg/g), far better than that of graphene oxide (379 mg/g) [160], $\text{Fe}_3\text{O}_4/\text{C}$ (74.68 mg/g) [161], multi-walled carbon nanotubes (150.6–206.0 mg/g) [162], and surface-modified carbon (60–300 mg/g) [163]. Both Langmuir and Freundlich models could fit the adsorption data well, but the latter had a higher degree of correlation, implying that there was multilayer adsorption on the surface of NPC-700. The NPC-700 also good stability and recyclability, as evidenced by the negligible change in adsorption efficiency after seven cycles of use. Adsorption mechanism investigation revealed that the electrostatic interaction and hydrophobic interaction between the NPC and CIP played a significant role in the adsorption. Similarly, An et al. [78], Ahmed et al. [158], and Sarker et al. [155] also reported the use of MOF-derived NPC for the adsorption of PPCPs. Therefore, the MOF-derived NPC had excellent adsorption performance and stability and could be used as a potential adsorbent to remediate PPCPs.

4.4.2. Catalytic Behavior of MOF-Based Materials

In recent years, MOF-based materials have been extensively studied for PPCPs in various catalytic degradation environments due to their unique structure and central metal ions. In particular, they are mostly used for persulfate (PMS/PS) activation, photocatalysis, and Fenton-like degradation. A summary of the MOF-based materials used in recent years for the catalytic degradation of PPCPs is provided in Table 6.

Table 6. Summary of MOF-based materials as catalysts for removal of PPCPs.

MOF-Based Materials	MOF Precursors	Catalytic Type	PPCPs	Degradation Rate	Reusability	Mechanism	Ref.
MOF composites							
Cu-hemin MOFs/BN	Cu-MOF	Photo-PS degradation	BPA	99% within 30 min	The degradation rate of BPA dropped to 78% in the third cycle.	$\cdot\text{OH}$ and $\text{SO}_4^{\bullet-}$	[164]
MOF/CCAC	Fe/Ni-MOF	Photocatalytic degradation	TC	98% within 75 min	Photocatalysts were well-reused in ten on-off cycles.	$\cdot\text{O}_2^-$ and h^+	[165]
ZIF-9@GEL	ZIF-9	PMS degradation	TC	90% within 1 h	The degradation performance did not decrease significantly (about 90%) after 3 cycles.	$\text{SO}_4^{\bullet-}$ and $\cdot\text{OH}$	[110]
ZIF-12@GEL	ZIF-12						
Pd@MIL-100(Fe)	MIL-100(Fe)	Photocatalytic degradation	TEH IBP BPA	99.5% within 150 min 100% within 150 min 70% within 240 min	The photocatalytic activity did not obviously decrease after 4 cycles.	Photogenerated electron and $\cdot\text{OH}$	[166]
MIL-100(Fe)/TiO ₂	MIL-100(Fe)	Photocatalytic degradation	TC	92.76% within 10 min	Degradation rate of TC was similar after 5 cycles.	$\cdot\text{O}_2^-$ and $\cdot\text{OH}$	[167]
Co-MIL-53(Al)	MIL-53(Al)	PMS degradation	TC	94.0% within 120 min	Co-MIL-53(Al) showed good activity after 4 cycles.	$\text{SO}_4^{\bullet-}$ and 1O_2	[168]
Co-Fe PBAs@rGO	Co-MOF	PMS degradation	LVF	97.6% after 60 min	Degradation rate exhibited no significant decrease after 5 cycles.	$\text{SO}_4^{\bullet-}$	[169]
MOF derivatives							
YSCCSs	ZIF-67	PMS degradation	BPA	99.1% within 23 min	The degradation rate of BPA exceeded 90% after 7 cycles.	$\text{SO}_4^{\bullet-}$ and $\cdot\text{OH}$	[170]
ZIF-CN/ g-C ₃ N ₄	ZIF-67	Photo-PMS degradation	BPA	97% after 60 min	The degradation rate only decreased by 8% after 7 cycles.	h^+ , $\cdot\text{O}_2^-$, $\text{SO}_4^{\bullet-}$ and $\cdot\text{OH}$	[171]
Co@NC-800	ZIF-67	PMS degradation	TC	91.2% within 5 min	The degradation rate hardly decreased after 4 cycles.	$\text{SO}_4^{\bullet-}$, $\cdot\text{O}_2^-$ and 1O_2	[172]

Table 6. Cont.

MOF-Based Materials	MOF Precursors	Catalytic Type	PPCPs	Degradation Rate	Reusability	Mechanism	Ref.
Fe-N/C	ZIF-8	PMS degradation	BPF	97.1% within 90 min	The removal rate decreased to 94.9%, 61.3%, and 42.1% in 3 cycles.	1O_2	[173]
FeCu@C	[Fe, Cu] -BDC	Fenton-like degradation	SMT	100% within 90 min	Not mentioned	$\pi-\pi$ interaction, $\cdot OH$ and surface hydroxyl groups	[174]
DMOFs	MIL-100(Fe)	Ionizing radiation degradation	CEP-C SM	100% removal for CEP-C 95% removal for CEP-C	The removal rate of CEP-C and SMT decreased to 94% and 76% after 3 cycles, respectively.	$\cdot OH$	[175]
CoFe ₂ O ₄ NC	Co/Fe bi-MOFs	PMS degradation	BPA	Over 97% within 90 min	Catalytic capacity dropped significantly after the first cycle and could be restored after 400 °C calcination for 15 min.	SO ₄ ^{•-} and $\cdot OH$	[176]

The combination of MOFs and other materials can make full use of their respective advantages, overcome their own defects, and improve the composite's stability and catalytic performance. For example, Pi and colleagues [169] successfully synthesized a separable magnetic Co-Fe PBAs@rGO nanocomposite to activate PMS by a simple two-step hydrothermal method. The synthetic strategy of using graphene as a supporter greatly reduced the agglomeration of the Co-Fe Prussian blue analogue (PBA) NPs. The combination also retained the active sites of Co and Fe, which was beneficial to the catalytic degradation of levofloxacin hydrochloride (LVF). Results showed that the Co-Fe PBAs@rGO had a strong catalytic ability to activate PMS (97.6% LVF removed after 60 min) and good recyclability. A similar study was also reported by Chen's group [164]. They successfully deposited Cu-hemin MOFs on boron nitride (BN) through a one-step hydrothermal method. The synthesized Cu-hemin MOFs/BN catalyst was used for the Fenton-like degradation of BPA. Under visible light irradiation, more than 99% of BPA (40 mg/L) was degraded within 30 min. Kinetic experiments also revealed that the degradation rate of Cu-hemin-MOFs/BN for BPA was 37.5 times and 14.8 times that of BN and Cu-hemin-MOFs, respectively. The authors concluded that the $\cdot\text{OH}$ and $\text{SO}_4^{\bullet-}$ were the main species in the PS activation. As an excellent photosensitizer, hemin could also generate photo-generated electrons to initiate the decomposition of PS so as to produce $\text{SO}_4^{\bullet-}$ [177]. He et al. [167] successfully developed a novel magnetic composite, taking full advantage of the MIL-101(Fe) and TiO_2 . In the process of removing the target pollutant TC, the MIL-101(Fe)/ TiO_2 showed high catalytic performance, with 91.24% of TC degraded within 10 min. It was speculated that the TiO_2 could receive ultraviolet light under sunlight to generate a large number of $\cdot\text{O}_2^-$ and $\cdot\text{OH}$ groups, and the calcined Fe-MOF could also effectively reduce the recombination of electrons and holes. The synergy of the two ensured the excellent photocatalytic performance of the composite material.

Aside from the above-mentioned MOF composites, MOF derivatives (e.g., NPC, metal@C, and metal oxide@C) prepared by using MOFs as a sacrificial template also have high catalytic activity for degrading PPCPs. For example, Wu et al. [173] selected in situ Fe-doped ZIF-8 as a sacrificial template and prepared a series of Fe-N co-doped porous carbon catalysts (Fe-N/C) by pyrolysis. The Fe-N/C doped with an appropriate amount of Fe had a layered porous structure and abundant defects, which enhanced the N doping and conductivity. The Fe-N/C mainly activated PMS to produce singlet oxygen ($^1\text{O}_2$) as the active species, which had an excellent degradation effect on bisphenol F (BPF). However, the removal rate of BPF dropped significantly from 94.5% in the first cycle to 42.1% after three cycles. It was likely because the BPF and intermediate products covered the active centers on the catalyst. Luckily, the Fe-N/C catalytic activity could be restored (returned to a 77% removal rate) by simple heat treatment. The gradual loss of catalytic activity of the MOF-based carbon catalysts remains a major challenge in improving their durability and reusability. To this end, Yang and his group [171] successfully designed a heterostructure composite material by combining the ZIF-8 derived NC (ZIF-NC) with g- C_3N_4 for PMS-activated degradation of BPA. The integration of ZIF-NC and g- C_3N_4 effectively improved both the PMS activation ability and the g- C_3N_4 photocatalytic activity. The preparation process for the ZIF-NC/g- C_3N_4 hybrid composite is depicted in Figure 10a. Experimental results showed that the ZIF-NC/g- C_3N_4 exhibited high photocatalytic activity in the presence of PMS, where 97% of BPA was degraded within 60 min (Figure 10b). Radical trapping experiments (Figure 10c) suggested that $\cdot\text{O}_2^-$ and photogenerated holes were the main active species, but a small number of $\cdot\text{OH}$ and $\text{SO}_4^{\bullet-}$ were also present in the photocatalytic reaction. A possible degradation mechanism is proposed in Figure 10d. On the one hand, photo-generated electrons could directly reach the surface of ZIF-NC and react with the adsorbed PMS to generate $\text{SO}_4^{\bullet-}$; on the other hand, electrons could migrate to the surface of g- C_3N_4 , reducing O_2 for $\cdot\text{O}_2^-$ generation. The holes of g- C_3N_4 could also directly react with the BPA. The synthesis strategy provides a new idea for improving the PMS-assisted photocatalysis.

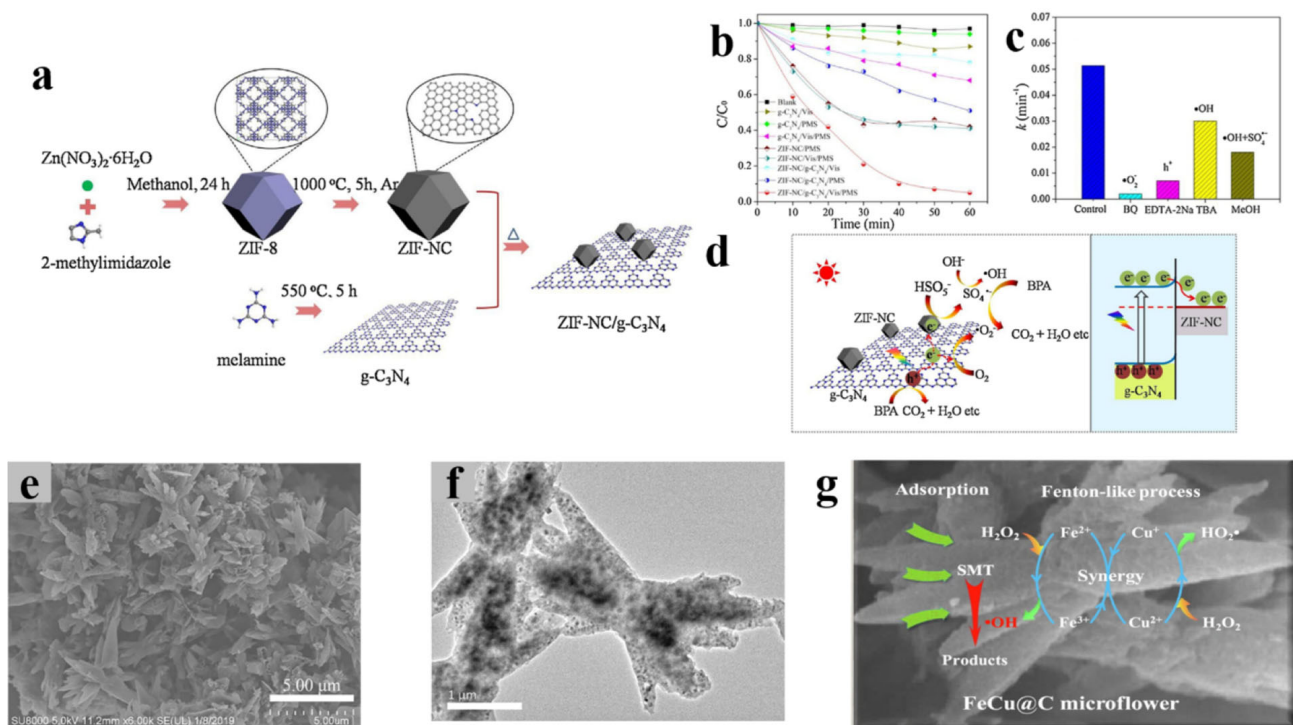


Figure 10. (a) Illustration of the preparation process for ZIF-NC/g-C₃N₄ composite. (b) The photocatalytic activity of different samples on BPA under visible light irradiation. (c) The corresponding reaction constants of ZIF-NC/g-C₃N₄ with PMS active material capture experiment. (d) Schematic illustration of photocatalytic mechanism of ZIF-NC/g-C₃N₄. Reprinted with permission from Ref. [171]. Copyright 2018, Elsevier. (e) FESEM images and (f) HRTEM images of FeCu@C. (g) Possible reaction mechanism of SMT degradation in the FeCu@C/H₂O₂ system. Reprinted with permission from Ref. [174]. Copyright 2019, Elsevier.

Given their rich carbon content and high porosity, MOFs are considered as ideal precursors for preparing carbon matrix and further producing new metal–carbon hybrid materials through pyrolysis. The introduction of carbon can significantly improve the dispersion and stability of catalytic metals and enhance the electronic conductivity of the material [178–180]. For instance, Tang et al. [174] synthesized a bimetallic carbon hybrid material (FeCu@C) by pyrolyzing the bimetallic MOF precursor [Fe, Cu]-BDC. The FeCu@C presented a 3D hierarchical microflower architecture (Figure 10e) within which some spherical dark spots were observed (Figure 10f), which might be the Fe and Cu NPs. The FeCu@C catalyst showed excellent catalytic activity for sulfamethizole (SMT) removal in the H₂O₂ system (removal within 90 min). The SMT removal process could be divided into the adsorption and Fenton-like process. On the one hand, the porous flower-like structure of the FeCu@C facilitated the rapid diffusion of SMT into the carbon matrix. On the other hand, the possible synergy between the internal bimetallic NPs helped to generate ·OH to promote the degradation of SMT.

Moreover, much effort also has been made to overcome the defects of particle aggregation and leaching of catalytic metal ions. For example, Zhang et al. [170] successfully synthesized yolk-shell MOF derivative Co₃O₄/C@SiO₂ nanoreactors (YSCCs) with carbon-supported Co₃O₄ as the core and SiO₂ as the protective shell (Figure 11a). The prepared ZIF-67@SiO₂, Co₃O₄@SiO₂ nanoreactors (YSCSs), and YSCCs all retained the rhombic dodecahedron structure of ZIF-67, and the Co₃O₄/C core of YSCCs was slightly smaller than the Co₃O₄ core of YSCSs (Figure 11b–d). In the TEM structures of YSCCs, the 10–20 nm Co₃O₄ NPs were dispersed in the MOF-derived carbon, and the core was tightly wrapped with an approx. 10 nm SiO₂ shell (Figure 11e). The catalyst YSCCs could remove 99.1% of BPA within 23 min, which was much higher than with Co₃O₄ (75%) and Co₃O₄/C (80%)

under the same conditions (Figure 11f). Free radical capture and quenching experiments (Figure 11g,h) implied that both $\cdot\text{OH}$ and $\text{SO}_4^{\bullet-}$ were the active species, and the $\text{SO}_4^{\bullet-}$ played a leading role in the PMS system. Because of the protection from the SiO_2 shell, Co leaching of the YSCCSs-PMS system was maintained at a low level (0.066–0.093 mg/L) (Figure 11i). Possible mechanisms of the BPA degradation process were briefly analyzed as follows (Figure 11j): (1) BPA and PMS could diffuse into the shell cavity; meanwhile, the Co^{3+} in the Co_3O_4 reacted with HSO_5^- to generate a large number of $\text{SO}_4^{\bullet-}$ for oxidative degradation of BPA; (2) hydrophilic SiO_2 prevented the leaching of Co ions and greatly retained the catalytic activity of Co by coating the active center Co_3O_4 ; (3) the presence of graphitic carbon also accelerated the transfer of electrons from the catalyst to the PMS.

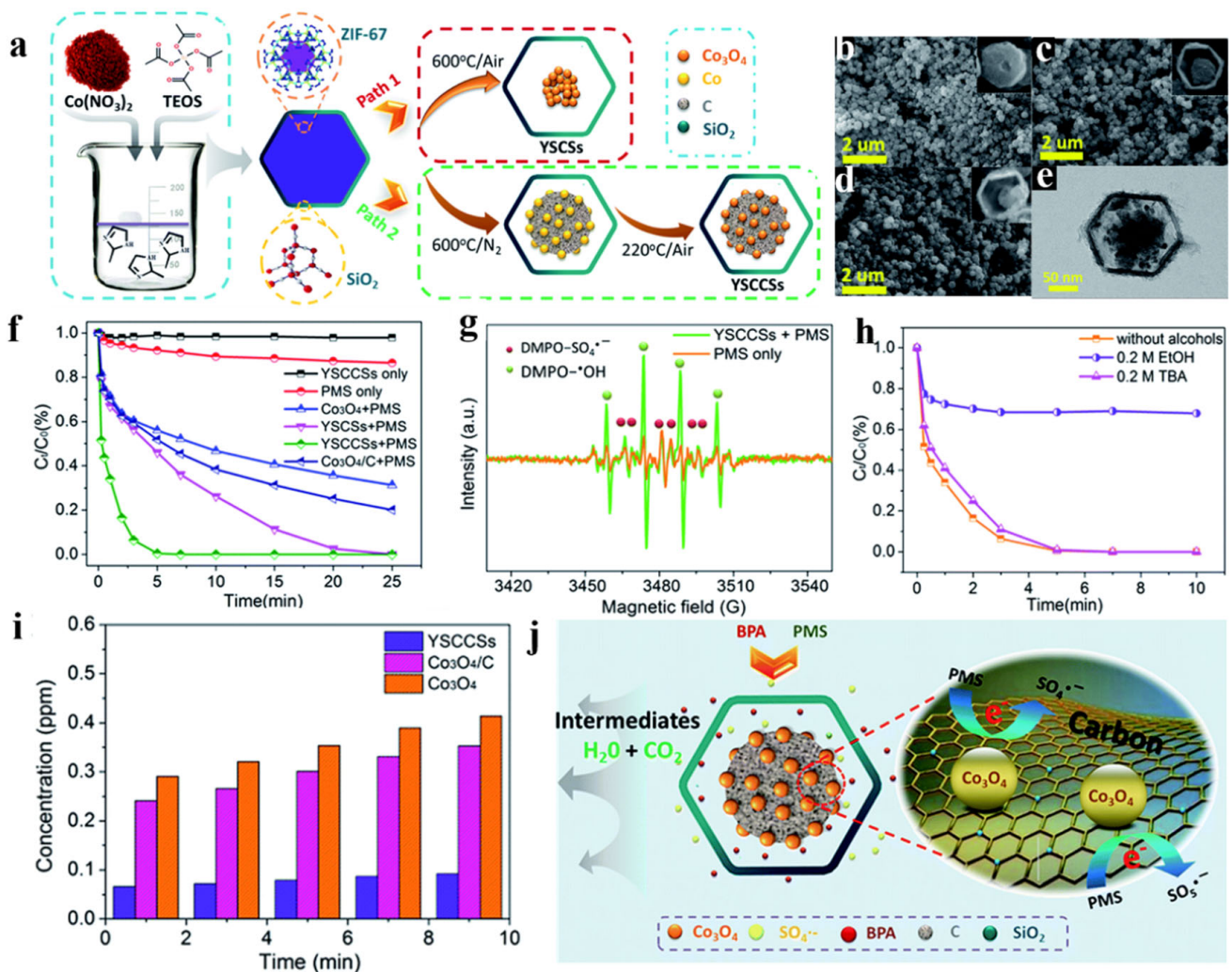


Figure 11. (a) Scheme diagram of synthesis of ZIF-67@ SiO_2 , YSCCSs and YSCCSs. SEM images of (b) ZIF-67@ SiO_2 , (c) YSCCSs and (d) YSCCSs. (e) TEM image of YSCCSs. (f) BPA degradation efficiency in different reaction systems within 25 min (conditions: [BPA] = 20 mg/L, [PMS] = 0.1 g/L, [catalyst] = 0.1 g/L and T = 298 K). (g) EPR spectra for the process of BPA degradation in different systems; (h) effects of radical scavengers on BPA degradation (conditions: [BPA] = 20 mg/L, [PMS] = 0.1 g/L, [catalyst] = 0.1 g/L, [DMPO] = 0.1 M, pH = 5, and T = 298 K). (i) The leaching of cobalt ions in the degradation process (conditions: [BPA] = 20 mg/L, [PMS] = 0.1 g/L, [catalyst] = 0.1 g/L, pH = 9.0, and T = 298 K). (j) Brief illustration of the possible synergistic mechanisms of BPA degradation. Reprinted with permission from Ref. [170]. Copyright 2018, The Royal Society of Chemistry.

4.5. Possible Mechanisms of OP Removal

As an excellent adsorbent, MOF-based materials for OP adsorption largely depend on the porosity and specific surface area of the materials. In short, the adsorption process of MOF-based materials for OPs involves multiple adsorption mechanisms, including physical adsorption (van der Waals interaction, electrostatic interaction) and chemical adsorption (acid–base interaction, hydrogen bonding interaction, π – π interaction, and some other chemical interactions) [181,182]. In addition to adsorption, catalysis (i.e., Fenton-like catalysis, photocatalytic, PMS/PS activation) is also another main application of MOF-based materials to remove OPs. Generally, catalysis and adsorption tend to be simultaneous and inseparable. During the catalysis process, OPs and oxidants (i.e., H_2O_2 , O_3 , PMS/PS) first pass through the ordered porous structure of MOF-based materials, combine with the active sites of the materials, and then undergo a series of catalytic degradation reactions.

The mechanisms of different types of catalytic degradation reactions are slightly different, which can be shown as follows. In the Fenton-like catalytic process, MOF-based materials mainly use the valence change of the central transition metal ion to activate H_2O_2 or O_3 to generate $\cdot\text{OH}$, and maintain the catalytic performance of the material through the redox cycle process [183]. As for the photocatalytic process, MOFs can be used as semiconductor precursors or combined with traditional semiconductor materials. With ultra-high porosity and unique channels, MOF-based materials can enhance the light trapping ability and promote the transfer of carriers, thereby effectively limiting the recombination of photogenerated electron-hole pairs. The active species in the photocatalytic process are mainly $\cdot\text{O}_2^-$ and $\cdot\text{OH}$ generated by photogenerated electrons, as well as strong oxidation holes [184]. In the PMS/PS activation system, the reaction mechanism can be roughly divided into the radical mechanism ($\text{SO}_4^{\bullet-}$, $\cdot\text{OH}$, $\cdot\text{O}_2^-$) and non-radical mechanism ($^1\text{O}_2$, electron transfer). For metal@C and metal oxide@C, the transition metals of the catalyst as the active center can activate PMS/PS to generate a large amount of $\text{SO}_4^{\bullet-}$ and $\cdot\text{OH}$, which are used to degrade OPs. This kind of reaction is dominated by radical reactions, part of which is completely degraded into CO_2 and water, and part of which forms intermediate products. In addition, non-radical pathways are mainly found in NPC and heteroatom-doped carbon, especially NC. Graphite N doping in the carbon skeleton can effectively break the chemical inertness of the sp^2 hybrid carbon configuration and induce charge transfer from adjacent carbon atoms to graphitic nitrogen atoms, thereby generating a positively charged center [115]. The high degree of graphitization and rich nitrogen doping of carbon materials are the key factors to promote non-free pathways. At present, research on the non-free radical mechanism is still in the exploratory stage, and many specific pathways are still unclear.

5. Conclusions and Prospects

This article reviewed the latest research progress in the application of two types of MOF-based materials (namely MOF composites and MOF derivatives) as adsorbents or catalysts for remediation of toxic HMs and OPs in water. The MOF-based materials inherit the advantages of one or more of the combined originals and generate synergistic effects between the composite components (e.g., advanced mechanical properties, magnetism, and excellent electron transfer capability). The MOF composite materials and their derivatives display excellent physicochemical characteristics (adsorption capacity, catalytic capacity, high selectivity, and reusability) far superior to the pristine MOFs. Therefore, they significantly improve the diffusion, adsorption, and degradation of pollutants in water. However, many problems still exist and need to be solved before these materials are applied in the real environment:

1. Production cost

Preparation of MOF-based materials requires higher input of raw materials (metal ions and organic linkers), energy, equipment, and labor than traditional adsorbents such as biochar. From the perspective of social and economic benefits, the transformation of MOF-based materials from laboratory scale to commercialization is still a problem to be

overcome. For hybridization of MOFs, the auxiliary component with excellent performance and an affordable price can significantly reduce the production cost of MOFs. Additionally, the selection of organic linkers and solvents requires further optimization. It is important to select ligands with abundant active sites and solvents that are inexpensive and non-toxic.

2. Material stability

As an adsorbent or catalyst, good water stability is a crucial parameter to measure the performance of a material. Good water stability is the prerequisite to ensure a material's adsorption or catalytic performance and reusability. Most of the MOF-based materials reported in the research have outstanding performance in the range of pH 2 to 10. However, nanoscale MOFs are almost impossible to be easily separated from the mixture solution, with the exception of magnetic MOF-based materials, and there are still some reports skirting discussion of their recyclability. Generally speaking, the water stability of pristine MOFs is poor, but it could be much improved by hybridizing them with substances of good physicochemical stability and ensuring the strong combination degree of MOFs and the combined elements. Further, MOF derivatives have highly graphitized structures, which can guarantee high water stability. Ensuring the release of nano-metal particles or nano-metal oxides of the derivatives in small amounts during the reaction is a key factor for the water stability of MOF derivatives.

3. Material safety

Given their outstanding characteristics, the trend towards continuous technological improvement and cost reduction is expected to increase the number of applications and production volumes of MOF-based materials. It also implies that the MOF-based materials will be interacted with various environmental endpoints with unprecedented frequency and quantity; however, the risks they may pose are still unknown. At present, most of the MOF-based materials under research are still of nano-scale. Nanoparticles may undergo a variety of migrations and transformations (aggregation dissolution, redox reactions, reactions with aquatic organisms, etc.) in environmental and biological systems, which will affect the fate, transport, and toxicity of MOF-based materials [185]. Ruyra et al. [186] and Fan et al. [187] found that different MOFs would produce certain toxic and environmental effects on human cells and organisms in the environment. Therefore, it is of paramount importance to include life-cycle assessment in the manufacture and use of MOF-based materials. A life-cycle database should be constructed and made available for any end-users when applying such materials in environmental or health-related domains.

4. Material recyclability

Numerous research studies have indicated that MOF-based materials as adsorbents have excellent adsorption and regeneration properties for a wide variety of HMs and OPs. For MOFs used for the removal of HMs, the routine procedure was to use acid or alkali solutions for desorption. The process was carried out for four to five cycles, and most of the MOF composites were still able to achieve more than 80% HM adsorption performance. Similarly, their removal efficiency for conventional industrial OPs and pesticides decreased slightly after five cycles; their adsorption capacity for organic dyes had no obvious loss after five to six cycles, and the adsorption efficiency for PPCPs decreased slightly after four to seven cycles. To achieve greater recyclability for > 10 rounds of use, more attention should be paid to the development of methods and technologies for material regeneration because very few studies have so far addressed its significance.

5. Extension from water to other fields

Up to now, the MOF-based materials have been used mainly for remediating HMs and OPs in the water environment (especially wastewater). For that reason, there has not been any attempt to apply the materials in other environmental systems (such as groundwater, soils, sediments, etc.). Therefore, there is an extensive research space for investigating the feasibility of using such materials in other fields. Whether we can combine the MOF-based

materials with some existing treatment technologies for the remediation of HMs or OPs in other fields is worthy of further exploration.

In short, MOF-based materials are invented in compliance with demand and the development of technology, and they will continue to be developed when new challenges arise. MOF-based materials have provided us many new opportunities for the removal of HMs and OPs in water, but their potential is far away from reaching a limit. Future research should start with simplifying the synthesis process, reducing costs, and improving its environmental stability and commercial practicability, so that MOF-based materials can achieve large-scale environmental applicability. With the continuous efforts made to tackle the difficulties and challenges, MOF-based materials will inevitably continue to be developed in the future and help promote environmental sustainability.

Author Contributions: Conceptualization, C.Y. and Z.X.; writing—original draft preparation, C.Y. & Z.X.; writing—review and editing, J.W.; supervision, J.W.; funding acquisition, J.W. All authors have read and agreed to the published version of the manuscript.

Funding: This research was funded by the Natural Science Foundation of Chongqing (CSTB2022NSCQ-MSX0391), the Open Funding of the State Environmental Protection Key Laboratory of Monitoring for Heavy Metal Pollutants (SKLMHM202211), and the Natural Science Foundation of Changsha City (No. kq2208020).

Institutional Review Board Statement: Not applicable.

Informed Consent Statement: Not applicable.

Data Availability Statement: Not applicable.

Conflicts of Interest: The authors declare no conflict of interest.

Abbreviations

AO7: acid Orange 7; As: arsenic; ATNL: atenolol; AY: acid yellow-17; BC: bacterial cellulose; BDC: terephthalic acid; BN: boron nitride; BPA: bisphenol A; BPF: bisphenol F; BTC: trimesic acid; BZQ: p-benzoquinone; CAP: chloramphenicol; CB: conduction band; Cd: cadmium; CEP-C: cephalosporin C; CIP: ciprofloxacin; CLFA: clofibric acid; CMC: carboxymethylcellulose; CNTs: carbon nanotubes; CR: congo red; Cr: chromium; DF: diclofenac; DCF: diclofenac sodium; EPA: Environmental Protection Agency; FLV: Fluvastatin; GO: graphene oxide; Hg: mercury; HMs: heavy metals; IBP: ibuprofen; IC: indigo carmine; IPA: isopropanol; LPC: layered porous carbon; LOFX: levofloxacin; LVF: levofloxacin hydrochloride; MB: methylene blue; MG: malachite green; MIL: Materials of Institut Lavoisier; MO: methyl orange; MOFs: metal organic frameworks; Na₂-EDTA: ethylenediaminetetraacetate; NC: N-doped carbon; NRC: nitroresorcinol; MWCNT: multi-wall carbon nanotubes; NPC: nanoporous carbon; ·OH: hydroxyl radical; ·O₂⁻: superoxide radical; ¹O₂: singlet oxygen; OPs: organic pollutants; PAHs: polycyclic aromatic hydrocarbons; Pb: lead; PCBs: polychlorinated biphenyls; PCMX: para-chloro-meta-xylene; PMS: peroxymonosulfate; POPs: persistent organic pollutants; PPCPs: pharmaceuticals and personal care products; PSM: post-synthetic-modification; PSS: polystyrenesulfonate; rGO: reduced graphene oxide; RhB: rhodamine B; SEM: scanning electron microscope; SMT: sulfamethizole; SMX: sulfamethoxazole; SMZ: sulfamethazine; SO₄^{•-}: sulfate radical; TC tetracycline; TCs: tetracycline antibiotics; TCS: triclosan; TEM: transmission electron microscopy. THE: theophylline; TNTs: titanate nanotubes; UIO: University of Oslo; VB: valence band; VSM: vibrating sample magnetometry; XRD: X-ray powder diffraction; ZIF: Zeolitic imidazolate framework.

References

1. Dong, H.; Zhang, L.; Shao, P.H.; Hu, Z.C.; Yao, Z.W.; Xiao, Q.Y.; Li, D.W.; Li, M.; Yang, L.M.; Luo, S.L.; et al. A metal-organic framework surrounded with conjugate acid-base pairs for the efficient capture of Cr(VI) via hydrogen bonding over a wide pH range. *J. Hazard. Mater.* **2023**, *441*, 129945. [[CrossRef](#)] [[PubMed](#)]
2. Shams, M.; Dehghani, M.H.; Nabizadeh, R.; Mesdaghinia, A.; Alimohammadi, M.; Najafpoor, A.A. Adsorption of phosphorus from aqueous solution by cubic zeolitic imidazolate framework-8: Modeling, mechanical agitation versus sonication. *J. Mol. Liq.* **2016**, *224*, 151–157. [[CrossRef](#)]

3. Lu, F.; Astruc, D. Nanocatalysts and other nanomaterials for water remediation from organic pollutants. *Coord. Chem. Rev.* **2020**, *408*, 213180. [[CrossRef](#)]
4. USEPA. *Drinking Water Standards and Health Advisories (EPA 820-R-11-002)*; Office of Water, USEPA: Washington, DC, USA, 2011.
5. Fu, K.X.; Liu, X.C.; Lv, Y.; Luo, J.M.; Sun, M.X.; Luo, S.L.; Crittenden, J.C. Superselective Hg(II) Removal from Water Using a Thiol-Laced MOF-Based Sponge Monolith: Performance and Mechanism. *Environ. Sci. Technol.* **2022**, *56*, 2677–2688. [[CrossRef](#)]
6. Wen, J.; Hu, X.H. Metal selectivity and effects of co-existing ions on the removal of Cd, Cu, Ni, and Cr by ZIF-8-EGCG nanoparticles. *J. Colloid. Interf. Sci.* **2021**, *589*, 578–586. [[CrossRef](#)]
7. Ma, S.; Hou, Y.; Xiao, Y.; Chu, F.; Cai, T.; Hu, W.; Hu, Y. Metal-organic framework@polyaniline nanoarchitecture for improved fire safety and mechanical performance of epoxy resin. *Mater. Chem. Phys.* **2020**, *247*, 122875. [[CrossRef](#)]
8. Seetharaj, R.; Vandana, P.V.; Arya, P.; Mathew, S. Dependence of solvents, pH, molar ratio and temperature in tuning metal organic framework architecture. *Arab. J. Chem.* **2019**, *12*, 295–315. [[CrossRef](#)]
9. Cheng, P.; Wang, C.; Kaneti, Y.V.; Eguchi, M.; Lin, J.; Yamauchi, Y.; Na, J. Practical MOF Nanoarchitectonics: New Strategies for Enhancing the Processability of MOFs for Practical Applications. *Langmuir* **2020**, *36*, 4231–4249. [[CrossRef](#)]
10. Wen, J.; Fang, Y.; Zeng, G.M. Progress and prospect of adsorptive removal of heavy metal ions from aqueous solution using metal-organic frameworks: A review of studies from the last decade. *Chemosphere* **2018**, *201*, 627–643. [[CrossRef](#)]
11. Yaghi, O.M.; Li, G.M.; Li, H.L. Selective binding and removal of guests in a microporous metal-organic framework. *Nature* **1995**, *378*, 703–706. [[CrossRef](#)]
12. Trens, P.; Belarbi, H.; Shepherd, C.; Gonzalez, P.; Ramsahye, N.A.; Lee, U.H.; Seo, Y.K.; Chang, J.S. Adsorption and separation of xylene isomers vapors onto the chromium terephthalate-based porous material MIL-101(Cr): An experimental and computational study. *Micropor. Mesopor. Mater.* **2014**, *183*, 17–22. [[CrossRef](#)]
13. Massoudinejad, M.; Ghaderpoori, M.; Shahsavani, A.; Amini, M.M. Adsorption of fluoride over a metal organic framework Uio-66 functionalized with amine groups and optimization with response surface methodology. *J. Mol. Liq.* **2016**, *221*, 279–286. [[CrossRef](#)]
14. Kayal, S.; Sun, B.; Chakraborty, A. Study of metal-organic framework MIL-101(Cr) for natural gas (methane) storage and compare with other MOFs (metal-organic frameworks). *Energy* **2015**, *91*, 772–781. [[CrossRef](#)]
15. Lysova, A.A.; Samsonenko, D.G.; Kovalenko, K.A.; Nizovtsev, A.S.; Dybtsev, D.N.; Fedin, V.P. A Series of Mesoporous Metal-Organic Frameworks with Tunable Windows Sizes and Exceptionally High Ethane over Ethylene Adsorption Selectivity. *Angew. Chem. Int. Edit.* **2020**, *59*, 20561–20567. [[CrossRef](#)] [[PubMed](#)]
16. Duan, J.; Pan, Y.; Liu, G.; Jin, W. Metal-organic framework adsorbents and membranes for separation applications. *Curr. Opin. Chem. Eng.* **2018**, *20*, 122–131. [[CrossRef](#)]
17. Sun, Y.; Dong, B.X.; Liu, W.L. An adjustable dual-emission fluorescent metal-organic framework: Effective detection of multiple metal ions, nitro-based molecules and DMA. *Spectrochim. Acta A Mol. Biomol. Spectrosc.* **2019**, *223*, 117283. [[CrossRef](#)]
18. Huxford, R.C.; Della Rocca, J.; Lin, W. Metal-organic frameworks as potential drug carriers. *Curr. Opin. Chem. Biol.* **2010**, *14*, 262–268. [[CrossRef](#)]
19. Polyukhov, D.M.; Kudriavych, N.A.; Gromilov, S.A.; Kiryutin, A.S.; Poryvaev, A.S.; Fedin, M.V. Efficient MOF-Catalyzed Ortho-Para Hydrogen Conversion for Practical Liquefaction and Energy Storage. *ACS Energy Lett.* **2022**, *7*, 4336–4341. [[CrossRef](#)]
20. Zhong, F.; Li, C.; Xie, Y.; Xu, H.; Gao, J. Titanium metal-organic framework nanorods for highly sensitive nitroaromatic explosives detection and nanomolar sensing of Fe³⁺. *J. Solid State Chem.* **2019**, *278*, 120892. [[CrossRef](#)]
21. Lysova, A.A.; Samsonenko, D.G.; Dorovatovskii, P.V.; Lazavenko, V.A.; Khrustalev, V.N.; Kovalenko, K.A.; Dybtsev, D.N.; Fedin, V.P. Tuning the Molecular and Cationic Affinity in a Series of Multifunctional Metal–Organic Frameworks Based on Dodecanuclear Zn(II) Carboxylate Wheels. *J. Am. Chem. Soc.* **2019**, *141*, 17260–17269. [[CrossRef](#)]
22. Qiu, J.; Zhang, X.; Feng, Y.; Zhang, X.; Wang, H.; Yao, J. Modified metal-organic frameworks as photocatalysts. *Appl. Catal. B* **2018**, *231*, 317–342. [[CrossRef](#)]
23. Wang, C.; Kim, J.; Malgras, V.; Na, J.; Lin, J.; You, J.; Zhang, M.; Li, J.; Yamauchi, Y. Metal-Organic Frameworks and Their Derived Materials: Emerging Catalysts for a Sulfate Radicals-Based Advanced Oxidation Process in Water Purification. *Small* **2019**, *15*, e1900744. [[CrossRef](#)] [[PubMed](#)]
24. Li, J.; Wang, X.; Zhao, G.; Chen, C.; Chai, Z.; Alsaedi, A.; Hayat, T.; Wang, X. Metal-organic framework-based materials: Superior adsorbents for the capture of toxic and radioactive metal ions. *Chem. Soc. Rev.* **2018**, *47*, 2322–2356. [[CrossRef](#)]
25. Megha, R.; Lakhani, V.; Vala, S.; Dharaskar, S.; Reddy Paluvai, N.; Kumar Sinha, M.; Sasikumar Jampa, S. Removal of heavy metals and dyes from its aqueous solution utilizing metal organic Frameworks (MOFs): Review. *Mater. Today Proc.* **2023**, *77*, 188–200.
26. Visa, A.; Maranescu, B.; Lupa, L.; Crisan, L.; Borota, A. New Efficient Adsorbent Materials for the Removal of Cd(II) from Aqueous Solutions. *Nanomaterials* **2020**, *10*, 899. [[CrossRef](#)] [[PubMed](#)]
27. Tran, T.V.; Nguyen, D.T.C.; Le, H.T.N.; Tu, T.T.K.; Le, N.D.; Lim, K.T.; Bach, L.G.; Nguyen, T.D. MIL-53 (Fe)-directed synthesis of hierarchically mesoporous carbon and its utilization for ciprofloxacin antibiotic remediation. *J. Environ. Chem. Eng.* **2019**, *7*, 102881. [[CrossRef](#)]
28. Xiong, W.; Zeng, Z.; Zeng, G.; Yang, Z.H.; Xiao, R.; Li, X.; Cao, J.; Zhou, C.; Chen, H.; Jia, M.; et al. Metal-organic frameworks derived magnetic carbon- α Fe/Fe₃C composites as a highly effective adsorbent for tetracycline removal from aqueous solution. *Chem. Eng. J.* **2019**, *374*, 91–99. [[CrossRef](#)]

29. Liu, T.; Zhang, Z.; Wang, Z.; Wang, Z.L.; Bush, R. Highly efficient and rapid removal of arsenic(III) from aqueous solutions by nanoscale zero-valent iron supported on a zirconium 1,4-dicarboxybenzene metal-organic framework (UiO-66 MOF). *RSC Adv.* **2019**, *9*, 39475–39487. [[CrossRef](#)]
30. Mao, J.; Ge, M.; Huang, J.; Lai, Y.; Lin, C.; Zhang, K.; Meng, K.; Tang, Y. Constructing multifunctional MOF@rGO hydro-/aerogels by the self-assembly process for customized water remediation. *J. Mater. Chem. A* **2017**, *5*, 11873–11881. [[CrossRef](#)]
31. Abdollahi, N.; Akbar Razavi, S.A.; Morsali, A.; Hu, M.L. High capacity Hg(II) and Pb(II) removal using MOF-based nanocomposite: Cooperative effects of pore functionalization and surface-charge modulation. *J. Hazard. Mater.* **2020**, *387*, 121667. [[CrossRef](#)]
32. Boix, G.; Troyano, J.; Garzon-Tovar, L.; Camur, C.; Bermejo, N.; Yazdi, A.; Piella, J.; Bastus, N.G.; Puentes, V.F.; Imaz, I.; et al. MOF-Beads Containing Inorganic Nanoparticles for the Simultaneous Removal of Multiple Heavy Metals from Water. *ACS Appl. Mater. Interfaces* **2020**, *12*, 10554–10562. [[CrossRef](#)] [[PubMed](#)]
33. Rao, Z.; Feng, K.; Tang, B.; Wu, P. Surface Decoration of Amino-Functionalized Metal–Organic Framework/Graphene Oxide Composite onto Polydopamine-Coated Membrane Substrate for Highly Efficient Heavy Metal Removal. *ACS Appl. Mater. Interfaces* **2017**, *9*, 2594–2605. [[CrossRef](#)] [[PubMed](#)]
34. Wei, N.; Zheng, X.; Ou, H.; Yu, P.; Li, Q.; Feng, S. Fabrication of an amine-modified ZIF-8@GO membrane for high-efficiency adsorption of copper ions. *New J. Chem.* **2019**, *43*, 5603–5610. [[CrossRef](#)]
35. Zhang, P.; Gong, J.L.; Zeng, G.M.; Song, B.; Liu, H.Y.; Huan, S.Y.; Li, J. Ultrathin reduced graphene oxide/MOF nanofiltration membrane with improved purification performance at low pressure. *Chemosphere* **2018**, *204*, 378–389. [[CrossRef](#)]
36. Efome, J.E.; Rana, D.; Matsuura, T.; Lan, C.Q. Insight Studies on Metal–Organic Framework Nanofibrous Membrane Adsorption and Activation for Heavy Metal Ions Removal from Aqueous Solution. *ACS Appl. Mater. Interfaces* **2018**, *10*, 18619–18629. [[CrossRef](#)]
37. Jamshidifard, S.; Koushkbaghi, S.; Hosseini, S.; Rezaei, S.; Karamipour, A.; Jafari Rad, A.; Irani, M. Incorporation of UiO-66-NH₂ MOF into the PAN/chitosan nanofibers for adsorption and membrane filtration of Pb(II), Cd(II) and Cr(VI) ions from aqueous solutions. *J. Hazard. Mater.* **2019**, *368*, 10–20. [[CrossRef](#)]
38. Pi, Y.; Li, X.; Xia, Q.; Wu, J.; Li, Z.; Li, Y.; Xiao, J. Formation of willow leaf-like structures composed of NH₂-MIL68(In) on a multifunctional multiwalled carbon nanotube backbone for enhanced photocatalytic reduction of Cr(VI). *Nano Res.* **2017**, *10*, 3543–3556. [[CrossRef](#)]
39. Song, Y.; Wang, N.; Yang, L.Y.; Wang, Y.G.; Yu, D.; Ouyang, X.K. Facile Fabrication of ZIF-8/Calcium Alginate Microparticles for Highly Efficient Adsorption of Pb(II) from Aqueous Solutions. *Ind. Eng. Chem. Res.* **2019**, *58*, 6394–6401. [[CrossRef](#)]
40. Bo, S.; Ren, W.; Lei, C.; Xie, Y.; Cai, Y.; Wang, S.; Gao, J.; Ni, Q.; Yao, J. Flexible and porous cellulose aerogels/zeolitic imidazolate framework (ZIF-8) hybrids for adsorption removal of Cr(IV) from water. *J. Solid State Chem.* **2018**, *262*, 135–141. [[CrossRef](#)]
41. Yin, N.; Wang, K.; Xia, Y.A.; Li, Z. Novel melamine modified metal-organic frameworks for remarkably high removal of heavy metal Pb(II). *Desalination* **2018**, *430*, 120–127. [[CrossRef](#)]
42. Zhang, L.; Wang, J.; Ren, X.; Zhang, W.; Zhang, T.; Liu, X.; Du, T.; Li, T.; Wang, J. Internally extended growth of core-shell NH₂-MIL-101(Al)@ZIF-8 nanoflowers for the simultaneous detection and removal of Cu(II). *J. Mater. Chem. A* **2018**, *6*, 21029–21038. [[CrossRef](#)]
43. Li, L.; Xu, Y.; Zhong, D.; Zhong, N. CTAB-surface-functionalized magnetic MOF@MOF composite adsorbent for Cr(VI) efficient removal from aqueous solution. *Colloids Surf. A* **2020**, *586*, 124255. [[CrossRef](#)]
44. Jian, M.; Wang, H.; Liu, R.; Qu, J.; Wang, H.; Zhang, X. Self-assembled one-dimensional MnO₂@zeolitic imidazolate framework-8 nanostructures for highly efficient arsenite removal. *Environ. Sci. Nano* **2016**, *3*, 1186–1194. [[CrossRef](#)]
45. Rapti, S.; Pournara, A.; Sarma, D.; Papadas, I.T.; Armatas, G.S.; Tsipis, A.C.; Lazarides, T.; Kanatzidis, M.G.; Manos, M.J. Selective capture of hexavalent chromium from an anion-exchange column of metal organic resin-alginic acid composite. *Chem. Sci.* **2016**, *7*, 2427–2436. [[CrossRef](#)] [[PubMed](#)]
46. Zhu, K.; Chen, C.; Xu, H.; Gao, Y.; Tan, X.; Alsaedi, A.; Hayat, T. Cr(VI) Reduction and Immobilization by Core-Double-Shell Structured Magnetic Polydopamine@Zeolitic Imidazolate Frameworks-8 Microspheres. *ACS Sustain. Chem. Eng.* **2017**, *5*, 6795–6802. [[CrossRef](#)]
47. Sun, D.T.; Peng, L.; Reeder, W.S.; Moosavi, S.M.; Tiana, D.; Britt, D.K.; Oveisi, E.; Queen, W.L. Rapid, Selective Heavy Metal Removal from Water by a Metal–Organic Framework/Polydopamine Composite. *ACS Cent. Sci.* **2018**, *4*, 349–356. [[CrossRef](#)]
48. Wang, N.; Ouyang, X.K.; Yang, L.Y.; Omer, A.M. Fabrication of a Magnetic Cellulose Nanocrystal/Metal–Organic Framework Composite for Removal of Pb(II) from Water. *ACS Sustain. Chem. Eng.* **2017**, *5*, 10447–10458. [[CrossRef](#)]
49. Ricco, R.; Konstas, K.; Styles, M.J.; Richardson, J.J.; Babarao, R.; Suzuki, K.; Scopece, P.; Falcaro, P. Lead(II) uptake by aluminium based magnetic framework composites (MFCs) in water. *J. Mater. Chem. A* **2015**, *3*, 19822–19831. [[CrossRef](#)]
50. Wang, X.; Liu, J.; Leong, S.; Lin, X.; Wei, J.; Kong, B.; Xu, Y.; Low, Z.X.; Yao, J.; Wang, H. Rapid Construction of ZnO@ZIF-8 Heterostructures with Size-Selective Photocatalysis Properties. *ACS Appl. Mater. Interfaces* **2016**, *8*, 9080–9087. [[CrossRef](#)]
51. Ma, X.; Lou, Y.; Chen, X.-B.; Shi, Z.; Xu, Y. Multifunctional flexible composite aerogels constructed through in-situ growth of metal-organic framework nanoparticles on bacterial cellulose. *Chem. Eng. J.* **2019**, *356*, 227–235. [[CrossRef](#)]
52. Lei, C.; Gao, J.; Ren, W.; Xie, Y.; Abdalkarim, S.Y.H.; Wang, S.; Ni, Q.; Yao, J. Fabrication of metal-organic frameworks@cellulose aerogels composite materials for removal of heavy metal ions in water. *Carbohydr. Polym.* **2019**, *205*, 35–41. [[CrossRef](#)] [[PubMed](#)]

53. Li, D.; Tian, X.; Wang, Z.; Guan, Z.; Li, X.; Qiao, H.; Ke, H.; Luo, L.; Wei, Q. Multifunctional adsorbent based on metal-organic framework modified bacterial cellulose/chitosan composite aerogel for high efficient removal of heavy metal ion and organic pollutant. *Chem. Eng. J.* **2020**, *383*, 123127. [[CrossRef](#)]
54. Shooto, N.D.; Dikio, C.W.; Wankasi, D.; Sikhwivhilu, L.M.; Mtunzi, F.M.; Dikio, E.D. Novel PVA/MOF Nanofibres: Fabrication, Evaluation and Adsorption of Lead Ions from Aqueous Solution. *Nanoscale Res. Lett.* **2016**, *11*, 414. [[CrossRef](#)]
55. Efome, J.E.; Rana, D.; Matsuura, T.; Lan, C.Q. Metal-organic frameworks supported on nanofibers to remove heavy metals. *J. Mater. Chem. A* **2018**, *6*, 4550–4555. [[CrossRef](#)]
56. Bahmani, E.; Koushkbaghi, S.; Darabi, M.; ZabihiSahebi, A.; Askari, A.; Irani, M. Fabrication of novel chitosan-g-PNVCL/ZIF-8 composite nanofibers for adsorption of Cr(VI), As(V) and phenol in a single and ternary systems. *Carbohydr. Polym.* **2019**, *224*, 115148. [[CrossRef](#)] [[PubMed](#)]
57. He, M.; Wang, L.; Lv, Y.; Wang, X.; Zhu, J.; Zhang, Y.; Liu, T. Novel polydopamine/metal organic framework thin film nanocomposite forward osmosis membrane for salt rejection and heavy metal removal. *Chem. Eng. J.* **2020**, *389*, 124452. [[CrossRef](#)]
58. Li, T.; Zhang, W.; Zhai, S.; Gao, G.; Ding, J.; Zhang, W.; Liu, Y.; Zhao, X.; Pan, B.; Lv, L. Efficient removal of nickel(II) from high salinity wastewater by a novel PAA/ZIF-8/PVDF hybrid ultrafiltration membrane. *Water Res.* **2018**, *143*, 87–98. [[CrossRef](#)]
59. Liang, R.; Shen, L.; Jing, F.; Qin, N.; Wu, L. Preparation of MIL-53(Fe)-Reduced Graphene Oxide Nanocomposites by a Simple Self-Assembly Strategy for Increasing Interfacial Contact: Efficient Visible-Light Photocatalysts. *ACS Appl. Mater. Interf.* **2015**, *7*, 9507–9515. [[CrossRef](#)]
60. Tang, J.; Yamauchi, Y. Carbon materials: MOF morphologies in control. *Nat. Chem.* **2016**, *8*, 638–639. [[CrossRef](#)]
61. Hu, M.; Reboul, J.; Furukawa, S.; Torad, N.L.; Ji, Q.; Srinivasu, P.; Ariga, K.; Kitagawa, S.; Yamauchi, Y. Direct carbonization of Al-based porous coordination polymer for synthesis of nanoporous carbon. *J. Am. Chem. Soc.* **2012**, *134*, 2864–2867. [[CrossRef](#)]
62. Li, X.; Liu, Y.; Zhang, C.; Wen, T.; Zhuang, L.; Wang, X.; Song, G.; Chen, D.; Ai, Y.; Hayat, T.; et al. Porous Fe₂O₃ microcubes derived from metal organic frameworks for efficient elimination of organic pollutants and heavy metal ions. *Chem. Eng. J.* **2018**, *336*, 241–252. [[CrossRef](#)]
63. Lai, Y.; Wang, F.; Zhang, Y.; Ou, P.; Wu, P.; Fang, Q.; Chen, Z.; Li, S. UiO-66 derived N-doped carbon nanoparticles coated by PANI for simultaneous adsorption and reduction of hexavalent chromium from waste water. *Chem. Eng. J.* **2019**, *378*, 122069. [[CrossRef](#)]
64. Yadav, M.; Xu, Q. Catalytic chromium reduction using formic acid and metal nanoparticles immobilized in a metal-organic framework. *Chem. Commun.* **2013**, *49*, 3327–3329. [[CrossRef](#)] [[PubMed](#)]
65. Gadipelli, S.; Travis, W.; Zhou, W.; Guo, Z. A thermally derived and optimized structure from ZIF-8 with giant enhancement in CO₂ uptake. *Energy Environ. Sci.* **2014**, *7*, 2232–2238. [[CrossRef](#)]
66. Chen, D.; Shen, W.; Wu, S.; Chen, C.; Luo, X.; Guo, L. Ion exchange induced removal of Pb(II) by MOF-derived magnetic inorganic sorbents. *Nanoscale* **2016**, *8*, 7172–7179. [[CrossRef](#)]
67. Chakraborty, A.; Bhattacharyya, S.; Hazra, A.; Ghosh, A.C.; Maji, T.K. Post-synthetic metalation in an anionic MOF for efficient catalytic activity and removal of heavy metal ions from aqueous solution. *Chem Commun.* **2016**, *52*, 2831–2834. [[CrossRef](#)]
68. Zhang, J.; Xiong, Z.; Li, C.; Wu, C. Exploring a thiol-functionalized MOF for elimination of lead and cadmium from aqueous solution. *J. Mol. Liq.* **2016**, *221*, 43–50. [[CrossRef](#)]
69. Ke, F.; Jiang, J.; Li, Y.; Liang, J.; Wan, X.; Ko, S. Highly selective removal of Hg²⁺ and Pb²⁺ by thiol-functionalized Fe₃O₄@metal-organic framework core-shell magnetic microspheres. *Appl. Surf. Sci.* **2017**, *413*, 266–274. [[CrossRef](#)]
70. Venkateswarlu, S.; Panda, A.; Kim, E.; Yoon, M. Biopolymer-Coated Magnetite Nanoparticles and Metal-Organic Framework Ternary Composites for Cooperative Pb(II) Adsorption. *ACS Appl. Nano Mater.* **2018**, *1*, 4198–4210. [[CrossRef](#)]
71. Huang, L.; He, M.; Chen, B.; Hu, B. Magnetic Zr-MOFs nanocomposites for rapid removal of heavy metal ions and dyes from water. *Chemosphere* **2018**, *199*, 435–444. [[CrossRef](#)]
72. Song, Y.; Qiang, T.; Ye, M.; Ma, Q.; Fang, Z. Metal organic framework derived magnetically separable 3-dimensional hierarchical Ni@C nanocomposites: Synthesis and adsorption properties. *Appl. Surf. Sci.* **2015**, *359*, 834–840. [[CrossRef](#)]
73. Afshariazar, F.; Morsali, A.; Wang, J.; Junk, P.C. Highest and Fastest Removal Rate of Pb(II) Ions through Rational Functionalized Decoration of a Metal-Organic Framework Cavity. *Chemistry* **2020**, *26*, 1355–1362. [[CrossRef](#)] [[PubMed](#)]
74. Huo, J.B.; Xu, L.; Yang, J.C.E.; Cui, H.J.; Yuan, B.; Fu, M.L. Magnetic responsive Fe₃O₄-ZIF-8 core-shell composites for efficient removal of As(III) from water. *Colloids Surf. A* **2018**, *539*, 59–68. [[CrossRef](#)]
75. Huo, J.-B.; Xu, L.; Chen, X.; Zhang, Y.; Yang, J.-C.E.; Yuan, B.; Fu, M.-L. Direct epitaxial synthesis of magnetic Fe₃O₄@UiO-66 composite for efficient removal of arsenate from water. *Micropor. Mesopor. Mater.* **2019**, *276*, 68–75. [[CrossRef](#)]
76. Folens, K.; Leus, K.; Nicomel, N.R.; Meledina, M.; Turner, S.; Van Tendeloo, G.; Laing, G.D.; Van Der Voort, P. Fe₃O₄@MIL-101—A Selective and Regenerable Adsorbent for the Removal of As Species from Water. *Eur. J. Inorg. Chem.* **2016**, *27*, 4395–4401. [[CrossRef](#)]
77. Yang, J.C.; Yin, X.B. CoFe₂O₄@MIL-100(Fe) hybrid magnetic nanoparticles exhibit fast and selective adsorption of arsenic with high adsorption capacity. *Sci. Rep.* **2017**, *7*, 40955. [[CrossRef](#)]
78. Wang, D.; Gilliland, S.E.; Yi, X.; Logan, K.; Heitger, D.R.; Lucas, H.R.; Wang, W.N. Iron Mesh-Based Metal Organic Framework Filter for Efficient Arsenic Removal. *Environ. Sci. Technol.* **2018**, *52*, 4275–4284. [[CrossRef](#)]
79. Lv, Z.; Fan, Q.; Xie, Y.; Chen, Z.; Alsaedi, A.; Hayat, T.; Wang, X.; Chen, C. MOFs-derived magnetic chestnut shell-like hollow sphere NiO/Ni@C composites and their removal performance for arsenic(V). *Chem. Eng. J.* **2019**, *362*, 413–421. [[CrossRef](#)]

80. Wang, X.; Liu, W.; Fu, H.; Yi, X.H.; Wang, P.; Zhao, C.; Wang, C.C.; Zheng, W. Simultaneous Cr(VI) reduction and Cr(III) removal of bifunctional MOF/Titanate nanotube composites. *Environ. Pollut.* **2019**, *249*, 502–511. [CrossRef]
81. Liang, R.; Jing, F.; Shen, L.; Qin, N.; Wu, L. M@MIL-100(Fe) (M = Au, Pd, Pt) nanocomposites fabricated by a facile photodeposition process: Efficient visible-light photocatalysts for redox reactions in water. *Nano Res.* **2015**, *8*, 3237–3249. [CrossRef]
82. Zhu, K.; Chen, C.; Lu, S.; Zhang, X.; Alsaedi, A.; Hayat, T. MOFs-induced encapsulation of ultrafine Ni nanoparticles into 3D N-doped graphene-CNT frameworks as a recyclable catalyst for Cr(VI) reduction with formic acid. *Carbon* **2019**, *148*, 52–63. [CrossRef]
83. Gao, G.; Nie, L.; Yang, S.; Jin, P.; Chen, R.; Ding, D.; Wang, X.C.; Wang, W.; Wu, K.; Zhang, Q. Well-defined strategy for development of adsorbent using metal organic frameworks (MOF) template for high performance removal of hexavalent chromium. *Appl. Surf. Sci.* **2018**, *457*, 1208–1217. [CrossRef]
84. Fang, Y.; Wen, J.; Zhang, H.; Zhang, Q.; Hu, X. Enhancing Cr(VI) reduction and immobilization by magnetic core-shell structured NZVI@MOF derivative hybrids. *Environ. Pollut.* **2020**, *260*, 114021. [CrossRef]
85. Liu, Z.M.; Wu, S.H.; Jia, S.Y.; Qin, F.-X.; Zhou, S.M.; Ren, H.T.; Na, P.; Liu, Y. Novel hematite nanorods and magnetite nanoparticles prepared from MIL-100(Fe) template for the removal of As(V). *Mater. Lett.* **2014**, *132*, 8–10. [CrossRef]
86. Shen, L.; Huang, L.; Liang, S.; Liang, R.; Qin, N.; Wu, L. Electrostatically derived self-assembly of NH₂-mediated zirconium MOFs with graphene for photocatalytic reduction of Cr(VI). *RSC Adv.* **2014**, *4*, 2546–2549. [CrossRef]
87. Wang, C.-C.; Du, X.-D.; Li, J.; Guo, X.-X.; Wang, P.; Zhang, J. Photocatalytic Cr(VI) reduction in metal-organic frameworks: A mini-review. *Appl. Catal. B* **2016**, *193*, 198–216. [CrossRef]
88. Yang, Q.; Zhao, Q.; Ren, S.; Chen, Z.; Zheng, H. Assembly of Zr-MOF crystals onto magnetic beads as a highly adsorbent for recycling nitrophenol. *Chem. Eng. J.* **2017**, *323*, 74–83. [CrossRef]
89. Niu, H.; Zheng, Y.; Wang, S.; Zhao, L.; Yang, S.; Cai, Y. Continuous generation of hydroxyl radicals for highly efficient elimination of chlorophenols and phenols catalyzed by heterogeneous Fenton-like catalysts yolk/shell Pd@Fe₃O₄@metal organic frameworks. *J. Hazard. Mater.* **2018**, *346*, 174–183. [CrossRef]
90. Teng, W.; Bai, N.; Chen, Z.; Shi, J.; Fan, J.; Zhang, W.X. Hierarchically porous carbon derived from metal-organic frameworks for separation of aromatic pollutants. *Chem. Eng. J.* **2018**, *346*, 388–396. [CrossRef]
91. He, D.; Niu, H.; He, S.; Mao, L.; Cai, Y.; Liang, Y. Strengthened Fenton degradation of phenol catalyzed by core/shell Fe-Pd@C nanocomposites derived from mechanochemically synthesized Fe-Metal organic frameworks. *Water Res.* **2019**, *162*, 151–160. [CrossRef]
92. Ahsan, M.A.; Fernandez-Delgado, O.; Deemer, E.; Wang, H.; El-Gendy, A.A.; Curry, M.L.; Noveron, J.C. Carbonization of Co-BDC MOF results in magnetic C@Co nanoparticles that catalyze the reduction of methyl orange and 4-nitrophenol in water. *J. Mol. Liq.* **2019**, *290*, 111059. [CrossRef]
93. Wang, S.; Boyjoo, Y.; Choueib, A.; Zhu, Z.H. Removal of dyes from aqueous solution using fly ash and red mud. *Water Res.* **2005**, *39*, 129–138. [CrossRef]
94. Liang, J.; Ning, X.A.; Sun, J.; Song, J.; Lu, J.; Cai, H.; Hong, Y. Toxicity evaluation of textile dyeing effluent and its possible relationship with chemical oxygen demand. *Ecotoxicol. Environ. Saf.* **2018**, *166*, 56–62. [CrossRef] [PubMed]
95. Nidheesh, P.V.; Zhou, M.; Oturan, M.A. An overview on the removal of synthetic dyes from water by electrochemical advanced oxidation processes. *Chemosphere* **2018**, *197*, 210–227. [CrossRef] [PubMed]
96. Chang, C.; Wang, X.; Bai, Y.; Liu, H. Applications of nanomaterials in enantioseparation and related techniques. *Trends Anal. Chem.* **2012**, *39*, 195–206. [CrossRef]
97. Liu, H.; Chen, L.; Ding, J. Adsorption behavior of magnetic amino-functionalized metal-organic framework for cationic and anionic dyes from aqueous solution. *RSC Adv.* **2016**, *6*, 48884–48895. [CrossRef]
98. Yang, Q.; Ren, S.; Zhao, Q.; Lu, R.; Hang, C.; Chen, Z.; Zheng, H. Selective separation of methyl orange from water using magnetic ZIF-67 composites. *Chem. Eng. J.* **2018**, *333*, 49–57. [CrossRef]
99. Shi, Z.; Xu, C.; Guan, H.; Li, L.; Fan, L.; Wang, Y.; Liu, L.; Meng, Q.; Zhang, R. Magnetic metal organic frameworks (MOFs) composite for removal of lead and malachite green in wastewater. *Colloids Surf. A* **2018**, *539*, 382–390. [CrossRef]
100. Xu, S.; Lv, Y.; Zeng, X.; Cao, D. ZIF-derived nitrogen-doped porous carbons as highly efficient adsorbents for removal of organic compounds from wastewater. *Chem. Eng. J.* **2017**, *323*, 502–511. [CrossRef]
101. Zhao, S.; Chen, D.; Wei, F.; Chen, N.; Liang, Z.; Luo, Y. Synthesis of graphene oxide/metal-organic frameworks hybrid materials for enhanced removal of Methylene blue in acidic and alkaline solutions. *J. Chem. Technol. Biotechnol.* **2017**, *93*, 698–709. [CrossRef]
102. Zhao, S.; Chen, D.; Wei, F.; Chen, N.; Liang, Z.; Luo, Y. Removal of Congo red dye from aqueous solution with nickel-based metal-organic framework/graphene oxide composites prepared by ultrasonic wave-assisted ball milling. *Ultrason. Sonochem.* **2017**, *39*, 845–852. [CrossRef] [PubMed]
103. Liu, X.; Luo, J.; Chen, X.; Yang, Y.; Yang, S. Selective adsorption performance of H₆P₂Mo₁₅W₃O₆₂-based Cu₃(BTC)₂ composite in treatment of simulated cationic dye wastewater. *Chem. Res. Chin. Univ.* **2017**, *33*, 268–273. [CrossRef]
104. Shao, Y.; Zhou, L.; Bao, C.; Ma, J.; Liu, M.; Wang, F. Magnetic responsive metal-organic frameworks nanosphere with core-shell structure for highly efficient removal of methylene blue. *Chem. Eng. J.* **2016**, *283*, 1127–1136. [CrossRef]
105. Zhang, C.F.; Qiu, L.G.; Ke, F.; Zhu, Y.J.; Yuan, Y.P.; Xu, G.S.; Jiang, X. A novel magnetic recyclable photocatalyst based on a core-shell metal-organic framework Fe₃O₄@MIL-100(Fe) for the decolorization of methylene blue dye. *J. Mater. Chem. A* **2013**, *1*, 14329. [CrossRef]

106. Yue, X.; Guo, W.; Li, X.; Zhou, H.; Wang, R. Core-shell Fe₃O₄@MIL-101(Fe) composites as heterogeneous catalysts of persulfate activation for the removal of Acid Orange 7. *Environ. Sci. Pollut. Res.* **2016**, *23*, 15218–15226. [[CrossRef](#)]
107. Zhang, Y.; Zhou, J.; Feng, Q.; Chen, X.; Hu, Z. Visible light photocatalytic degradation of MB using UiO-66/g-C₃N₄ heterojunction nanocatalyst. *Chemosphere* **2018**, *212*, 523–532. [[CrossRef](#)]
108. Wang, C.; Wang, H.; Luo, R.; Liu, C.; Li, J.; Sun, X.; Shen, J.; Han, W.; Wang, L. Metal-organic framework one-dimensional fibers as efficient catalysts for activating peroxydisulfate. *Chem. Eng. J.* **2017**, *330*, 262–271. [[CrossRef](#)]
109. Wu, C.H.; Yun, W.C.; Wi-Afedzi, T.; Lin, K.A. ZIF-67 supported on macroscale resin as an efficient and convenient heterogeneous catalyst for Oxone activation. *J. Colloid Interf. Sci.* **2018**, *514*, 262–271. [[CrossRef](#)]
110. Ren, W.; Gao, J.; Lei, C.; Xie, Y.; Cai, Y.; Ni, Q.; Yao, J. Recyclable metal-organic framework/cellulose aerogels for activating peroxydisulfate to degrade organic pollutants. *Chem. Eng. J.* **2018**, *349*, 766–774. [[CrossRef](#)]
111. Jin, L.; Zhao, X.; Qian, X.; Dong, M. Nickel nanoparticles encapsulated in porous carbon and carbon nanotube hybrids from bimetallic metal-organic-frameworks for highly efficient adsorption of dyes. *J. Colloid Interf. Sci.* **2018**, *509*, 245–253. [[CrossRef](#)]
112. Lin, H.Y.; Zhao, J.; Song, G.; Luan, J.; Liu, X.X.; Liu, G.C. High quality and high performance adsorption of Congo red using as-grown MWCNTs synthesized over a Co-MOF as a catalyst precursor via the CVD method. *Dalton Trans.* **2017**, *46*, 17067–17073. [[CrossRef](#)] [[PubMed](#)]
113. Wang, G.; Chen, S.; Quan, X.; Yu, H.; Zhang, Y. Enhanced activation of peroxydisulfate by nitrogen doped porous carbon for effective removal of organic pollutants. *Carbon* **2017**, *115*, 730–739. [[CrossRef](#)]
114. Ma, W.; Du, Y.; Wang, N.; Miao, P. ZIF-8 derived nitrogen-doped porous carbon as metal-free catalyst of peroxydisulfate activation. *Environ. Sci. Pollut. Res. Int.* **2017**, *24*, 16276–16288. [[CrossRef](#)] [[PubMed](#)]
115. Wang, N.; Ma, W.; Ren, Z.; Du, Y.; Xu, P.; Han, X. Prussian blue analogues derived porous nitrogen-doped carbon microspheres as high-performance metal-free peroxydisulfate activators for non-radical-dominated degradation of organic pollutants. *J. Mater. Chem. A* **2018**, *6*, 884–895. [[CrossRef](#)]
116. Lin, K.A.; Chen, B.J. Prussian blue analogue derived magnetic carbon/cobalt/iron nanocomposite as an efficient and recyclable catalyst for activation of peroxydisulfate. *Chemosphere* **2017**, *166*, 146–156. [[CrossRef](#)]
117. Zhang, Y.F.; Qiu, L.G.; Yuan, Y.P.; Zhu, Y.J.; Jiang, X.; Xiao, J.D. Magnetic Fe₃O₄@C/Cu and Fe₃O₄@CuO core-shell composites constructed from MOF-based materials and their photocatalytic properties under visible light. *Appl. Catal. B* **2014**, *144*, 863–869. [[CrossRef](#)]
118. Andrew Lin, K.Y.; Hsu, F.K.; Lee, W.D. Magnetic cobalt-graphene nanocomposite derived from self-assembly of MOFs with graphene oxide as an activator for peroxydisulfate. *J. Mater. Chem. A* **2015**, *3*, 9480–9490. [[CrossRef](#)]
119. Ai, L.; Zhang, C.; Li, L.; Jiang, J. Iron terephthalate metal-organic framework: Revealing the effective activation of hydrogen peroxide for the degradation of organic dye under visible light irradiation. *Appl. Catal. B* **2014**, *148–149*, 191–200. [[CrossRef](#)]
120. Chen, X.; Zheng, Z.; Ke, X.; Jaatinen, E.; Xie, T.; Wang, D.; Guo, C.; Zhao, J.; Zhu, H. Supported silver nanoparticles as photocatalysts under ultraviolet and visible light irradiation. *Green Chem.* **2010**, *12*, 414. [[CrossRef](#)]
121. Li, M.; Meng, J.; Li, Q.; Huang, M.; Liu, X.; Owusu, K.A.; Liu, Z.; Mai, L. Finely Crafted 3D Electrodes for Dendrite-Free and High-Performance Flexible Fiber-Shaped Zn-Co Batteries. *Adv. Funct. Mater.* **2018**, *28*, 1802016. [[CrossRef](#)]
122. Duan, X.; Ao, Z.; Sun, H.; Indrawirawan, S.; Wang, Y.; Kang, J.; Liang, F.; Zhu, Z.H.; Wang, S. Nitrogen-doped graphene for generation and evolution of reactive radicals by metal-free catalysis. *ACS Appl. Mater. Interfaces* **2015**, *7*, 4169–4178. [[CrossRef](#)] [[PubMed](#)]
123. Wei, Z.; Chen, D.; Guo, Z.; Jia, P.; Xing, H. Eosin Y-Embedded Zirconium-Based Metal-Organic Framework as a Dual-Emitting Built-In Self-Calibrating Platform for Pesticide Detection. *Inorg. Chem.* **2020**, *59*, 5386–5393. [[CrossRef](#)]
124. Li, Z. Spatiotemporal pattern models for bioaccumulation of pesticides in common herbaceous and woody plants. *J. Environ. Manag.* **2020**, *276*, 111334. [[CrossRef](#)] [[PubMed](#)]
125. Pan, D.; He, M.; Kong, F. Risk attitude, risk perception, and farmers' pesticide application behavior in China: A moderation and mediation model. *J. Clean. Prod.* **2020**, *276*, 124241. [[CrossRef](#)]
126. Kim, K.H.; Kabir, E.; Jahan, S.A. Exposure to pesticides and the associated human health effects. *Sci. Total Environ.* **2017**, *575*, 525–535. [[CrossRef](#)]
127. Yadav, I.C.; Devi, N.L.; Syed, J.H.; Cheng, Z.; Li, J.; Zhang, G.; Jones, K.C. Current status of persistent organic pesticides residues in air, water, and soil, and their possible effect on neighboring countries: A comprehensive review of India. *Sci. Total Environ.* **2015**, *511*, 123–137. [[CrossRef](#)]
128. Abdelhameed, R.M.; Abdel-Gawad, H.; Elshahat, M.; Emam, H.E. Cu-BTC@cotton composite: Design and removal of ethion insecticide from water. *RSC Adv.* **2016**, *6*, 42324–42333. [[CrossRef](#)]
129. Wang, X.; Ma, X.; Huang, P.; Wang, J.; Du, T.; Du, X.; Lu, X. Magnetic Cu-MOFs embedded within graphene oxide nanocomposites for enhanced preconcentration of benzenoid-containing insecticides. *Talanta* **2018**, *181*, 112–117. [[CrossRef](#)]
130. Liu, G.; Li, L.; Xu, D.; Huang, X.; Xu, X.; Zheng, S.; Zhang, Y.; Lin, H. Metal-organic framework preparation using magnetic graphene oxide-beta-cyclodextrin for neonicotinoid pesticide adsorption and removal. *Carbohydr. Polym.* **2017**, *175*, 584–591. [[CrossRef](#)]
131. Liang, R.; Jing, F.; Shen, L.; Qin, N.; Wu, L. MIL-53(Fe) as a highly efficient bifunctional photocatalyst for the simultaneous reduction of Cr(VI) and oxidation of dyes. *J. Hazard. Mater.* **2015**, *287*, 364–372. [[CrossRef](#)]

132. Oladipo, A.A.; Vaziri, R.; Abureesh, M.A. Highly robust AgIO₃ /MIL-53 (Fe) nanohybrid composites for degradation of organophosphorus pesticides in single and binary systems: Application of artificial neural networks modelling. *J. Taiwan Inst. Chem. Eng.* **2018**, *83*, 133–142. [[CrossRef](#)]
133. Naimi Joubani, M.; Zanjanchi, M.A.; Sohrabnezhad, S. The carboxylate magnetic—Zinc based metal-organic framework hetero-junction: Fe₃O₄-COOH@ZIF-8/Ag/Ag₃PO₄ for plasmon enhanced visible light Z-scheme photocatalysis. *Adv. Powder Technol.* **2020**, *31*, 29–39. [[CrossRef](#)]
134. Shen, K.; Chen, L.; Long, J.; Zhong, W.; Li, Y. MOFs-Templated Co@Pd Core-Shell NPs Embedded in N-Doped Carbon Matrix with Superior Hydrogenation Activities. *ACS Catal.* **2015**, *5*, 5264–5271. [[CrossRef](#)]
135. Long, J.; Shen, K.; Chen, L.; Li, Y. Multimetal-MOF-derived transition metal alloy NPs embedded in an N-doped carbon matrix: Highly active catalysts for hydrogenation reactions. *J. Mater. Chem. A* **2016**, *4*, 10254–10262. [[CrossRef](#)]
136. Ye, G.; Luo, P.; Zhao, Y.; Qiu, G.; Hu, Y.; Preis, S.; Wei, C. Three-dimensional Co/Ni bimetallic organic frameworks for high-efficient catalytic ozonation of atrazine: Mechanism, effect parameters, and degradation pathways analysis. *Chemosphere* **2020**, *253*, 126767. [[CrossRef](#)] [[PubMed](#)]
137. Cuerda-Correa, E.M.; Dominguez-Vargas, J.R.; Olivares-Marin, F.J.; de Heredia, J.B. On the use of carbon blacks as potential low-cost adsorbents for the removal of non-steroidal anti-inflammatory drugs from river water. *J. Hazard. Mater.* **2010**, *177*, 1046–1053. [[CrossRef](#)]
138. Hasan, Z.; Jeon, J.; Jhung, S.H. Adsorptive removal of naproxen and clofibric acid from water using metal-organic frameworks. *J. Hazard. Mater.* **2012**, *209–210*, 151–157. [[CrossRef](#)] [[PubMed](#)]
139. Rivera-Jiménez, S.M.; Hernández-Maldonado, A.J. Nickel(II) grafted MCM-41: A novel sorbent for the removal of Naproxen from water. *Micropor. Mesopor. Mater.* **2008**, *116*, 246–252. [[CrossRef](#)]
140. Park, S.; Lee, W. Removal of selected pharmaceuticals and personal care products in reclaimed water during simulated managed aquifer recharge. *Sci. Total Environ.* **2018**, *640–641*, 671–677. [[CrossRef](#)]
141. Jamil, K. Health effects of pharmaceuticals and personal care products. In *Pharmaceuticals and Personal Care Products: Waste Management and Treatment Technology*, 1st ed.; Prasad, M.N.V., Vithanage, M., Kapley, A., Eds.; Butterworth-Heinemann: Kidlington, UK, 2019; pp. 115–128.
142. Mendez-Arriaga, F.; Esplugas, S.; Gimenez, J. Photocatalytic degradation of non-steroidal anti-inflammatory drugs with TiO₂ and simulated solar irradiation. *Water Res.* **2008**, *42*, 585–594. [[CrossRef](#)]
143. Marti, E.; Variatza, E.; Balcazar, J.L. The role of aquatic ecosystems as reservoirs of antibiotic resistance. *Trends Microbiol.* **2014**, *22*, 36–41. [[CrossRef](#)] [[PubMed](#)]
144. Moradi, S.E.; Haji Shabani, A.M.; Dadfarnia, S.; Emami, S. Effective removal of ciprofloxacin from aqueous solutions using magnetic metal-organic framework sorbents: Mechanisms, isotherms and kinetics. *J. Iran. Chem. Soc.* **2016**, *13*, 1617–1627. [[CrossRef](#)]
145. Bayazit, S.S.; Danalioglu, S.T.; Abdel Salam, M.; Kerkez Kuyumcu, O. Preparation of magnetic MIL-101 (Cr) for efficient removal of ciprofloxacin. *Environ. Sci. Pollut. Res. Int.* **2017**, *24*, 25452–25461. [[CrossRef](#)] [[PubMed](#)]
146. Xiong, W.; Zeng, G.; Yang, Z.; Zhou, Y.; Zhang, C.; Cheng, M.; Liu, Y.; Hu, L.; Wan, J.; Zhou, C.; et al. Adsorption of tetracycline antibiotics from aqueous solutions on nanocomposite multi-walled carbon nanotube functionalized MIL-53(Fe) as new adsorbent. *Sci. Total Environ.* **2018**, *627*, 235–244. [[CrossRef](#)]
147. Sun, Y.; Chen, M.; Liu, H.; Zhu, Y.; Wang, D.; Yan, M. Adsorptive removal of dye and antibiotic from water with functionalized zirconium-based metal organic framework and graphene oxide composite nanomaterial UiO-66-(OH)₂/GO. *Appl. Surf. Sci.* **2020**, *525*, 146614. [[CrossRef](#)]
148. Sun, X.; Hu, D.; Yang, L.Y.; Wang, N.; Wang, Y.G.; Ouyang, X.K. Efficient adsorption of Levofloxacin from aqueous solution using calcium alginate/metal organic frameworks composite beads. *J. Sol-Gel Sci. Technol.* **2019**, *91*, 353–363. [[CrossRef](#)]
149. Luo, Z.; Chen, H.; Wu, S.; Yang, C.; Cheng, J. Enhanced removal of bisphenol A from aqueous solution by aluminum-based MOF/sodium alginate-chitosan composite beads. *Chemosphere* **2019**, *237*, 124493. [[CrossRef](#)]
150. Mohamed, A.K.; Mahmoud, M.E. Encapsulation of starch hydrogel and doping nanomagnetite onto metal-organic frameworks for efficient removal of fluvastatin antibiotic from water. *Carbohydr. Polym.* **2020**, *245*, 116438. [[CrossRef](#)]
151. Yang, W.; Han, Y.; Li, C.; Zhu, L.; Shi, L.; Tang, W.; Wang, J.; Yue, T.; Li, Z. Shapeable three-dimensional CMC aerogels decorated with Ni/Co-MOF for rapid and highly efficient tetracycline hydrochloride removal. *Chem. Eng. J.* **2019**, *375*, 122076. [[CrossRef](#)]
152. Zhao, X.; Zhao, H.; Dai, W.; Wei, Y.; Wang, Y.; Zhang, Y.; Zhi, L.; Huang, H.; Gao, Z. A metal-organic framework with large 1-D channels and rich OH sites for high-efficiency chloramphenicol removal from water. *J. Colloid Interf. Sci.* **2018**, *526*, 28–34. [[CrossRef](#)]
153. Gao, Y.; Xia, J.; Liu, D.; Kang, R.; Yu, G.; Deng, S. Synthesis of mixed-linker Zr-MOFs for emerging contaminant adsorption and photodegradation under visible light. *Chem. Eng. J.* **2019**, *378*, 122118. [[CrossRef](#)]
154. Bhadra, B.N.; Jhung, S.H. Adsorptive removal of wide range of pharmaceuticals and personal care products from water using bio-MOF-1 derived porous carbon. *Micropor. Mesopor. Mater.* **2018**, *270*, 102–108. [[CrossRef](#)]
155. Sarker, M.; An, H.J.; Yoo, D.K.; Jhung, S.H. Nitrogen-doped porous carbon from ionic liquid@Al-metal-organic framework: A prominent adsorbent for purification of both aqueous and non-aqueous solutions. *Chem. Eng. J.* **2018**, *338*, 107–116. [[CrossRef](#)]
156. Liang, C.; Zhang, X.; Feng, P.; Chai, H.; Huang, Y. ZIF-67 derived hollow cobalt sulfide as superior adsorbent for effective adsorption removal of ciprofloxacin antibiotics. *Chem. Eng. J.* **2018**, *344*, 95–104. [[CrossRef](#)]

157. Peng, H.; Cao, J.; Xiong, W.; Yang, Z.; Jia, M.; Sun, S.; Xu, Z.; Zhang, Y.; Cai, H. Two-dimension N-doped nanoporous carbon from KCl thermal exfoliation of Zn-ZIF-L: Efficient adsorption for tetracycline and optimizing of response surface model. *J. Hazard. Mater.* **2020**, *402*, 123498. [[CrossRef](#)] [[PubMed](#)]
158. Ahmed, I.; Bhadra, B.N.; Lee, H.J.; Jhung, S.H. Metal-organic framework-derived carbons: Preparation from ZIF-8 and application in the adsorptive removal of sulfamethoxazole from water. *Catal. Today* **2018**, *301*, 90–97. [[CrossRef](#)]
159. Li, S.; Zhang, X.; Huang, Y. Zeolitic imidazolate framework-8 derived nanoporous carbon as an effective and recyclable adsorbent for removal of ciprofloxacin antibiotics from water. *J. Hazard. Mater.* **2017**, *321*, 711–719. [[CrossRef](#)]
160. Chen, H.; Gao, B.; Li, H. Removal of sulfamethoxazole and ciprofloxacin from aqueous solutions by graphene oxide. *J. Hazard. Mater.* **2015**, *282*, 201–207. [[CrossRef](#)]
161. Shi, S.; Fan, Y.; Huang, Y. Facile Low Temperature Hydrothermal Synthesis of Magnetic Mesoporous Carbon Nanocomposite for Adsorption Removal of Ciprofloxacin Antibiotics. *Ind. Eng. Chem. Res.* **2013**, *52*, 2604–2612. [[CrossRef](#)]
162. Yu, F.; Sun, S.; Han, S.; Zheng, J.; Ma, J. Adsorption removal of ciprofloxacin by multi-walled carbon nanotubes with different oxygen contents from aqueous solutions. *Chem. Eng. J.* **2016**, *285*, 588–595. [[CrossRef](#)]
163. Carabineiro, S.A.; Thavorn-Amornsri, T.; Pereira, M.F.; Figueiredo, J.L. Adsorption of ciprofloxacin on surface-modified carbon materials. *Water Res.* **2011**, *45*, 4583–4591. [[CrossRef](#)]
164. Ke, Q.; Shi, Y.; Liu, Y.; Chen, F.; Wang, H.; Wu, X.L.; Lin, H.; Chen, J. Enhanced catalytic degradation of bisphenol A by hemin-MOFs supported on boron nitride via the photo-assisted heterogeneous activation of persulfate. *Sep. Purif. Technol.* **2019**, *229*, 115822. [[CrossRef](#)]
165. Sun, Z.; Wu, X.; Qu, K.; Huang, Z.; Liu, S.; Dong, M.; Guo, Z. Bimetallic metal-organic frameworks anchored corn-cob-derived porous carbon photocatalysts for synergistic degradation of organic pollutants. *Chemosphere* **2020**, *259*, 127389. [[CrossRef](#)] [[PubMed](#)]
166. Liang, R.; Luo, S.; Jing, F.; Shen, L.; Qin, N.; Wu, L. A simple strategy for fabrication of Pd@MIL-100(Fe) nanocomposite as a visible-light-driven photocatalyst for the treatment of pharmaceuticals and personal care products (PPCPs). *Appl. Catal. B* **2015**, *176–177*, 240–248. [[CrossRef](#)]
167. He, L.; Dong, Y.; Zheng, Y.; Jia, Q.; Shan, S.; Zhang, Y. A novel magnetic MIL-101(Fe)/TiO₂ composite for photo degradation of tetracycline under solar light. *J. Hazard. Mater.* **2019**, *361*, 85–94. [[CrossRef](#)]
168. Liu, F.; Cao, J.; Yang, Z.; Xiong, W.; Xu, Z.; Song, P.; Jia, M.; Sun, S.; Zhang, Y.; Zhong, X. Heterogeneous activation of peroxymonosulfate by cobalt-doped MIL-53(Al) for efficient tetracycline degradation in water: Coexistence of radical and non-radical reactions. *J. Colloid Interf. Sci.* **2020**, *581*, 195–204. [[CrossRef](#)] [[PubMed](#)]
169. Pi, Y.; Ma, L.; Zhao, P.; Cao, Y.; Gao, H.; Wang, C.; Li, Q.; Dong, S.; Sun, J. Facile green synthetic graphene-based Co-Fe Prussian blue analogues as an activator of peroxymonosulfate for the degradation of levofloxacin hydrochloride. *J. Colloid Interf. Sci.* **2018**, *526*, 18–27. [[CrossRef](#)]
170. Zhang, M.; Wang, C.; Liu, C.; Luo, R.; Li, J.; Sun, X.; Shen, J.; Han, W.; Wang, L. Metal-organic framework derived Co₃O₄/C@SiO₂ yolk-shell nanoreactors with enhanced catalytic performance. *J. Mater. Chem. A* **2018**, *6*, 11226–11235. [[CrossRef](#)]
171. Gong, Y.; Zhao, X.; Zhang, H.; Yang, B.; Xiao, K.; Guo, T.; Zhang, J.; Shao, H.; Wang, Y.; Yu, G. MOF-derived nitrogen doped carbon modified g-C₃N₄ heterostructure composite with enhanced photocatalytic activity for bisphenol A degradation with peroxymonosulfate under visible light irradiation. *Appl. Catal. B* **2018**, *233*, 35–45. [[CrossRef](#)]
172. Cao, J.; Yang, Z.; Xiong, W.; Zhou, Y.; Wu, Y.; Jia, M.; Sun, S.; Zhou, C.; Zhang, Y.; Zhong, R. Peroxymonosulfate activation of magnetic Co nanoparticles relative to an N-doped porous carbon under confinement: Boosting stability and performance. *Sep. Purif. Technol.* **2020**, *250*, 117237. [[CrossRef](#)]
173. Wu, S.; Liu, H.; Yang, C.; Li, X.; Lin, Y.; Yin, K.; Sun, J.; Teng, Q.; Du, C.; Zhong, Y. High-performance porous carbon catalysts doped by iron and nitrogen for degradation of bisphenol F via peroxymonosulfate activation. *Chem. Eng. J.* **2020**, *392*, 123683. [[CrossRef](#)]
174. Tang, J.; Wang, J. MOF-derived three-dimensional flower-like FeCu@C composite as an efficient Fenton-like catalyst for sulfamethazine degradation. *Chem. Eng. J.* **2019**, *375*, 122007. [[CrossRef](#)]
175. Yang, Q.; Chen, D.; Chu, L.; Wang, J. Enhancement of ionizing radiation-induced catalytic degradation of antibiotics using Fe/C nanomaterials derived from Fe-based MOFs. *J. Hazard. Mater.* **2020**, *389*, 122148. [[CrossRef](#)]
176. Yang, S.; Qiu, X.; Jin, P.; Dzakpasu, M.; Wang, X.C.; Zhang, Q.; Zhang, L.; Yang, L.; Ding, D.; Wang, W.; et al. MOF-templated synthesis of CoFe₂O₄ nanocrystals and its coupling with peroxymonosulfate for degradation of bisphenol A. *Chem. Eng. J.* **2018**, *353*, 329–339. [[CrossRef](#)]
177. Song, W.; Ge, P.; Ke, Q.; Sun, Y.; Chen, F.; Wang, H.; Shi, Y.; Wu, X.L.; Lin, H.; Chen, J.; et al. Insight into the mechanisms for hexavalent chromium reduction and sulfisoxazole degradation catalyzed by graphitic carbon nitride: The Yin and Yang in the photo-assisted processes. *Chemosphere* **2019**, *221*, 166–174. [[CrossRef](#)] [[PubMed](#)]
178. Jia, Z.; Kang, J.; Zhang, W.C.; Wang, W.M.; Yang, C.; Sun, H.; Habibi, D.; Zhang, L.C. Surface aging behaviour of Fe-based amorphous alloys as catalysts during heterogeneous photo Fenton-like process for water treatment. *Appl. Catal. B* **2017**, *204*, 537–547. [[CrossRef](#)]
179. Lei, Y.; Wei, L.; Zhai, S.; Wang, Y.; Karahan, H.E.; Chen, X.; Zhou, Z.; Wang, C.; Sui, X.; Chen, Y. Metal-free bifunctional carbon electrocatalysts derived from zeolitic imidazolate frameworks for efficient water splitting. *Mater. Chem. Front.* **2018**, *2*, 102–111. [[CrossRef](#)]

180. Kaneti, Y.V.; Zhang, J.; He, Y.B.; Wang, Z.; Tanaka, S.; Hossain, M.S.A.; Pan, Z.Z.; Xiang, B.; Yang, Q.H.; Yamauchi, Y. Fabrication of an MOF-derived heteroatom-doped Co/CoO/carbon hybrid with superior sodium storage performance for sodium-ion batteries. *J. Mater. Chem. A* **2017**, *5*, 15356–15366. [[CrossRef](#)]
181. Sarker, M.; Shin, S.; Jeong, J.H.; Jhung, S.H. Mesoporous metal-organic framework PCN-222(Fe): Promising adsorbent for removal of big anionic and cationic dyes from water. *Chem. Eng. J.* **2019**, *371*, 252–259. [[CrossRef](#)]
182. Ahmed, I.; Jhung, S.H. Applications of metal-organic frameworks in adsorption/separation processes via hydrogen bonding interactions. *Chem. Eng. J.* **2017**, *310*, 197–215. [[CrossRef](#)]
183. Tang, J.; Wang, J. Fenton-like degradation of sulfamethoxazole using Fe-based magnetic nanoparticles embedded into mesoporous carbon hybrid as an efficient catalyst. *Chem. Eng. J.* **2018**, *351*, 1085–1094. [[CrossRef](#)]
184. Hu, B.; Yuan, J.Y.; Tian, J.Y.; Wang, M.; Wang, X.; He, L.; Zhang, Z.; Wang, Z.W.; Liu, C.S. Co/Fe-bimetallic organic framework-derived carbon-incorporated cobalt-ferric mixed metal phosphide as a highly efficient photocatalyst under visible light. *J. Colloid Interf. Sci.* **2018**, *531*, 148–159. [[CrossRef](#)] [[PubMed](#)]
185. Yang, C.L.; Wen, J.; Xue, Z.Z.; Yin, X.Y.; Li, Y.F.; Yuan, L. The accumulation and toxicity of ZIF-8 nanoparticles in *Corbicula fluminea*. *J. Environ. Sci.* **2023**, *127*, 91–101. [[CrossRef](#)] [[PubMed](#)]
186. Ruyra, A.; Yazdi, A.; Espin, J.A.; Carne-Sanchez, N.; Roher, J.; Lorenzo, I.; Imaz, D. Maspoch, Synthesis, culture medium stability, and in vitro and in vivo zebrafish embryo toxicity of metal-organic framework nanoparticles. *Chemistry* **2015**, *21*, 2508–2518. [[CrossRef](#)] [[PubMed](#)]
187. Fan, G.; Hong, L.; Zheng, X.; Zhou, J.; Zhan, J.; Chen, Z.; Liu, S. Growth inhibition of *Microcystic aeruginosa* by metal-organic frameworks: Effect of variety, metal ion and organic ligand. *RSC Adv.* **2018**, *8*, 35314–35326. [[CrossRef](#)]

Disclaimer/Publisher's Note: The statements, opinions and data contained in all publications are solely those of the individual author(s) and contributor(s) and not of MDPI and/or the editor(s). MDPI and/or the editor(s) disclaim responsibility for any injury to people or property resulting from any ideas, methods, instructions or products referred to in the content.